FACULTY OF SCIENCE
UNIVERSITY OF COPENHAGEN

Master thesis

Mikkel Theiss Kristensen

Rare Emission-line Galaxies in the COSMOS Field

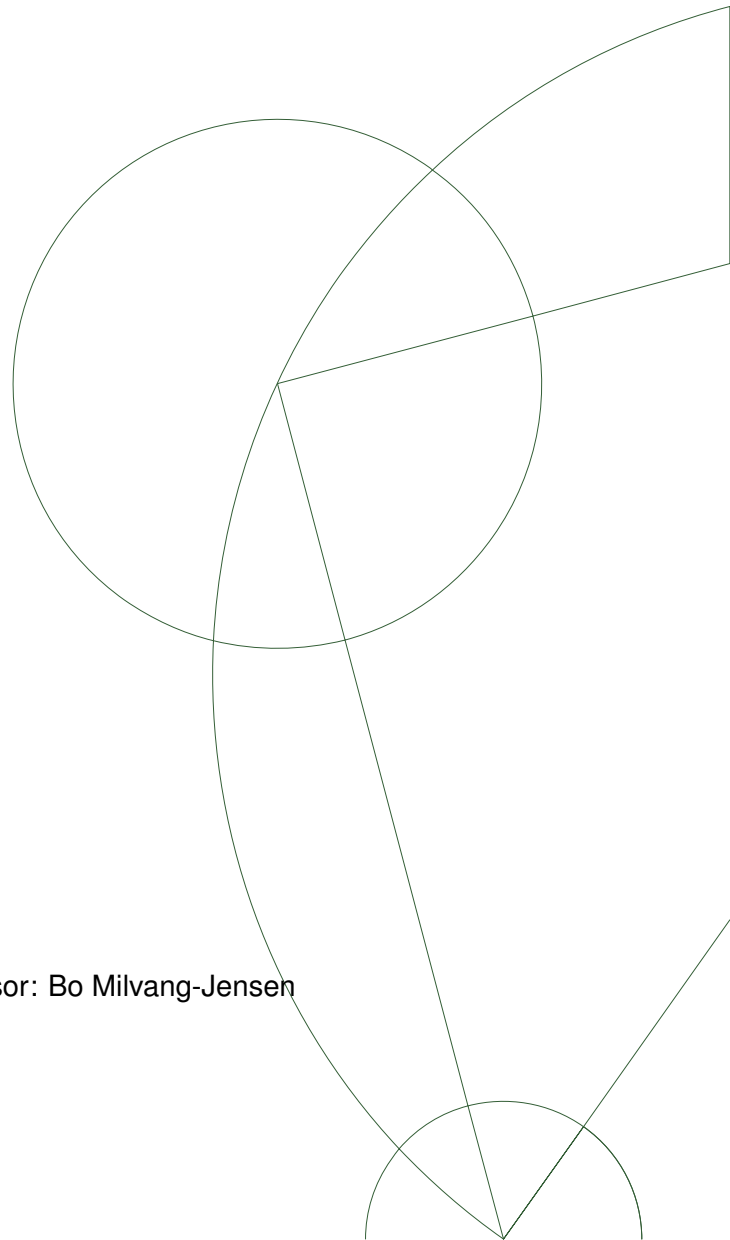

Main supervisor: Johan Peter Uldall Fynbo, co-supervisor: Bo Milvang-Jensen

Submitted December 23, 2015

Abstract

Large scale surveys such as COSMOS are invaluable for observing galaxies across cosmic time. Coupled with narrow band filters, surveys can be used to search for galaxies with emission lines at specific redshifts. The 4-meter VISTA telescope contributes to the COSMOS with an ultra-deep survey (UltraVISTA) with narrow-band imaging utilizing the NB118 filter centered at 11910 Å. This filter enables the search for a number of strong emission lines at $z \leq 2.2$. For $z > 2.2$, a number of rarer emission lines can be found such as MgII at $z = 3.3$, CII] at $z = 4.1$, and CIII] at $z = 5.2$. Such emitters are rare. Combining the newest Y, NB118, and J images from UltraVISTA with the COSMOS2015 catalog containing precise photometric redshifts for more than half a million objects, the hope is to find a range of rare line emitters at high redshifts ($z > 2.5$). Candidates are selected if they shave narrow band excess. The method employed is evaluated in order to optimize the parameters for the present search. It is found that stricter detection parameters strongly influence the number of high redshift objects whereas selection parameters mostly affect the number of selected candidates rather than their redshifts. The 105 selected candidates, also called outliers, are found to have $\langle z \rangle = 3.08 \pm 0.62$, although a large number have undesirable traits leaving only 34 for further for analysis with $\langle z \rangle = 3.35 \pm 0.56$. Out of the 34 good outliers, 13 ($\sim 38\%$) are likely MgII emitters. Up to 8 ($\sim 24\%$) more that may be MgII emitters also but their nature is uncertain. 2 ($\sim 6\%$) may be CII] emitters and 1 ($\sim 3\%$) outlier is consistent with CIII] ($\sim 3\%$). The remaining 10 ($\sim 29\%$) are possibly [OII] emitters, although their narrow band excesses may be emission lines not considered.

Contents

1 | Introduction

The purpose of this thesis is to search for and examine objects in the COSMOS field that show evidence for rare emission lines. The objects are selected from two main criteria: excess in a narrow band filter and constraints on the redshift that excludes known, common emission line galaxies from star-forming galaxies and/or active galactic nuclei (AGN). Combined with photometric measurements from other telescopes, an attempt to classify the objects is made.

A narrow-band excess is indicative of an increased brightness in a small part of an object's spectrum compared to a background or continuum level. Selecting on this criteria alone will yield a large number of selected objects - most of which will be star-forming galaxies with very common oxygen or hydrogen emission lines. By requiring a high redshift on objects, the expectation is to weed many of them out.

Additionally, the method employed will be reviewed as it might have implications for similar type of studies.

First, source extraction will be carried out in images from UltraVISTA, which is a deep and ultra-deep survey of the COSMOS field performed by the Visible and Infrared Survey Telescope for Astronomy (VISTA). Specifically, images from a narrow band (NB118) will be used for detection and two neighboring broad bands (Y and J) will be used to establish a continuum from which the narrow band may show excess. The parameter space for source extraction and candidate selection are also explored in order to determine the robustness of the method.

Identification from UltraVISTA data alone is difficult as it only covers the near-infrared. A dataset that covers ultraviolet, optical, and mid-infrared wavelengths is included in aiding classification and construction of spectral energy distributions (SED). The catalog is obtained from Laigle et al. (submitted), which also contains the photometric redshifts used in the selection processes.

Several other properties derived from SED fitting such as star formation rates (SFR), stellar masses, redshift probability distributions (PDZ), and much more are included in the catalog.

Once the parameters have been established, data has been matched and objects with narrow band excess found, detailed analysis and sorting are carried out. This includes: examining the photometric redshifts to see if the position of the narrow band matches any strong emission lines, comparing SFR with stellar mass to check for extremely star forming/passive galaxies, and study the morphology in a Hubble Space Telescope (HST) broad band filter (F814W) and a red-green-blue (RGB) image combined of three VISTA images.

Once described, galaxies will be categorized in distinctive groups in an attempt to characterize the findings qualitatively and quantitatively.

Several strong emission lines are expected to lie in NB118 at redshifts higher than 2.5. One of the strongest is the resonant MgII doublet $\lambda\lambda$2796, 2803 which is expected to be found at $z = 3.26$. Emission lines at lower wavelengths (thus higher redshift) are also considered since there is no upper bound on the redshift selection.

2 | Theory

In order to interpret the results properly, a basic background for galaxy formation and evolution is provided. Central aspects of galaxy classification such as star formation rate and stellar masses are described through the theoretical framework of initial mass functions and stellar populations coupled to empirical and simulated results.

2.1 Galaxy formation and evolution

The subject of how a galaxy is formed and evolve is fundamental to understanding the results of this study with the main emphasis on evolution. The presence of galaxies across cosmological length and time scales requires the discussion of them to involve cosmology, though.

Throughout this study, a ΛCDM cosmological model is assumed with $\Omega_\Lambda = 0.7$, $\Omega_{DM} = 0.21$, and $\Omega_{\text{baryons}} = 0.04$.

2.1.1 Initial conditions and structure formation

In the very early universe, small density perturbations were generated from quantum fluctuations such as those invoked in the inflationary theory. These perturbations grew in time due to the fact a slightly over-dense region will attract matter while under-dense regions became more rarefied. In a static universe, the density contrast $\delta\rho/\rho$ will grow exponentially in time, but in an expanding one, the expansion damps accretion flows and the growth rate is usually a power law of time $\delta\rho/\rho \propto t^\alpha$.

At some point, the perturbation reaches over-density $\delta\rho/\rho \sim 1$ and the matter within the physical size begins to collapse gravitationally. The dominant matter part is dark matter, and they collapse to form dark matter halos. Baryonic matter is also attracted and is shocked to the virial temperature of the halo.

The gas can settle further down the potential well if it is sufficiently cooled. Various cooling mechanisms exist and are highly dependent on the virial temperature. Bremsstrahlung takes places in the hottest halos, excitation and de-excitations play a role in cooler halos and is highly dependent on the atomic species, and lastly is inverse compton scattering of the cosmic microwave background in high redshift galaxies.

Generally speaking, cooling is most effective in higher density regions but the net effect of cooling is the same: the baryonic matter segregates from the dark matter and accumulates as dense, cold gas at the center of the dark matter halo. A protogalaxy is formed. Furthermore, if the baryonic matter retains some of its angular momentum and settle in a cold disk in centrifugal equilibrium in the center of the halo.

The dark matter halos are not single isolated systems, though, and the interaction between halos may cause them to merge and grow hierarchically in size.

2.1.2 Star formation

Star formation is an important aspect in the study of galaxies since the light from a galaxy is the cumulative light of its stars. Obviously, intrinsic properties of a galaxy, such as metallicity, age, and type influence the light. By and large, though, one has to describe how stars form in order to understand galaxy formation and evolution since the light emitted by a galaxy is the cumulative light from its stars. There are two broad areas of star formation: microphysics and macrophysics[1]. Microphysics is a term that

[1]Following the distinction made in Mo et al. (2010) and their presentation of star formation.

covers the mechanisms behind individual star formation such as gravitational collapse of dense molecular clouds and star formation efficiency of GMCs whereas macrophysics covers formation and structure of molecular clouds in galaxies.

The nursing grounds for star formation are giant molecular clouds (GMC). These clouds are found in the cold gas of the interstellar medium (ISM) and are dominated by neutral hydrogen and to a significant degree, molecular hydrogen H_2. The fraction of H_2 depends greatly on the type of galaxy and location. In the Milky Way and other spiral galaxies, the cold gas consists almost entirely of H_2 near the center and the denser the gas, the higher the fraction of H_2. The largest of these clouds have masses of 10^5-10^6 $M_\odot$, densities of $n_{H_2} \simeq 100-500$ cm^{-3} and extend over tens of parsecs. Additionally, the clouds are clumpy in appearance with smaller substructures of denser clumps and cores. Star formation only occurs in the most massive clumps with masses of 10^2-10^4 $M_\odot$ and densities of $n_{H_2} \simeq 10^2$-10^4 cm^{-3} or cores with 0.1-10 $M_\odot$ and densities of $n_{H_2} > 10^5$ cm^{-3}. The former gives birth to star clusters while the latter to single stars.

GMCs are transient phenomena that appear to have a typical lifetime of $\sim 10^7$yr based on the fact that GMCs show no correlation with stars older than this. Star formation is also suggested to start as soon as a cloud is formed. Therefore, it is easy to draw the connection between the formation rate of stars being equal to the formation rate of GMCs. To better understand galaxies with star formation, it is vital to consider a number of processes that form clouds. There are two main groups of these processes: (1) cooling with subsequent molecule formation by itself that triggers gravitational collapse and (2) compression or collapse in turbulent or unstable gas that triggers the cooling and molecule chain of events.

One process that can trigger GMC formation is **turbulence** on scales of both GMCs or larger. Since GMCs are transient objects, it has been suggested that they form and dissolve at converging points in larger scale turbulent flow. These flows may be driven by cooling and accretion of gas in merging dark matter halos or energy injections in form of spiral density waves, supernova explosions, and protostellar outflows, stellar winds, and ionizing radiation from newly formed stars. Another process that can trigger GMC formation is **spiral arms** in spiral galaxies. The arms are believed to be spiral density waves that compress the gas swept alongside with them, which promotes thermal and gravitational instability. It is observed that there is an increased star formation rate (SFR) in the spiral arms of the Milky Way and other spiral galaxies. Finally, **galaxy interactions and mergers** cause gas to flow towards the center of the merger remnant, which increases the density manyfold hence giving rise to a nuclear starburst.

SFR is usually quantized in how gas is turned into stars in units of solar masses per year, $M_\odot\ yr^{-1}$. Sometimes, it is convenient to look at the ratio between the SFR and the stellar mass, $M_\star$, of a galaxy. This is referred to as the specific star formation rate (SSFR), which is given in units of yr^{-1}, though several authors tend to use units of Gyr^{-1} instead.

2.1.3 The initial mass function

With stars beginning to form, one can describe what kind of stars form. One way to look at this subject is to consider the mass spectrum, i.e the distribution of masses of newly formed stars. This is called the initial mass function (IMF) and is particularly important in creating synthetic spectra of galaxies. Additionally, the IMF determines the baryonic content, the chemical enrichment, and evolution of galaxies. In that sense, it is a fundamental pillar to how we view and understand galaxies. Formally, it can be written:

$$\int_{m_l}^{m_u} m\phi(m)\ \mathrm{d}m = 1\ M_\odot, \tag{2.1}$$

where m_l and m_u are the lower and upper mass limits for stars, and $\phi(m)\ \mathrm{d}m$ being normalized so to describe the number of stars born with masses in the range $m \pm \mathrm{d}m/2$ for every 1 $M_\odot$ of newly formed stars. The logarithmic form is also used (Chabrier, 2003):

$$\xi(m) = ln(10)m\phi(m), \tag{2.2}$$

The logarithmic slopes of the IMFs can be used for characterization:

$$\alpha(m) \equiv -\frac{\mathrm{d}\ \log\phi)}{\mathrm{d}\ \log m} \qquad \text{and} \qquad \beta \equiv -\frac{\mathrm{d}\ \log\xi)}{\mathrm{d}\ \log m} = \alpha - 1 \tag{2.3}$$

The very first quantization of IMFs is Salpeter (1955) and was presented as a power-law approximation, $\phi(m)\ \mathrm{d}m \propto m^{-\alpha}\ \mathrm{d}m$, where the Salpeter coefficient is $\alpha = 2.35$. Thus, the number of stars decreases rapidly with stellar mass.

Although very popular, the large number of brown dwarfs and low mass stars predicted by a Salpeter IMF are not consistent with observations (Chabrier, 2003). Additionally, description of the high mass regime has also been under scrutiny (Scalo, 1986), which found that the IMF is very consistent with large-scale observations in this regime. It also opened up the opportunity for different IMF for different types of formations, e.g single stars or clusters, although conclusions were tentative.

It is important to notice, though, that the IMF can not be directly observed. Any quantization of the mass distribution is based of the cumulative light of a stellar cluster or galaxy.

All in all, though, it seems that the IMF is universal (Bastian et al., 2010), and any variations of it in specific local and extragalactic environments usually have explanations for their deviations. An excellent use of IMFs is when taking stellar evolution into consideration - a subject that is well-described and well-understood - in order to produce synthetic spectra of galaxies. An example of using a different IMF for galaxy modeling is Daddi et al. (2007) who mention that using an IMF other than Salpeter will result in an overall lower SFR.

2.1.4 Stellar populations and formation

The light from a galaxy can be used to probe the stellar content. Since the luminosity and evolution of a single star is well understood, a synthesized spectrum can be made at any point in the life cycle of a star. Once you have an coeval ensemble of stars and you know the distribution of masses through the IMF, a spectrum for the ensemble can be made. Adding several ensembles together with different ages and sizes, different galaxy types (e.g recent starburst or red, dead galaxies) can be imitated.

Figure 2.1 shows an example of a synthetic spectrum of a starburst with only stellar light and not emission lines at different times in its evolution. In early times, it is dominated by the bright O and B stars. The lifetime of these are short, though, and much of the ultra violet radiation is gone after only 10-100 Myr. Other features are also dependent on age such as breaks in the continuum or spectral features. These characteristics carry over into the light of galaxies and can be used to examine their stellar populations.

More formally, the total stellar luminosity of a galaxy at a given wavelength can be written as:

$$L_\lambda = \int_0^t \mathcal{L}_\lambda^{cp}(t - t')\Psi(t')dt', \tag{2.4}$$

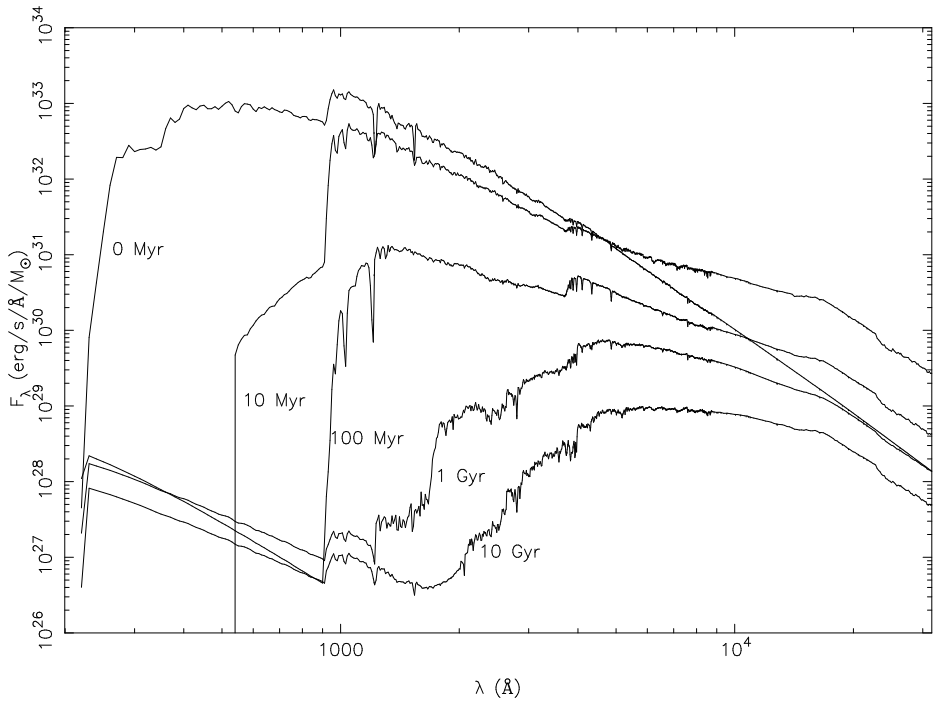

Figure 2.1: Energy distribution of a $1M_\odot$ starburst at various evolution times using a Salpeter IMF (Fioc and Rocca-Volmerange, 1997)

where $\mathcal{L}_\lambda^{cp}(\tau)$ is the luminosity per unit stellar mass of all stars of a coeval population (cp) of age τ, and $\Psi(t)$ is the star formation rate (mass turned into stars per unit time). Moreover, $\mathcal{L}_\lambda^{cp}(\tau)$ can be written as:

$$\mathcal{L}_\lambda^{cp}(\tau) = \int \mathcal{L}_\lambda(m,\tau)\frac{\phi(m)}{\mathrm{M}_\odot}dm, \tag{2.5}$$

where m is the mass of a star, $\phi(m)$ is the normalized IMF (equation 2.1), and $\mathcal{L}_\lambda(m,\tau)$ is the luminosity of a star with initial mass m at age τ. With these equation, the SED can be found at any time once star formation rate, $\Psi(t)$ and IMF, $\phi(m)$ are specified (Mo et al., 2010). As mentioned earlier, the IMF is not directly observed but inferred through the luminosity function as just described.

Galaxies with a star formation history that only lasts for a short period can be explained by a delta function, $\Psi(t) \propto \delta(t-t_{\mathrm{form}})$. This means that the luminosity function is basically given as $L_\lambda(t - t_{\mathrm{form}}) = \mathcal{L}_\lambda^{cp}(t - t_{\mathrm{form}})$ and the spectrum is more or less figure 2.1. These galaxies are said to have *passive evolution*.

Two other spectral features are associated with an evolving coeval population; the Lyman break at 912 Å break and the 4000 Å break, which also can be seen in figure 2.1. The Lyman break become more and more pronounced at an age of $\sim 10^7$ yrs when the most massive stars move off the main sequence. A large amount of UV photons are generated at an age of $\sim 10^9$ yrs due to the remaining stars spending a lot of time in the post asymptotic giant branch phase. Like the 4000 Å break, it can be used as a diagnostic tool for SFR and stellar mass (Mo et al., 2010). The 4000 Å break, however, is a more robust tool since the amplitude of the break increases almost monotonically with age from $\sim 10^7$ yrs (Mo et al., 2010). The break is due to the increased optical depth of the stellar atmospheres of G and K stars due to metal absorption. Additionally, it provides an excellent tool in

studying the SF histories of galaxies (Kauffmann et al., 2003; Kriek et al., 2011), although it is sensitive the metallicity.

The strength of the breaks can be quantized as follows:

$$D(912) = \int_{1000}^{1100} F(\lambda)\,\mathrm{d}\lambda \Big/ \int_{800}^{900} F(\lambda)\,\mathrm{d}\lambda\ ; \tag{2.6}$$

$$D(4000) = \int_{4050}^{4250} F(\lambda)\,\mathrm{d}\lambda \Big/ \int_{3750}^{3950} F(\lambda)\,\mathrm{d}\lambda\ , \tag{2.7}$$

where the integration limits are taken from Mo et al. (2010). The strength of the breaks can be used to decide the age of a stellar population. As figure 2.1 suggests, the strength of the Lyman break changes with age and is largest at ages betweem 10-100 Myr. Observing a strong Lyman break is thus indicative of a recently formed stellar population. The integration limits indicate that a spectrum is required, but broad band filters may also be used given that they approximately cover the same wavelengths.

Other star formation tools include continuum and line emission. Stars with $m > 5M_{\odot}$ have short life times and emit most of their energy as UV continuum radiation. A UV continuum in a galaxy is therefore indicative of recent star formation as long as the radiation is not absorbed on its way to the observer. In case of a dusty star forming region, much of the UV produced by all stars can be absorbed by the dust and re-emitted as far-infrared (FIR) radiation. Thus, a FIR continuum can also be used as a SFR diagnostic. Emission lines include nebular lines from recombination of hydrogen in the interstellar medium ionized by young, massive stars. Hα is the most commonly used line, but other lines from the Lyman, Paschen or Brackett series can also be used. Forbidden and semi-forbidden lines can also be used provided their emission is strong. A common line for this is [OII] (Mo et al., 2010), but certain UV lines can also be used such as CIII] (Stark et al., 2015).

2.1.5 Galaxy main sequence of star formation

Star-forming galaxies follow a strong correlation between SFR and stellar mass and hence form a main sequence of star formation (MSSF), both in the local universe (Daddi et al., 2007; Rodighiero et al., 2011), at intermediate redshifts, and at higher redshifts (Daddi et al., 2009). Figure 2.2 shows the MSSF as found in Daddi et al. (2007) for galaxies at $z \simeq 2.$ (the black solid line) overplotted with galaxies from two different fields.

It is suggested, though, that there is a tighter correlation between stellar mass and SSFR rather than SFR (Rodighiero et al., 2011; Daddi et al., 2009). Another factor that influences the main sequence is the redshift. It is established that the SFR was higher in earlier universe (Karim et al., 2011) and has since dropped to a lower level.

While 4 out of 5 datasets presented in figure 2.3 only examined the star formation history out to $z \simeq 3$, Hopkins and Beacom (2006) has examined it further back to $z \simeq 6$ and found that the maximum SFR happened near $z = 3$ and consequently dropped of towards higher redshifts.

2.2 Galaxy types

Having established one of the most important processes in generating the light distribution and appearance of a galaxy, it is now time to consider a range of different galaxies that may be found in this study. While the following discussion describes galaxies with very different histories or properties, the galaxies that are expected to be found may very well be something in between two or more types.

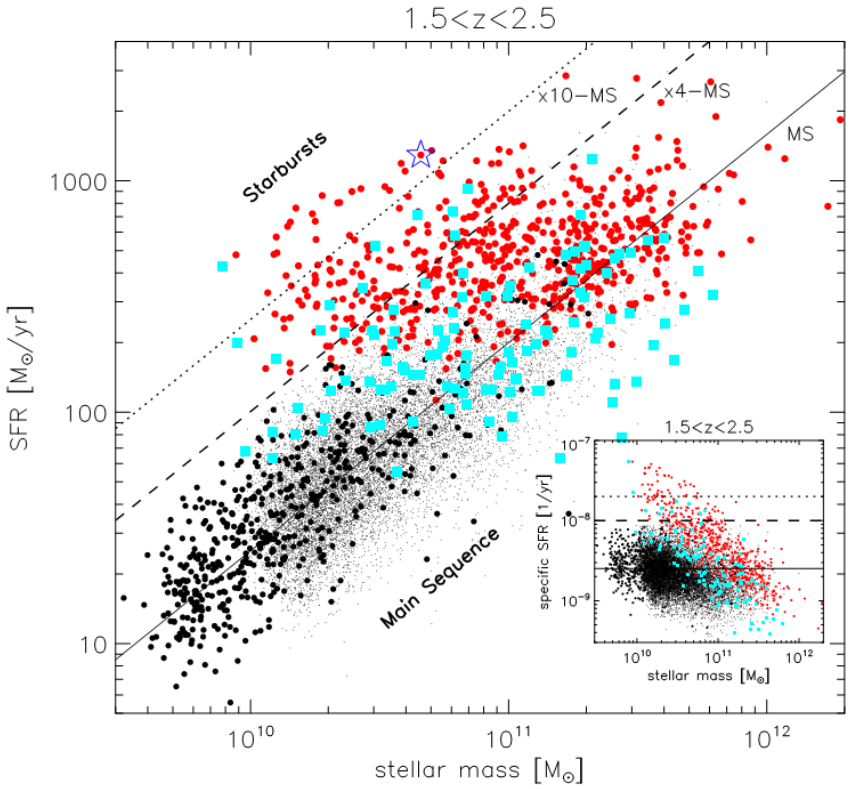

Figure 2.2: Figure from Rodighiero et al. (2011). It shows the stellar mass and star formation relation at $1.5 < z < 2.5$. It includes four main samples of data:the "shallow" PACS-COSMOS sources (red filled circles), the deeper PACS-GOODS South (cyan squares), the BzK-GOODS sample (black filled circles) and the BzK-COSMOS sources (black dots). Additionally, a black solid line indicates the main sequence as given by Daddi et al. (2007) (SFR= $200M_1^{0.9}1$ where M_{11} is the stellar mass in units of 10^{11} $M_\odot$. The dashed line is 4*MS and the dotted line is 10*MS)

The main types of galaxies considered are star forming galaxies that are identified by a moderate SFR and a range of stellar masses and appear to lie on the MSSF. Quiescent galaxies are dominated their high infrared flux combined with high stellar masses and low SFR. Another type of galaxies are found to be interacting with another galaxy, which produces morphological disturbances and often accompanied by high SFR. The last type is galaxies whose light is not dominated by stellar emission but rather nuclear emission. This includes both the continuum and emission line radiation.

2.2.1 Star forming

Star forming galaxies are usually spiral galaxies (Mo et al., 2010) whose morphology is favorable for creation and collapse of GMC. The clouds, being mostly hydrogen, are then ionized by the newly created O and B stars to form HII regions. Free electrons can pair up with the ionized hydrogen and give rise to a series of recombination lines, which are direct tracers of recent star formation. The most common tracer lines are Hα, but other recombination lines such as Hβ, Pα, Pβ, Brα, and Brγ can be used as well (Kennicutt, 1998).

At higher redshift, Hα becomes less accessible, and other nebular emission lines can be used as tracers. [OII] can be a fair alternative, although it is affected by the presence of dust that absorbs the flux emitted at UV and optical wavelengths, and re-emits it at longer wave-lengths in the infrared (IR) regime (Gilbank et al., 2010; Talia et al., 2015).

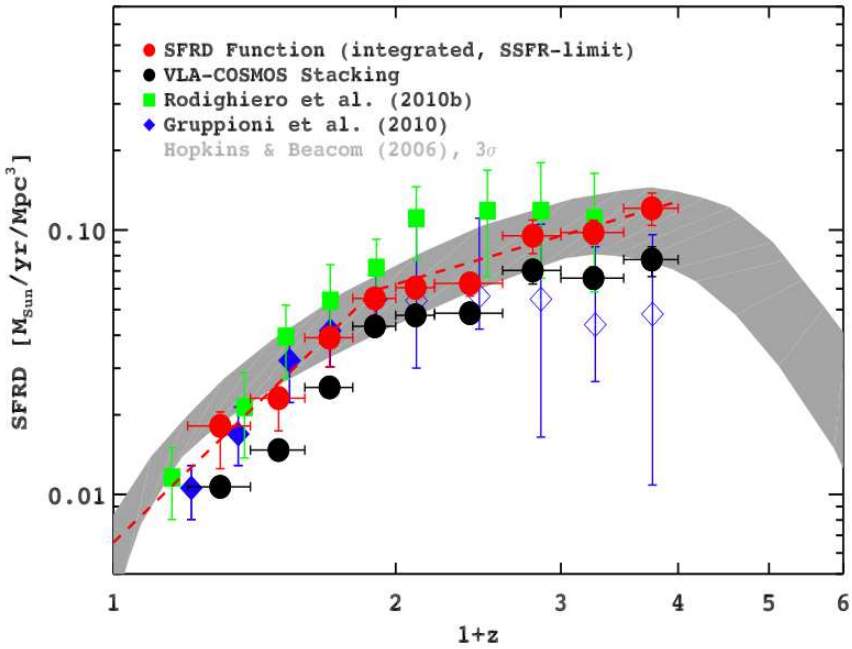

Figure 2.3: Evolution of SFR density as a function of z (Karim et al., 2011).

Given the constant creation of new stars at a moderate pace, some continuum features such as the 4000Å break are weak but still present due to a presence of a moderately large old population. The Lyman break is also significantly smaller because of the dispersion in stellar age.

2.2.2 Quiescent galaxies

The star formation history of some galaxies are characterized by a short spurt of star formation after which it has quieted down. The massive stars died off quickly and have left the galaxy off with a population of $\lesssim 1$ $M_\odot$ stars after a few Gyr whose emission is mainly the red wavelengths due to many of them being on the giant branch in an H-R diagram (Mo et al., 2010). Such galaxies are said to be passively evolving.

The 4000 Å break becomes prominent in such galaxies whereas the Lyman break becomes difficult to distinguish due to an increase in UV flux caused by the post-AGB stars.

2.2.3 Mergers and tidal interactions

A galaxy in the vicinity of other galaxies can have its gas content disturbed which can have drastic effects on its SFR. Gas losing its angular momentum can cause it to surge for the central regions of a galaxy and increasing the gas surface density. This makes advantageous conditions for the formation of molecular clouds which in turn greatly increases SFR and giving rise to a nuclear starburst.

These galaxies are dominated by the light of young O and B stars and see a prominent Lyman break while the 4000 Å is very weak. However, dusty galaxies will result in a lot of the UV radiation being absorbed and re-emitted as infrared light. Extremely luminous infrared galaxies, or ULIRGs, show signs of extremely high SFR and tidal interactions such as tails, shells, and complex velocity fields (Mo et al., 2010).

2.2.4 Active galactic nuclei

A last type of galaxy is somewhat different than the ones discussed since most of its light is not of stellar origin. The light is instead emitted from a very small area within the center of a galaxy which nowadays is believed to be a complex process of accretion of gas onto a super-massive black hole (SMBH). This produces a large amount of UV ionizing photons that ionize surrounding clouds and give rise to broad- and narrow emission lines with velocity dispersions of up to ~ 10000 km/s.

Some AGNs dominate the light of their host galaxy more so than others. A subtype, Seyfert galaxies, exhibit luminous central regions and emission lines not associated with star formation but with its host galaxy clearly visible. Another type, quasars, completely dominate and the light from the host galaxy causing the host galaxy to be difficult to distinguish.

The formation of AGNs is also a subject of debate. Nuclear starbursts give rise to extremely luminous galaxy cores and if infalling gas can lose further angular momentum, it may start feeding the SMBH (Mo et al., 2010).

Furthermore, AGNs have been found to quench the SFR due to feedback processes Bower et al. (2006).

2.3 Filters

An important instrument for doing large scale surveys is the use of filters. Their purpose is to only let certain wavelengths through, which then is measured on a CCD. Using several different filters gives an energy distribution and form a sort of low resolution spectrum. Advantages of using photometry rather than spectroscopy are the large sky coverage and comparatively lower exposure times required. However, a large area of the sky contain a large number of objects. In order to describe a single object, certain actions are required, which will be described shortly.

Different telescopes and detectors are optimized for different wavelengths and thus use different filters. Filters can generally be characterized by their central or effective wavelengths and their widths. Some of the most used filters are given in table 2.1. However, filters also come in an intermediate and narrow version. Narrow bands generally have widths of $\sim$ 1.5% of their central wavelengths, intermediate bands have $\sim$ 5% while broad bands have widths of $10 - 20\%$ of their central wavelength.

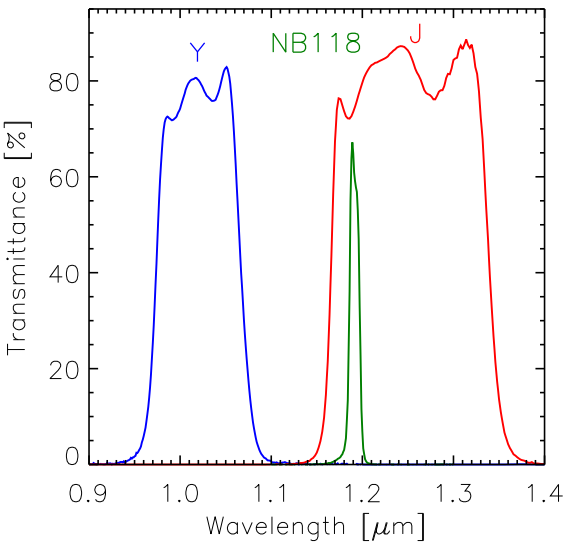

Figure 2.4: Used filters in this study, figure from Milvang-Jensen et al. (2013)

Different types of filters have different uses. Broad bands are not as sensitive to short wavelength interval effects such as spectral lines and are thus excellent for continuum measurements. Narrow bands are on the other hand more sensitive to effects such as emission lines. However, this works in their favor since they can be used to probe for spectral lines at shorter wavelengths that have been redshifted to the wavelength of the band.

Across their wavelength interval, filters are not equally sensitive to incoming light. The response of a filter to light at different wavelengths can be measured and plotted as a

transmission curve. An example is figure 2.4 which shows the transmission curves of some of the filters used in this study.

2.3.1 Filters used in this study

Three filters used for candidate selection in this study: two broad bands (Y and J) and a narrow band (NB118). Their central wavelengths are 10200 Å, 12520 Å, and 11910 Å with widths of 930 Å, 1720 Å, and 123 Å, respectively. The transmission curves of these can be seen in figure 2.4. Measurements from a catalog from Laigle et al. (submitted) (COSMOS2015) is also included and use a much wider range of filters (see table 2.1).

As mentioned previously, narrow bands enable search for emission lines. In the case of NB118, it is located within the J band. As such, a continuum flux can be inferred from J and a difference in flux between J and NB118 is thus indicative of a spectral line situated in NB118. Which spectral line it is depends on the redshift of the target object. Due to the width of the narrow band, only specific redshifts will result in a strong emission line in NB118. Milvang-Jensen et al. (2013) mention Hα emitters at $z = 0.8$, Hβ and [OIII] emitters at $z \approx 1.4$, and [OII] emitters at $z = 2.2$. These are among some of the most prominent lines.

There are a number of other lines that are also interesting, though. They are not as common which make them interesting for this study. A number of other interesting lines is shown in table 2.2. Throughout this thesis, referred lines are the one in the table unless stated otherwise.

Instrument / Telescope	Filter	Central λ (Å)	Width (Å)
GALEX	NUV	2313	748
MegaCam/CFHT	u^*	3823	670
Surprime-Cam/Subaru	B	4458	946
	V	5477	1382
	r	6288	1382
	i^+	7683	1497
	z^{++}	9105	1370
intermediate bands	IA427	4263	206
	IA464	4635	218
	IA484	4849	228
	IA505	5062	230
	IA527	5261	242
	IA574	5764	271
	IA624	6233	300
	IA679	6781	336
	IA709	7073	315
	IA738	7361	323
	IA767	7684	364
	IA827	8244	343
narrow bands	NB771	7119	72
	NB816	8149	119
HSC/Subaru	Y	9990	820
VIRCAM/VISTA	Y	10214	970
	J	12534	1720
	H	16453	2900
	K_s	21539	3090
	NB118	11910	123
WIRCam/CFHT	H	16311	3000
	K_s	21590	3120
IRAC/Spitzer	ch1	35634	7460
	ch2	45110	10110
	ch3	57593	14140
	ch4	79594	28760

Table 2.1: A selection of filters used in COSMOS (Laigle et al., submitted).

An example is MgII. MgII is a resonant doublet at 2796 and 2803 Å and is often seen as absorption in galaxy spectra (Kornei et al., 2013) due to a range of phenomena including circumgalactic medium absorption, infalling gas, and outflowing galactic scale winds (Nielsen et al., 2013). MgII *emission*, though, is not as common and may be indicative of highly ionizing processes, AGN activity, or high SFR (Kornei et al., 2013; Roig et al., 2013). Even with very high SFR, Weiner et al. (2009) found only ∼4% e of 1406 star-forming galaxies had MgII emission. The other lines mentioned in table 2.2 will be discussed when encountered in

NB118 lines and redshift

z	Line	λ_{rest} (Å)
Prominent lines[a]		
0.8	Hα	6563
1.4	Hβ+[OIII]	4861+4959,5007
2.2	[OII]	3727
Other lines		
2.5	[NeV]	3347, 3427
2.7	HeI	3187
3.3	MgII	2796, 2803
3.9	[NeIV]	2422, 2424
4.1	CII]	2326
5.2	CIII]	1908

Table 2.2: [a]: Mentioned in Milvang-Jensen et al. (2013). Other lines are emission lines considered in this study.

chapter 5.

2.3.2 Photometric measurements

Having a wide range of filters also makes it possible to create a spectral energy distribution (SED), which is a measure of brightness as a function of wavelength. In that sense, it is similar to a spectrum, albeit a low-resolution one. However, the extraction of brightness of a single object is unlike that of spectroscopy. A single image may cover a large area of the sky and as such contain a large number of objects. Therefore, an object needs to be identified first, but it needs to be determined which parameters make an object. Then, the brightness of an object is measured which there are many methods of. Photometric measurements are therefore complex in both their preparatory phase but also at the point of measuring.

These considerations are described in detail in chapter 3 where the program Source Extractor (SExtractor (Bertin and Arnouts, 1996)) is used and these parameters are explained. Basically, one way to identify an object is to consider how much brighter an area is compared to the background, and if it is a certain amount brighter, it is considered an object. The size of the object is the total connected area that has increased brightness. The exact position may be found by saying the brightest spot is the center or that the weighted brightness average is.

Once the position has been established comes the point of measuring the brightness. First, the area in which the flux is measured needs to be decided. There are several methods for this, including fixed circular apertures, isophotal area of an object, and flexible elliptical apertures. This is described further in chapter 4. Flux is measured in units of energy per second per area per wavelength. Throughout this study, AB magnitudes are used, and the conversion from image measurements to magnitude is:

$$m_{ab} = -2.5 \log_{10}(f) + Z_p, \tag{2.8}$$

where m_{ab} is the magnitude, $Z_p = 30.00$ is the zero-point, which is dependent on the specific instrument and conversion[2], and f is the measured pixel value in ADUs for the

[2] $Z_p = 30.00$ is true for UltraVISTA images, but other images such as those from the Subaru telescope, $Z_p = 31.4$

A given error in the flux will carry over in magnitudes in the follow form:

$$m_{error} = \frac{2.5\, f_{error}}{\ln(10)\, f}, \tag{2.9}$$

where m_{error} is the error in magnitude and f_{error} is the error in ADU. Only the error to the first order is included.

3 | Data

In this study, two types of data are used: Three images (Y, NB118, J) from VISTA on which this study performs source extraction and photometric measurements and a catalog from Laigle et al. (submitted) containing photometric measurements in several (∼35) other filters from various telescopes. Both datasets cover the Cosmological Evolution Survey field (COSMOS; Scoville et al. (2007)) - an area of the sky that covers 2 square degrees. This chapter will explain some of the technical details of these datasets

The VISTA images are taken from the UltraVISTA survey (McCracken et al., 2012; Milvang-Jensen et al., 2013), which has had two data releases so far and covers a slightly smaller area compared than the while COSMOS field. A third (DR3) and, at the time of writing, unreleased one is used for this study. The filters that will be used are two broad bands (Y and J) and one narrow band (NB118). They are centered at 10215 Å, 12535 Å, and 11910 Å respectively. The catalog is obtained from Laigle et al. (submitted) which is a large catalog of precise photometric measurement, redshifts, and stellar masses of more than half a million objects in the COSMOS field. It uses images from 7 instruments on 5 telescopes ranging from near ultra-violet data to infrared data. It also contains UltraVISTA data but uses data release 2 (DR2) and do not include NB118 photometry.

3.1 COSMOS

COSMOS is an astronomical survey that aims to describe the evolution and formation of galaxies by using a large compilation of data collected by a number of telescopes observing the same area on the sky. This area is called the COSMOS field and is covered by most of the major space-based telescopes and several large ground based ones. It is a two square degree equatorial field centered at $\alpha = +150.11916667$ (10:00:28.600), $\delta = +2.20583333$ (+02:12:21.00) in J2000 coordinates. Almost 300 papers related to COSMOS have been published.

The many telescopes cover wavelengths ranging from x-ray to radio (see figure 3.1). This section will briefly cover most of the instruments and telescopes alongside with their contribution to COSMOS.

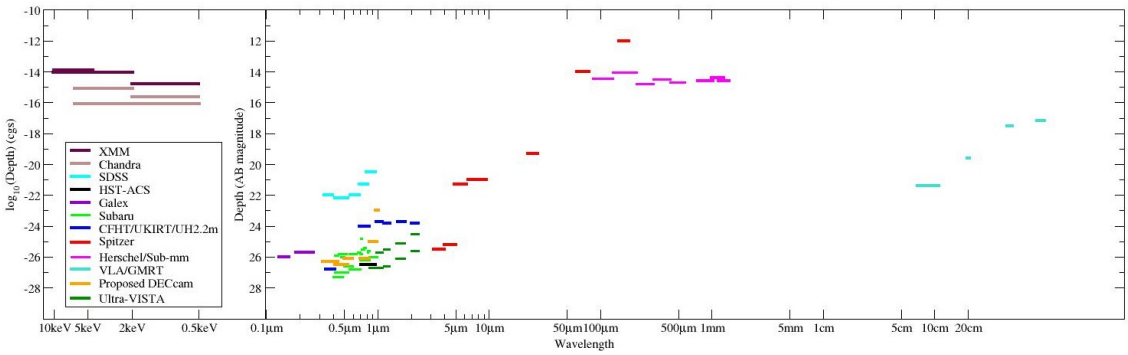

Figure 3.1: 5σ depths of all existing data in COSMOS. For a larger resolution, see `http://cosmos.astro.caltech.edu/page/astronomers`.

3.1.1 Hubble Space Telescope

The Hubble Space Telescope (HST) was allocated 640 orbits in cycles 12 and 13 but only used 590 due to the fact that a group of high-redshift pursuers was granted 50 orbits.

The Advanced Camera for Surveys (ACS) instrument on board obtained a 27.2 10σ AB magnitude depth in the F814W band, which covers 1.8 square degrees and has a resolution of 0.05"/pixel. Additionally, several other filters (F475W, F606W) were also used on smaller areas (0.03 and 0.05 square degrees) for other surveys .

The high resolution and large coverage of the F814W image makes it invaluable in describing the spatial extent of objects in the COSMOS field - especially at high redshift. This is also the declared primary scientific goal of the F814W images (Koekemoer et al., 2007). The reason for using this filter is its location at red wavelengths as well as exceptionally high transmission (>90-95%) across a wide wavelength range ($\sim$ 7300-9500 Å). Its wavelength location is especially important for high redshift objects since their fluxes are shifted to more red wavelengths.

Thus, the usage of HST in COSMOS is important in order to resolve the morphology of high redshift objects.

3.1.2 X-ray

Two x-ray space telescopes are employed for COSMOS: XMM-Newton and Chandra. They cover roughly the same wavelengths for broad band imaging (1-25 Å) and have both surveyed the entire 2 square degrees field. Additionally, they also proved spectroscopic measurements in similar wavelengths

Their mission is to study black holes and the formation of galaxies amongst other things. The photometric measurements provided by the broad bands are not utilized in the catalog from Laigle, but the images are used to check for x-ray emission in hopes of finding extremely energetic processes.

3.1.3 GALEX UV

The Galaxy Evolution Explorer (GALEX) is a space telescoped placed in a 690 km and 29 degrees inclination orbit whose goal is to perform imaging and spectroscopic surveys of most of the sky. The surveys are of various depths and details and are made using two ultraviolet bands: Far UV (FUV, 1350-1780 Å) and Near UV (NUV, 1770-2730Å).

GALEX has observed the COSMOS field for 100 hours and provide depths of 26 AB magnitudes. These data points are the lowest wavelength photometric measurements used and provide valuable information below the Lyman break for high redshift objects.

Although data from GALEX are included in the catalog from Laigle et al. (submitted), it has not been included in this study due to late arrival of the final catalog.

3.1.4 VISTA NIR

Near infrared (NIR) data come from two telescopes with one of them being the Visible and Infrared Survey Telescope for Astronomy (VISTA). It has contributed to three key surveys for COSMOS: Deep, ultra-deep and narrow-band. The first two use the Y, J, H, and Ks broad bands and cover 1.8 and 0.9 square degree respectively. The narrow-band survey makes use of the NB118 band and covers the same area as the ultra-deep survey (Milvang-Jensen et al., 2013). The broad bands are centered at 10214, 12535, 16453, and 21540 Å while the narrow band is centered at 11910 Å.

The name of the survey is UltraVISTA (McCracken et al., 2012) due to the ultra deep images it provides of the COSMOS field. These images are instrumental to this study since it is from these that candidate selection is made. In section 3.2, a deeper explanation and analysis of VISTA and the UltraVISTA images is given.

3.1.5 Subaru UV/optical/NIR

The Subaru telescope is Japanese and is situated on the summit of Mauna Kea on the island of Hawaii. It is a large contributor to COSMOS with its 20 different bands; 6 broad bands (B, V, g, r, i, z^+), 12 intermediate bands (IA427, IA464, IA484, IA505, IA527, IA574, IA624, IA679, IA709, IA738, IA767, IA827), and two narrow bands (NB711, NB816). These images are made using the SuprimeCam instrument. Observations were made in the period of January 2004 to April 2005 for the broad bands and one narrow band while the observations for the rest of the bands were made January 2006 and March 2007. The broad bands reach 3σ depths of up to 27.2 AB magnitude while the intermediate bands reach 25.9 in 2" aperture. Recently, the Hyper Suprime-Cam contributed with Y band data to COSMOS as well.

Thus, Subaru covers a large wavelength area (4460-9105 Å) with its 6 broad bands and provides low resolution spectroscopy (Taniguchi et al., 2015) in those wavelengths through its 12 intermediate bands. The two narrow bands can be used to search for spectral lines much like the method in this study.

3.1.6 Spitzer MIR

Spitzer has conveyed the COSMOS field for 4 large programs: S-COSMOS, COSMOS-IRS, SEDS, and SPLASH. All programs covered the entire field except SEDS, which only covered 0.2 square degrees. One of Spitzers three instruments is the InfraRed Array Camera (IRAC) which has 4 channels at wavelengths of 3.6, 4.5, 5.8, and 8.0 μm. The widths of these channels are large: 0.75, 1.02, 1.43, and 2.91 μm. The SPLASH (Spitzer Large Area Survey with Hyper-Suprime-Cam) survey was done during cycle 9 (November 2012 - March 2014) and 10 (December 2013 – October 2014)

The wavelengths of Spitzer are valuable in determining light emitted from gas or dust and prove important when determining photometric redshift or total stellar mass of distant galaxies.

3.1.7 Herschel FIR

Two large programs have observed the COSMOS field: The PACS Evolutionary Probe (PEP) and Herschel Multi-tiered Extragalactic Survey (HerMES). Both surveys have covered the entire field though with different instruments. PEP has used the Photodetector Array Camera & Spectrometer (PACS) and its two bands at 100 μm and 160 μm while HerMES has used the Spectral and Photometric Imaging Receiver (SPIRE) with three bands at 250μm, 350μm and 500μm.

The two programs state similar goals as the Spitzer surveys though with an advantage of bing able to probe even higher redshift galaxies.

3.1.8 Sub-millimeter and millimeter

A wide range of telescopes and instruments has been utilized for COSMOS with coverage ranging from 0.07 (GISMO) to 0.75 (LABOCA) square degrees. The wavelengths of the sub-millimeter (submm) surveys range from 0.45 mm (JCMT/SCUBA-2) to 2.0 mm (GISMO). Their contribution to COSMOS consists especially of studying the so-called sub-millimeter galaxies (SMG), which are speculated to be highly redshifted ultra-luminous infrared galaxies (ULIRG). ULIRGs are massive galaxies with extreme SFR and submm luminosity.

3.2 VISTA data

The VISTA itself is a 4 meter wide-field telescope that is designed for deep optical and infrared surveys with a mosaic of 16 detectors on the instrument VISTA Infrared Camera (VIRCAM). It is located in Chile on the Paranal Observatory, which also houses the VLT. It has a 1.65 degree diameter field of view and its 67 Mpixels yield an active pixel area of 0.6 square degrees.

It is a mosaic of 16 detectors and in order to cover the whole area or stripe, an observing pattern combined with offsets must be employed. This section will describe the observational details about the data set used for this study as well as potential problems in the data set.

3.2.1 Data set

The key difference of DR3 to previous releases is an ample increase in exposure time in the four ultra deep stripes. It contains data from December, 2009 to approximately May, 2014.

It has first been processed by the VISTA Data Flow System (VDFS), which consists of quality control pipelines at ESO Paranal and Garching and then in a science reduction pipeline by The Cambridge Astronomy Survey Unit (CASU).

The data available from CASU consist of sky-subtracted images with corresponding sky frames, flat fields, bad pixel maps and stracked `_st` images. Weight maps are also available, but they are made by McCracken et al. (2012) themselves.

The area covered by the images and different surveys can be seen in figure 3.3. The exposure time for Y, J, and NB118 (i.e the filters used in this study) have ultra-deep exposure times of 53.2, 34.9, and 22.8 for DR2[1] while they are 105.3, 102.6, and 65.3 for DR3 (Milvang-Jensen, priv. comm.).

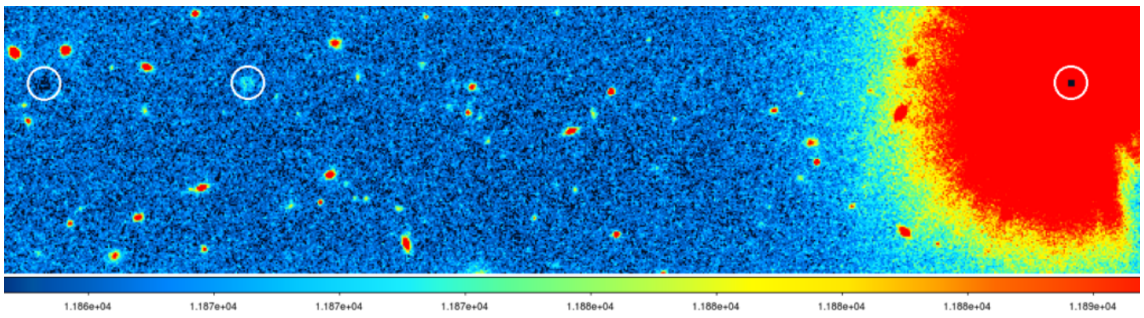

Figure 3.2: An example of cross-talk

Addionally, an RGB image is used for analysis of the objects and it is provided by Bo Milvang-Jensen. It is calculated from the UltraVISTA DR3 H, NB118 and Y images. This is for visualisation purposes: narrow-band excess is not defined from this RGB image. This RGB has H in the red channel (rather than J) simply to have a red band that does not include the emission line that falls in NB118 and J. The Lupton et al. (2004) method for constructing RGB images was used: this has the advantage that pixel that reach the saturation limit used in the construction of the image will appear with the correct color (e.g. green for objects with strong narrow-band excess) instead of white. The method also includes a non-linear scaling.

[1] `http://www.eso.org/sci/observing/phase3/data_releases/uvista_dr2.pdf`

3.2.2 Faults and defects

Given the design of the instrument, 16 NB118 filters are required (one for each detector). Each filter has different response curves (Milvang-Jensen et al., 2013), although the differences are small, and reacts differently to e.g ambient temperature.

An additional problem with the images is cross-talk which is when a signal from a readout channel appears in other readout channels. An example can be seen in figure 3.2[2]. It was believed until recently that VIRCAM had no cross-talk, but Rebecca Bowler and others from the UltraVISTA team found a weak effect in VISTA data. This is a problem that is expected to be encountered in data and candidate selection. In order to minimize its impact, selected candidates are visually inspected and rejected if they are cross-talk objects.

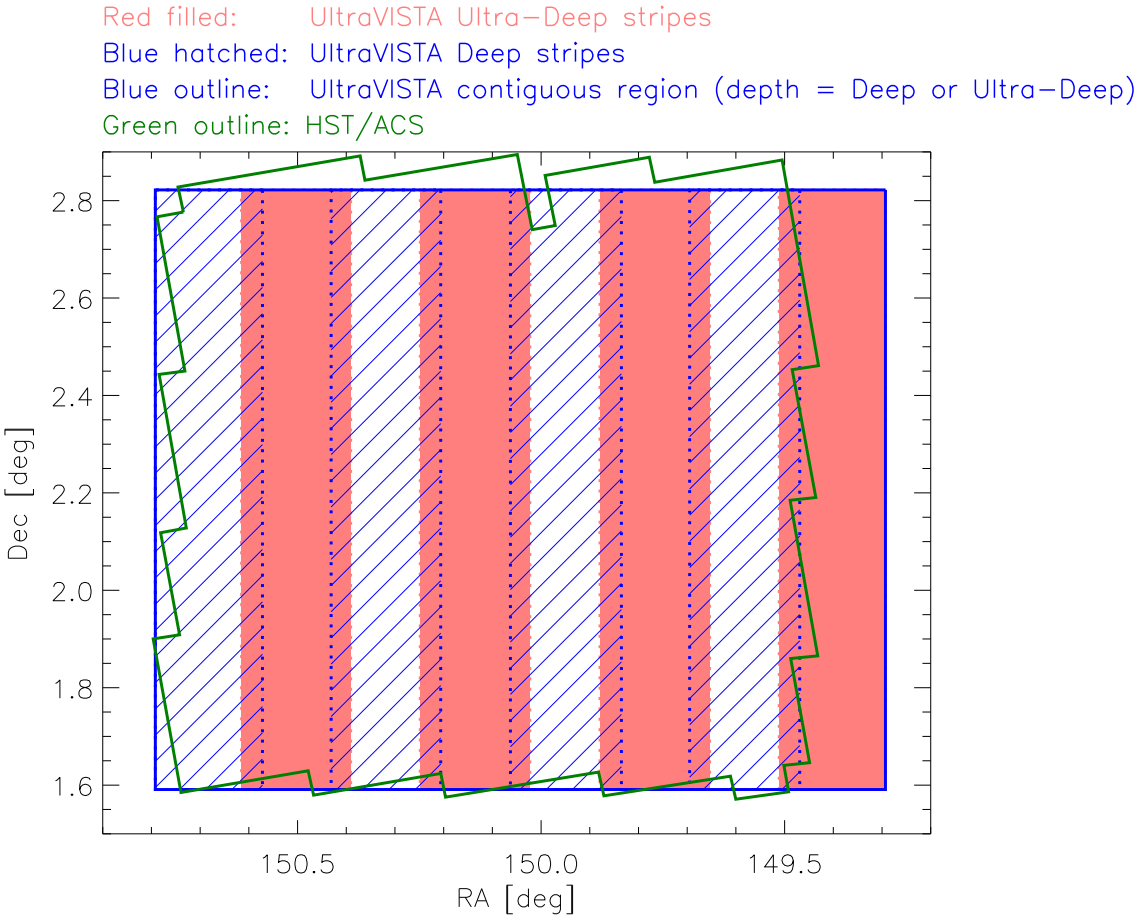

Figure 3.3: Schematic layout of UltraVISTA observations showing the different stripes (Deep and UltraDeep). Taken from McCracken et al. (2012).

3.3 The COSMOS2015 catalog (Laigle)

All external data used is retrieved from Laigle et al. (submitted). Data files are not publicly available yet, but permission was granted for this study. Laigle et al. (submitted) present a catalog with precise photometric redshifts and stellar masses for more half a million objects in the COSMOS field. This is done using the newest available images from various filters from number of telescopes. In comparison to earlier catalogs, this one has lower rates of

[2]From `http://www.eso.org/sci/meetings/2015/Rainbows2015/Talk_Files/DAY2/milvang_ESO_rainbows_conf_2015.pdf`

catastrophic redshift failures and higher accuracy. The catalog includes objects in both the whole field and in the ultra-deep stripes, which are the most interesting for this study.

Since this catalog is crucial to the selection of and descriptions of candidates, this section provides details and explanations on how the images are processed and the final catalog is made.

An important note is that the final catalog was obtained December, 16th, 2015 - a week before submission deadline. It has mostly been fully incorporated but some measurements have not been possible to update, in which case it will be mentioned.

3.3.1 Filter magnitudes

The catalog contains photometric measurements from near ultra-violet (NUV) from the GALEX to infrared measurements from Spitzer. The inclusion of Spitzer data as well as deeper near-infrared from UltraVISTA (DR2) is the main improvement over older catalogs
.

All in all, the catalog contains data from 5 different telescopes using 7 different instruments. It includes measurements from 32 different filters with 3σ depths of 24-26 AB magnitude in 3" apertures. The depths and locations of the various filters can be seen in figure 3.4. The transmission curves of the filters can be seen in figure 3.5.

The telescopes and instruments used are GALEX for NUV data, u^* band data from the Canada-Fance Hawaii Telescope (CFHT/MegaCam), and the COSMOS-20 survey from Subaru SuprimeCam for optical data. Near-infrared is obtained from the HSC instrument on Subaru, VIRCAM on VISTA (UltraVISTA DR2), and WIRCam om CFHT while infrared data is from the $3.6\mu m$, $4.5\mu m$, $5.8\mu m$, and $8.0\mu m$ channels on Spitzer.

An important step that is done for this catalog is *image homogenisation*. The profile of the point-spread-function (PSF) is homogenized between all the optical and near-infrared. This is to address the problem that the fraction of the total flux falling in a fixed aperture depends on the band.

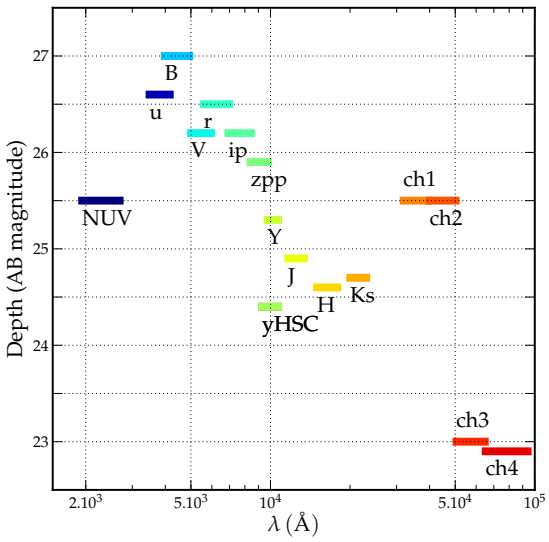

Figure 3.4: Limiting magnitude at 3σ in a 3" diameter aperture for most of the broad-band data used to compute the photo-zs in the COSMOS2015 catalog. From Laigle et al. (2015)

Once homogenisation has been performed, catalog extraction begins. It is done using SExtractor in dual image mode, i.e using one image for detection and another for source extraction. This procedure is described in much greater detail in chapter 4 since the same procedure is ones on UltraVISTA DR3 images. For detection image, this catalog utilizes a chi-squared $zYJHK_s$ image, which is produced by using SWarp on the non-homogenized images. The reason for using NIR and optical images for detection has to do with the purpose of the catalog; to probe the high redshift universe and include UV-luminous sources at $z > 2$. The z^{++} image is from Subaru while $YJHK_s$ is from UltraVISTA (DR2).

Source extraction is then done for each band with 2" and 3" diameter apertures. A few parameters are worth noting as these are discussed in detail in chapter 4.1 and chapter 5.1.2. First is `DETECT_THRESH`, which is the detection threshold and is set to 1.51. Secondly is `DETECT_MINAREA` - the number of contagious pixels an object is required to have to be

considered an object - which is set to 10. Last is the choice of using either a local or a global background for extraction. The catalog uses a local background estimated in a 30 pixels thick rectangular annulus around objects.

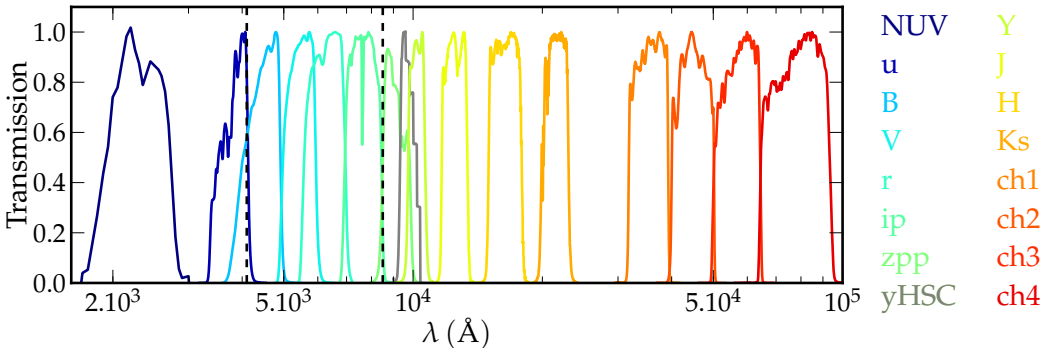

Figure 3.5: Filter transmission curves. The dashed lines show the wavelength area which the intermediate and narrow bands cover, though the transmission curve for these are not plotted. Taken from Laigle et al. (submitted)

Data from certain telescopes need special treatment. GALEX UV fluxes are measured using a PSF fitting method based on the u^* image as prior. Spitzer/IRAC SPLASH data are treated with IRACLEAN, which utilizes the position and morphological properties of sources in a high resolution image from a different filter. Laigle et al. (submitted) uses the chi-squared $zYJHK_s$ image as the prior for IRACLEAN.

Lastly comes the step of computing the photometric errors and upper limits. SExtractor errors are underestimated and require a correction factor Milvang-Jensen et al. (2013). This is found by taking empty aperture measurements in each band and then taking the ratio of the standard deviation of that flux to the median SExtractor error. The upper limits are found by taking the standard deviation of the fluxes in empty aperture measurements. For some bands, though, this value varies over the field and a different method is applied.

3.3.2 Photometric redshift

Once the photometry has been extracted, photometric redshift computations are made. The filters used for photometric redshift computations can be seen in table 2.1. This is done using the program LePHARE (Arnouts et al., 2002; Ilbert et al., 2006), which is a set of fortran commands to compute the photometric redshift. The basic idea is to use a set of galaxy templates and perform a χ^2 analysis between the predicted flux from these templates and the observed flux. The method is the same as performed in Ilbert et al. (2013).

3" aperture flux measurements are used for the computations as this gives slightly better redshifts at redshifts lower than 1. Additionally, they use fluxes for the computations rather than magnitude since it is more robust - especially on faint objects. Once the fluxes have been extracted, they use LePHARE, which is a set of fortran commands to calculate photometric redshift. It is based on color, i.e magnitude differences, rather than fluxes making it insensitive to global offsets.

The templates considered are 31 templates of spiral- and elliptical galaxies, 12 templates of young blue star-forming galaxies, and extinction as a free parameter with various extinction laws considered. For each template, fluxes in every band are predicted and a χ^2 analysis is performed between each template fluxes and observed fluxes of each object.

More precisely, the code finds the template T_{min} that minimizes at each redshift z_{step} in the following expression:

$$\chi^2(z_{step}) = \sum_{\text{filters}i} \frac{(F_{obs,i} - \alpha F_{SED,i}(z_{step}, T))^2}{\sigma^2_{obs,i}} \tag{3.1}$$

where $F_{SED,i}(z_{step}, T)$ is the flux predicted for a template T and α is the normalization factor. z_{step} runs from 0 to 6 in increments of 0.01. The value for each step can be stored and used to build a probability density function (PDF) at each redshift step. The $1-\sigma$ uncertainties enclose 68% of the area of the PDF around the median. This PDF of redshifts is referred to as the PDZ.

Photometric redshifts lack the accuracy that spectroscopic redshifts provide, though the methods for computing photometric redshifts are becoming increasingly better. One way to test how well a method works is to compute photometric redshift for galaxies that has a spectroscopic redshift and compare the two. The description method used in Laigle et al. (submitted) is the so-called normalized median absolute deviation (NMAD) and is given as:

$$\text{NMAD} = 1.48 \times \text{median}\left(\frac{|z_p - z_s|}{1 + z_s}\right) \tag{3.2}$$

where median is of the whole sample of galaxies with the two redshifts, and z_p and z_s are the photometric and spectroscopic redshift, respectively. This method is robust against catastrophic failures, which is given as $|z_p - z_s|/(1 + z_s) > 0.15$ and the percentage of failures is denoted η. 11 spectroscopic surveys have been used to test the accuracy of the photometric redshifts with a sample size of ~ 13500 galaxies.

Interesting for this study is the accuracy and catastrophic failure rate for high redshift ($3 < z < 6$) galaxies since selection and classification are made from the computed photometric redshifts. For this redshift interval, an accuracy of $\sigma_{\Delta z/(1+z_s)} = 0.021$ and catastrophic failure rate, $\eta = 15.0\%$ is found. Additionally, the errors on the photometric redshifts are multiplied by a factor depending on the brightness due to a systematical underestimation of errors from LePHARE.

Other properties extracted using LePHARE are stellar mass and SFR. A library of synthetic spectra generated using a Stellar Population Synthesis (SPS) model (Bruzual and Charlot, 2003). Laigle et al. (submitted) assume a Chabrier IMF and an exponentially declining star formation history combined with a delayed one. From the fit, stellar mass and SFR can be extracted. It is worth noting that Laigle et al. (submitted) do not intend include SFR from the template fitting in their distributed catalogs due to the uncertainties associated with template fitting. The SFR are available in the catalog used for this study, though, and will be used to characterize the selected candidates.

4 | Method

This section will describe the data processing - how images are treated, how the COSMOS2015 catalog is used, and how it is all put together. Many parameters can be tuned to influence the data flow. Some are crude while others only yield small differences in the results. This section gives an overview of parameters and the most important ones are briefly discussed

There are two main steps of data processing in my study: Source extraction and candidate selection. Source extraction is the process of extracting sources from the Y, J, and NB118 images and candidate selection is about selecting objects that fulfill a set of photometric criteria.

How data are processed can be seen in overview in figure 4.1. Data processing is primarily done in Python except for Source extraction, which is done using SExtractor.

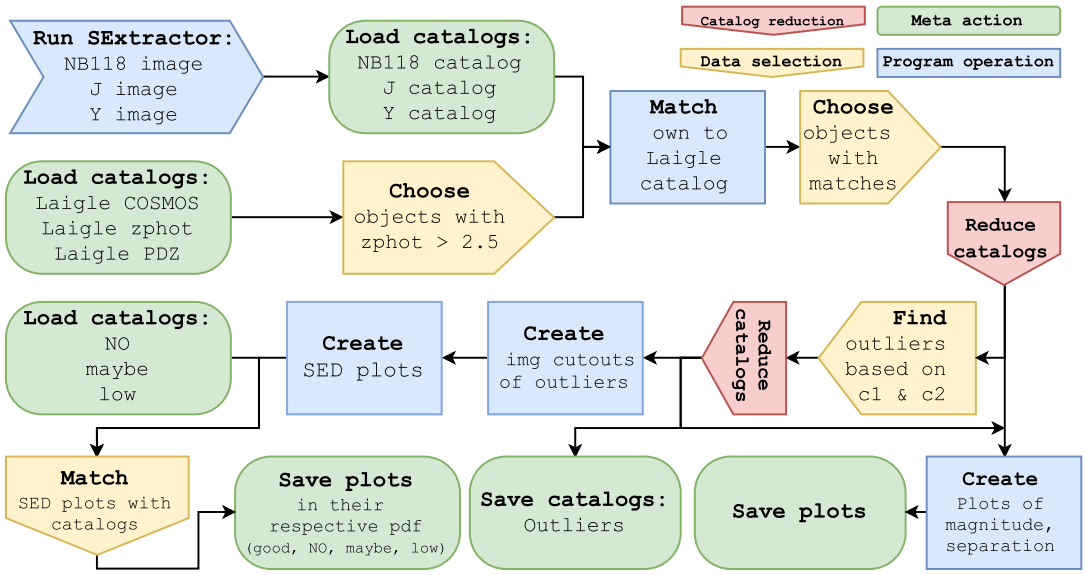

Figure 4.1: A flowchart on how data and catalogs are used and put together. It follows the data processing script hierarchically. The first program operation, **Run SExtractor**, is basically source extraction. The rest of the operations are done in Python. In **Find** outliers, c1 and c2 are equations 4.5 and 4.6. The catalogs used for matching SEDs are the manually selected objects that show either bad behavior (NO), strange behavior (maybe), or signs of OII emission (low).

4.1 Source extraction

An important aspect of this study is to extract the flux of objects in the new UltraVISTA images. This is done by using SExtractor in dual-image mode where the first image is the detection image and the second one is the extraction image. Additionally, several other options for object identification are considered such as- how many coherent pixels is an object required to have and how much brighter does an object have to be compared to the background.

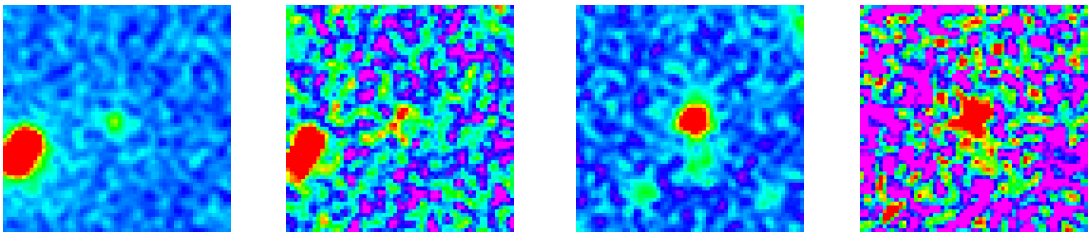

(a) Smooth J image (b) Clumpy NB image (c) Smooth J image (d) Noisy NB image

Figure 4.2: Cutouts of J095745.01+020532.7 ((a) and (b)) and J095930.43+015908.1 ((c) and (d)). These two sources show what to be wary of when using NB as detection image. The J image shows nice and smooth sources but the NB image reveals a clumpy and noisy source respectively.

4.1.1 Detection image

The detection image determines where detected sources are situated and thus from where aperture measurements are centered. Faint objects are especially sensitive to the position of apertures, and small changes in aperture position can decide whether or not an object fulfills the selection criteria. Additionally, objects are only extracted as long as they are in the detection image despite the fact that they may be very bright in other images. It is therefore important what image to use as detection image.

Obviously, there are three possible images to use as detection image; Y, J, and NB. Each image provides its own advantages and limitations. Generally, the Y and J images are not as noisy and cover a larger area of the sky. Sources in these images are well-defined and many of them are smooth whereas NB sources can exhibit clumpy and irregular shapes. These features are exaggerated in noisy areas of the image. An example of this can be seen in figure 4.2.

Given the premise of the study, which is to use NB118 to search for objects with color excess, it does make sense to use the NB image as detection image. If an object is not present in NB, it will not be picked out for further analysis. The method is not foolproof, however. Objects that are faint may not be picked up in the NB image since the background is generally more noisy. Thus, it may not be sufficiently bright than the background for SExtractor to notice it.

Comparing J versus NB118 as detection image, 299,000 versus 139,000 sources are found, respectively. Despite this, both procedures produce the same amount of selected candidates. While both methods are valid and can be used to supplement each other, only the objects found using the NB detection image will be used for further analysis.

4.1.2 Input parameters

The two primary parameters that are examined are `DETECT_THRESH` and `DETECT_MINAREA`. Additionally, several other parameters are useful and even necessary to adjust for good results. Among these are: (1) using a filter that essentially smooths the image to aid detection of faint objects, (2) the aperture size in which flux is measured, (3) and type of background analysis that is to be carried out.

`DETECT_THRESH` describes the threshold above which pixels are considered a part of an object. More specifically, it is how many times brighter a pixel has to be relative to the background root-mean-square (RMS). The default value in SExtractor is 2.5 but it is highly recommended to change it depending on one's objective. A threshold of 2.5 sigma is fairly high for faint objects and detection of these may benefit from a lower threshold.

A sigma of 2.0 and 1.5 is tested. On a 5700×5700 pixel subimage of the NB image, a value of 1.5 sigma gives 8453 total sources, 2.0 sigma gives 7037 total sources, and 2.5 sigma gives 6115 total sources. Some detections with 1.5 sigma may be image artifacts, but not all will fulfill the selection criteria and thus not be selected for further analysis. Even then, selected objects are studied qualitatively afterwards and thus they can be removed manually. Therefore, 1.5 is the value used for `DETECT_THRESH`. This parameter is examined further in chapter 5.

Another important parameter is `DETECT_MINAREA`. It is the minimum number of pixels above the detection threshold an area is required to contain in order to be considered an object. A small area may give false detections or even background detections while large areas may skip faint objects. On the same subimage as mentioned above, using 1.5 sigma for detection yields 8611 objects with 3 as minimum area, 8453 using 5, and finally 8318 using 7. The number of detections is thus not as affected by this parameter as it is with altering sigma. While the same argument used for selecting a low detection limit can be made for selecting a small minimum area, 5 is used as minimum area. The reasoning behind this is that not many objects are lost by changing this parameter, and obvious false detections caused by a small minimum area are manually rejected. The effects of changing these parameters is discussed in chapter 5

A few other parameters are also important. One of them is aperture size, `PHOT_APERTURES`. It is in units of pixels and since the resolution in the images are $0.15"/pixel$, a 2" aperture needs a setting of 13.33, 3" requires 20.00, and so on. Since this study is generally dealing with faint and high redshift objects, a large extent on the sky is not expected. Multiple apertures can be used if. Hence this option is set to 13.33, 20.00 for 2" and 3"aperture measurements.

Another aspect of extracting sources is to consider how background is decided. The parameter `BACKPHOTO_TYPE` can be set to either `GLOBAL` or `LOCAL`. When running SExtractor, it builds a global background map at first. This background map is then used for detections. Using `GLOBAL` means that the photometry is computed from this global background map, but with `LOCAL`, the background is recomputed in a rectangular annulus around the object. Seeing that the NB image has large systematic differences in background, e.g near strip edges, `LOCAL` is used. The number of detections are not different as this parameter only decides the background for photometric measurements. The change in the photometry of objects may have an effect on the number of selected outliers.

Lastly, a filter can be used to convolve the image which will aid in detection of faint extended objects. A Gaussian convolution kernel with FWHM close to the seeing from the images is used as filter as recommended by the manual[1] and Bertin and Arnouts (1996). The values for the seeing for Y, NB118, and J are 0.71", 0.75", and 0.73" respectively (Milvang-Jensen, priv. comm.). These values are given in pixel values and calculated by the conversion 1 pixel = 0.15".

4.1.3 Output parameters

Before the source extraction is executed, one has to decide what output is desired. Various photometric measurements can be extracted, including flux from an isophotal area (ISO), flexible elliptical aperture (KRON/AUTO), and circular aperture (APER). Additionally, the position of sources can be extracted as both pixel coordinates or world coordinates. One type of photometric measurements is more suitable for specific tasks than others, and some tasks become easier depending on the coordinate type being used.

The ISO flux is the flux measured within the detection isophote. This is only influenced the `DETECT_THRESH` keyword. In principle, this is good for determining the color of an

[1] `https://www.astromatic.net/pubsvn/software/sextractor/trunk/doc/sextractor.pdf`

object since it is unlikely to be contaminated by other sources. Non-gaussian objects or clumpy objects, though, are vulnerable to erroneous measurements. The AUTO flux is measured by a Kron-like aperture (described in Kron 1980), which is basically a flexible elliptical aperture. It is put to good use when measuring irregular or elliptical shaped objects and single objects in crowded areas. Its strength is also its weakness since the aperture is different from object to object and thus yields inconsistent measurements. The last type of measuring can be done with circular aperture. The size of the aperture is user-dependent, but common sizes are 2" and 3". All photometric measurements are extracted since each can be used for different purposes.

Both pixel coordinates and world coordinates are extracted. The pixel coordinates are used for finding an object's corresponding entry in the Laigle catalog since the conversion from pixels to arc seconds is straightforward. World coordinates are primarily used for naming and identification purposes (IUA style). Both decimal degrees and sexagesimal formats are used. Sexagesimal coordinates are not directly given from SExtractor but calculated using the `astropy` python package.

4.2 Candidate selection

As briefly mentioned earlier, objects are selected from two main criteria: color excess and high photometric redshift. However, this is one of the very last steps of source selection. These steps will be described in this section. Most steps will be treated qualitatively, but quantitative analysis of certain steps are included as well and presented in chapter 5.

4.2.1 Redshift sorting

The redshift sorting is done using the photometric redshifts from the Laigle et al. (submitted) catalog (section 3.3) and is the first sorting processes performed. Several different redshifts are given in the catalog: z_{min}, redshift of the lowest χ^2 template, z_{PDF}, median redshift of the PDZ, z_2 is only supplied if a second redshift solution exist with a probability of $>5\%$ inferred in the PDZ, and z_q, the redshift using an AGN library for SED fitting. For an explanation of PDZ, see section 3.3.2.

Typically, $z_{min} = z_{PDF}$ but Laigle et al. (submitted) and Ilbert et al. (2013) has found that z_{PDF} is a slightly better redshift estimator of the two. A last redshift is given, z_{best} which is equal to z_{PDF} unless an object is detected in x-ray or a stellar template yields a better χ^2. In these cases, z_{best} is equal to 9.99 and 0, respectively. z_{best} is used for selection in this study.

Once the photometric redshift has been extracted from the catalog, it is required that:

$$2.5 < z_{best} < 9.0 \tag{4.1}$$

where 2.5 is chosen as the minimum allowed redshift in order to avoid [OII] emitters in the sample and 9.0 is to avoid x-ray emitters. Another requirement worth discussing is whether or not objects with $z_{best} > 2.5$ but a lower bound 68% CFI lower than 2.5 are selected or not. It is not done and thus equation 4.1 is the only requirement for redshift selection. Objects may also be rejected if $z_2 < 2.5$, but this is not done either for this study.

4.2.2 Object matching

A simple algorithm to match Laigle catalogs objects to the objects found in this study is implemented. Since the position of objects has been supplied in both catalogs, these are used for object matching. It is not expected that objects in both catalogs are situated

in the exact same position since different detection images has been used. Laigle uses a chi-squared YKHK$_s$-z^{++} for detection whereas this study only uses NB118.

The way matching works is to first translate the coordinates of objects in the Laigle catalog to NB118 image pixel coordinates. The reasoning behind this is that pixel positions are slightly easier to work with and understand intuitively than world coordinates. The pixel coordinates of the objects found in NB118 are already available from the source extraction procedure. Pixel coordinates do not have to be integers.

For each object extracted, it is first checked whether or not objects share x-pixel coordinate with redshift-sorted objects from the Laigle catalog. However, since it is not expected that the same object shares the exact same coordinates, a slight offset, ε is allowed. If equation 4.2 is fulfilled, the next step is to check whether or not the two objects also share y-pixel using the same offset condition as before. If equation 4.3 also is fulfilled, a match is found.

$$|x_{own} - x_{Laigle}| < \varepsilon, \tag{4.2}$$

$$|y_{own} - y_{Laigle}| < \varepsilon, \tag{4.3}$$

where x_{own} and y_{own} are the pixel coordinates of my object and x_{Laigle} and y_{Laigle} are the pixel coordinates of the objects in the Laigle catalog. The algorithm then writes the index of the two objects down, e.g index 123123 for the object in the Laigle catalog and 4545 for the object in my catalog. Once all of my objects has been tested, both catalogs are reduced to contain only matching objects and they are both sorted to match each others indices - i.e index 10 in both catalogs is the same object.

The value of ε needs to be low enough to make sure that matches are indeed matches of the same objects but high to take the possible strange appearances of NB118 objects into account. A value of 2 is used for matching in this study. This means that the maximum separation allowed is 2.83 pixels (= 0.42"). The reason for choosing 2 comes partly from simple trial and error and partly from the typical maximum offset (see figure 4.3).

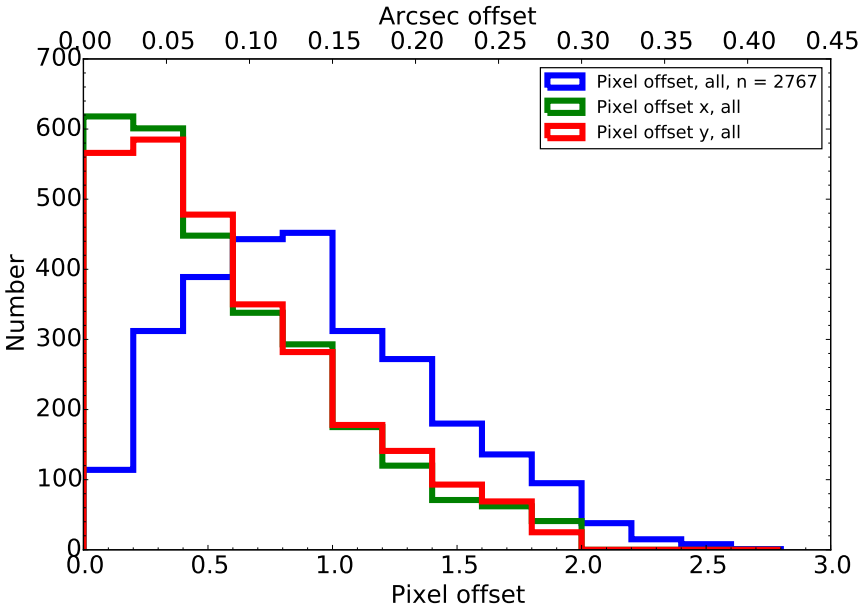

Figure 4.3: Separation between all matched objects in Laigle catalog and in own catalog. The green and red histograms show $|\Delta x| = |x_{own} - x_{Laigle}|$ and $|\Delta y| = |y_{own} - y_{Laigle}|$, respectively. The blue histogram is the total separation sep $= \sqrt{(\Delta x)^2 + (\Delta y)^2}$ which has $\langle \text{sep} \rangle = 0.92 \pm 0.49$ pixel $= 0.14 \pm 0.07$". A natural cut-off is visible towards 2 pixel separation in x- and y-pixel coordinates.

Using $\varepsilon = 2.0$ yields 2767 matched objects with a mean separation of 0.92±0.49 pixels ($= 0.14 \pm 0.07$"). While a larger ε will yield more matches, it can be seen from figure 4.3 that there is a natural cutoff at around 2.0-2.5 pixel separation, though the x- and y-separations seem to want to extend slightly further than 2.0. Also, allowing a larger separation may match objects incorrectly and thus increase the offset. It is not a goal in itself to decrease the offset between matched objects, but a small offset is indicative of correct matching.

4.2.3 Object selection

Next comes the process of selecting objects that fulfill the narrow band excess criteria. Identifying an excess relies on two conditions: The narrow band magnitude is a certain amount brighter than the continuum estimated from a liner interpolation between theY and J magnitudes, and that this excess is significant, i.e the relative error on the measurement is not too high. This is done using 2" aperture measurements, although iso magnitudes are also included for comparative purposes.

The narrow band is situated inside the J band. A naive way of measuring narrow-band excess would be to compare the magnitude in the NB with that in J.. This will cause some problems, though. Looking at how the bands are situated gives some insight. It can be seen from figure 2.4 which shows that NB is inside J but not in the center. The NB is close to the low wavelength limit of the J filter. If an object has a sloped continuum across J, NB-J will yield a non-zero result. For example, if the continuum rises towards higher wavelengths in J, the NB magnitude is fainter than the J magnitude.

One way to determine whether or not the continuum is sloped is to look at the slope, or gradient, from Y to J. If Y and J are approximately the same, a somewhat flat continuum can be assumed. The larger the gradient, the steeper the underlying continuum is assumed to be. If Y is brighter than J, NB is situated in the bright wing of the J-band even though it is not necessarily located on top of an emission line. These observations point towards having a corrected J-NB color in order to determine whether or not NB has excess.

This procedure is the same as in Milvang-Jensen et al. (2013), section 5, equation (7). Here, the quantity $(J - NB118)_{corr}$ is introduced which depends on the slope of the $(Y - J)$ color:

$$(J - NB118)_{corr} = \begin{cases} (J - NB118) + 0.34(Y - J) & \text{if } (Y - J) \leq 0.45 \\ (J - NB118) + 0.158 & \text{if } (Y - J) > 0.45 \\ (J - NB118) + 0.07 & \text{if } Y\text{not detected.} \end{cases} \tag{4.4}$$

The first branch corresponds to the empirical relation for the Milvang-Jensen et al. (2013) found to correct for the continuum slope. The second branch is a modification that was introduced due to passive galaxies near $z = 2$ being incorrectly identified as having narrow band excess (Milvang-Jensen et al. (2013), figure 7).

Next is determining how large the minimum excess needs to be. A low cut yields more objects, but some of them may not have significant excess and the NB magnitude may even be the same as the continuum. Having too many objects will also be difficult to describe properly given the scope and time frame of this work. A high cut gives a smaller sample size and will aid in only picking strong candidates. This cut will reject objects with weak excesses, but the selected objects are more likely to show exhibit features. A high cut ensures that only definite strange objects are selected. Therefore, it is required that:

$$(J - NB118)_{corr} \geq 0.3 \tag{4.5}$$

This is the first condition - sometimes referred to as c1 within this thesis. It is possible to choose 0.2 such as Milvang-Jensen et al. (2013), but it yields too many candidates.

Additionally, the excess is required to be significant. Again, lower significance means more objects. However, only robust detections are desired. A high σ significance is therefore desirable. Milvang-Jensen et al. (2013) used a value of 2.5σ. It is required that:

$$(J - NB118)_{corr} > 3\sigma_{(J-NB118)_{corr}} \tag{4.6}$$

This is the second condition - sometimes referred to as c2 within this thesis. The effects of changing c1 and c2 will be discussed further in chapter 5. From this point on, selected candidates are sometimes referred to as outliers.

5 | Results and Discussion

The results of this thesis cover several aspects of the study, though it is first and foremost identification of NB excess objects. A further discussion of parameter choices and computations performed in the data processing is also be included.

One of the most important products from the data processing is the spectral energy distributions (SED) of objects selected as outliers. A schematic of the SED products can be seen in figure 5.1. The SEDs of the candidates selected for in depth analysis is included in appendix A while the rest are available on a webserver[1]

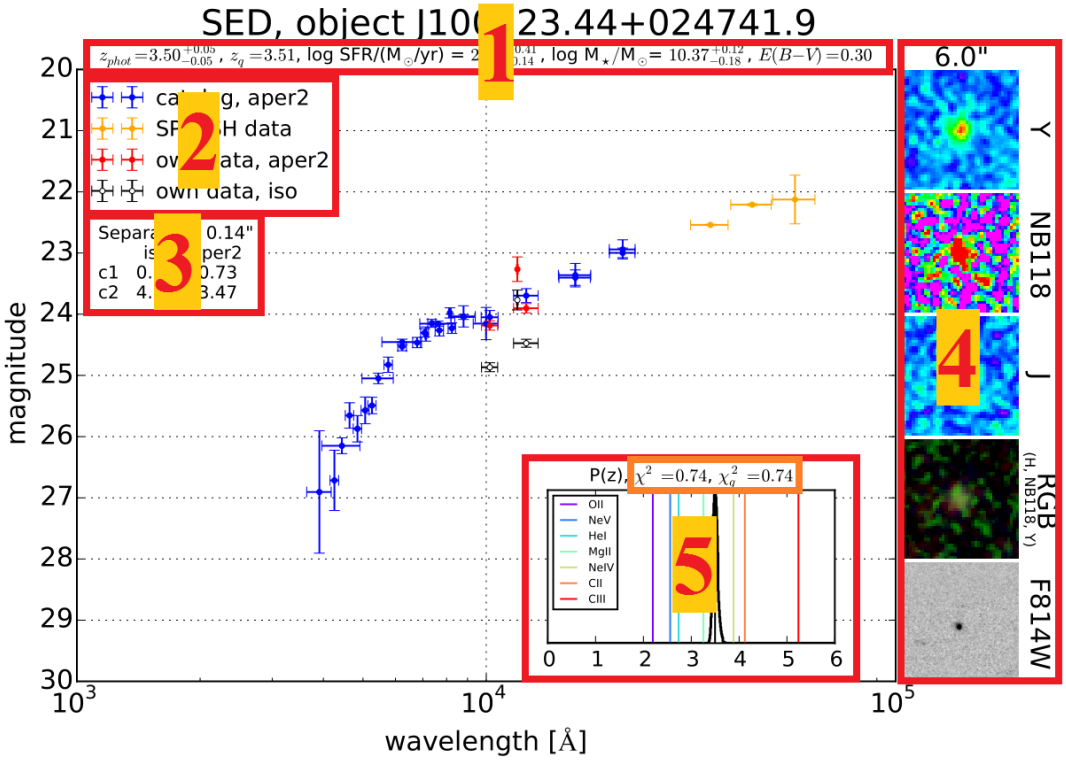

Figure 5.1: Schematic of the SED. The SED plots contain lots of information and an overview is given here. [1] is the SED derived properties and contains: z_{phot}, the best photometric redshift, z_q, the best redshift with AGN templates, SFR, stellar mass, and extinction. [2] is the legend which shows what data is plotted. [3] shows the seperation of the object from the Laigle et al. (submitted) catalog and the values of the selection criteria c1 and c2 (see equation 4.5 and 4.6) with two different types of photometric measuring. [4] shows 6" $\times$ 6" arcsec cutouts of the object in different images. A cross appears if the object is not covered in F814W [5] shows the PDZ and outlined in orange are the reduced χ^2 for the template fittings without and with AGN templates. The colored lines in the PDZ are the emission lines mentioned in table 2.2. The blue data points are systematic offset corrected 2" measurements from Laigle et al. (submitted) and the orange are also from the catalog but SPLASH data. The PSF for SPLASH is so large that it does not make sense to talk about 2" so the total magnitude is used. The magnitude is AB magnitude.

[1] Good SEDs: `https://www.dropbox.com/s/yonff78tssp54bt/SED.pdf?dl=0`
Bad SEDs: `https://www.dropbox.com/s/mhlyr3b9ct4qnt8/SED_NO.pdf?dl=0`
Maybe SEDs: `https://www.dropbox.com/s/617mhy2bamrtmq0/SED_maybe.pdf?dl=0`
Low SEDs: `https://www.dropbox.com/s/pmvgvketaw7vjgt/SED_low.pdf?dl=0`

5.1 Selected candidates

This section covers all the candidates that fulfilled c1 and c2. A coarse sorting (referred to as labeling) is applied and a subsample is picked for further analysis. Figure 5.2 shows the selected candidates and subsequent coarse sorting on a (J-NB) versus (Y-J) color diagram and figure 5.3 shows the outliers on a $(J - NB118)_{corr}$ versus $\mathrm{NB118}_{aper2}$ color diagram.

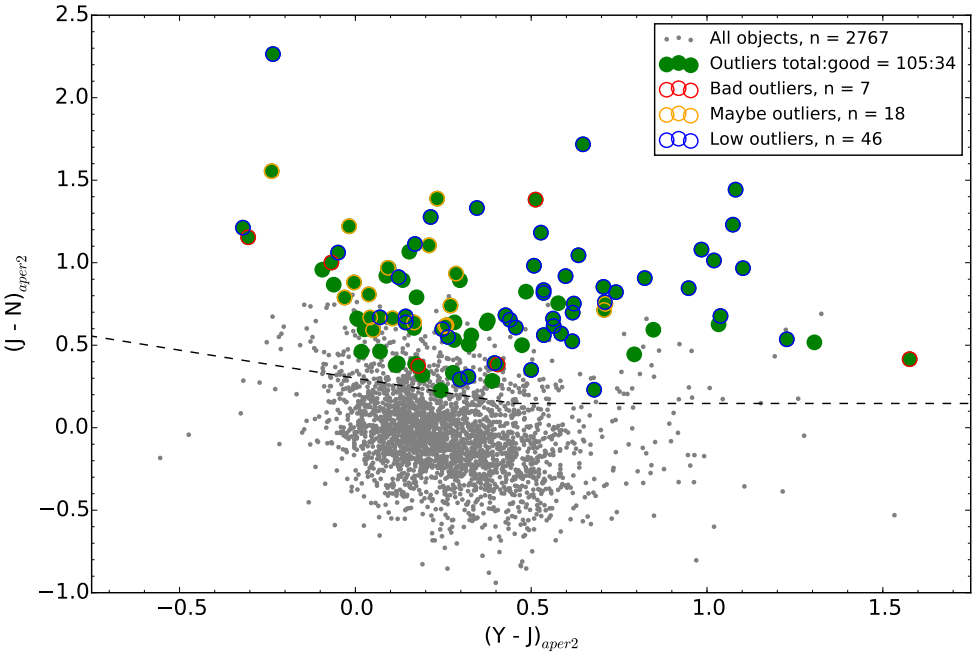

Figure 5.2: Selected candidates in a (J-NB118) versus (Y-J) color diagram. Note that the candidates have been labeled in accordance with section 5.1.1. Candidates mean the same as outliers. The dotted line is the selection criteria c1. The Total outliers are green (105), and the ones with no labeling have no colored circumference are the good outliers (34).

5.1.1 Labeling

The final number of outliers is 105. It is a large sample to study in detail so some sort of sorting is required. While the redshift cut is set so that [OII] emitters are not included, many outliers still show signs of such emission. Obviously, these are not of significant interest for the thesis and are not considered good outliers. Other outliers are situated at the edge of a NB strip, in star halos, or results of faults in the detector. Clearly, these outliers are simply rejected. Lastly, some outliers exhibit strange morphology, are located in areas that may be considered bad regions but not to such a degree as to reject them, or generally prove to be difficult and time consuming to analyze and approve. These are labeled 'maybe' since they may actually be fine outliers. The outliers that are not labeled in any way are considered good outliers.

The label of an outlier can be determined by visual inspection. 6" × 6" cutouts of each objects has been made from Y, J, and NB118 images. Objects on the edge of the NB strips are immediately found, and Y and J images can be used to reveal if an outlier is located near a star as the background appears fog-like and brighter than usual. Sometimes the cutout is too small to reveal this and inspection of the full image is required. Some outliers may very well be results of detector defects and might be cross-talk rather than

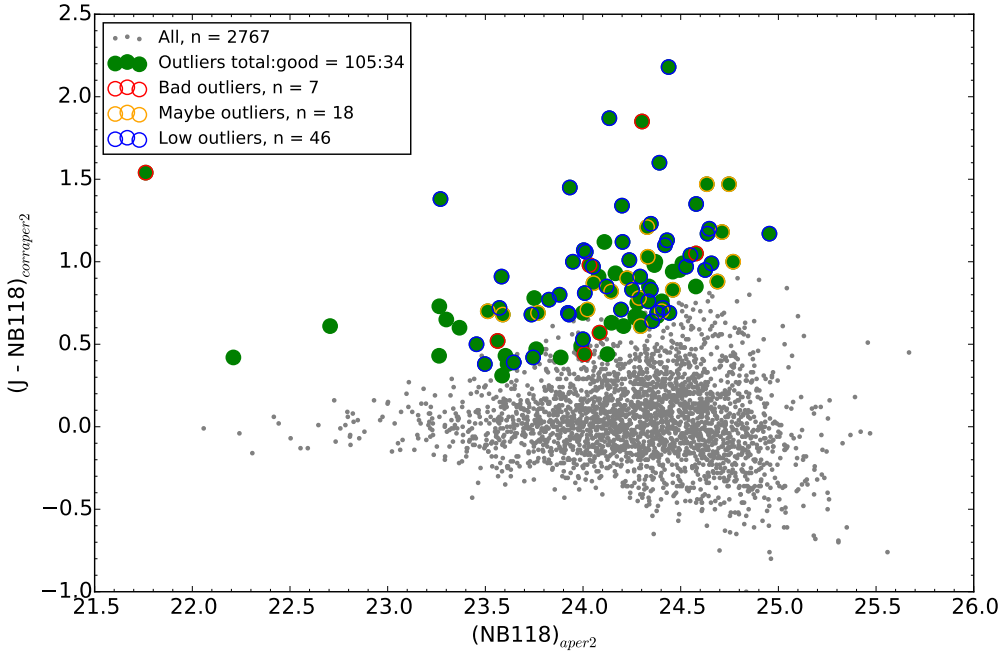

Figure 5.3: Selected candidates in a (J-NB118)$_{corr,aper2}$ versus (NB118)$_{aper2}$ color diagram. Note that the candidates have been labeled in accordance with section 5.1.1. Candidates mean the same as outliers. The dotted line is the selection criteria c1. The Total outliers are green (105), and the ones with no labeling have no colored circumference are the good outliers (34).

a real object (see section 3.2.2). While an object may not show any immediate problems from the cutouts, all objects have been inspected in all images to look for signs of any problems. Further visual inspection can be carried out for select objects that are covered by the HST Advanced Camera for Surveys (ACS) instrument using the F814W (I-band) filter, which has greater resolution (0.03"/pixel) than VIRCAM(0.15"/pixel).

An additional method to further label outliers is to make a qualitative analysis of the SED, photometric redshift, and PDZ combined. For example, if a high redshift object has a large break towards UV, it may very well be a Lyman break, while an object with nearly flat SED and its PDZ peaks near 2.20, it may very well be an [OII] emitter. The Lyman break galaxy will be kept as a good outlier whereas the [OII] emitter will be labeled 'low'. Labeling is thus a very coarse sorting. Labeled outliers are still kept but will not receive detailed analysis. Brief descriptions and characterizations of the different labels are

Label	N	$\langle z \rangle$	σ_z	$\langle \log M_\star \rangle$	$\langle \log \mathrm{SFR} \rangle$	$\langle sSFR \rangle\ [Gyr^{-1}]$
Bad	7	3.85	1.15	10.03	1.51	4.35
Maybe	18	3.36	0.45	9.68	1.31	6.56
Low	46	2.65	0.14	9.57	1.02	3.93
Good	34	3.35	0.56	10.08	1.62	5.12
All	105	3.08	0.62	9.79	1.30	4.79

Table 5.1: Table showing the distribution of labels. The most used label is 'low'. As discussed in section 5.1.1.3, the NB118 excess is believed to be caused by [OII], though other emission lines are also possible explanations. If it is [OII], however, the reshift of these objects are wrong by $\sim 20\%$ on average.

provided, though.

Table 5.1 shows the mean photometric redshift of the different labels. It shows that 'maybe' outliers and the good candidates are similar in this regard while 'low' labeled outliers are centered at $z = 2.65$ with only a small spread, $\sigma_{'low'} = 0.14$.

5.1.1.1 Bad outliers

These outliers are near the edges of narrow band strips, in star jets or star halos, or are simply defects from the detector. Examples of this can be seen in figure 5.4. While it is obvious that 5.4a (edge) and 5.4b (jet) are given the label 'bad', it is not so obvious with 5.4c (possible cross-talk) and 5.4d (star halo).

Star halos influences the background significantly. The flux from the star is most certainly contributing to the flux of the outlier. This means that the measurements on the object are wrong. No analysis to determine to what degree measurements are affected has been carried out, but it is most likely different from filter to filter. However, it is entirely possible that Y, J, and NB118 are affected somewhat equally and the offset cancels out. Therefore, the criteria for selection is still valid and the object may still be considered an object with NB118-excess. However, for the sake of only keeping robust outliers, these objects will not be considered for further analysis.

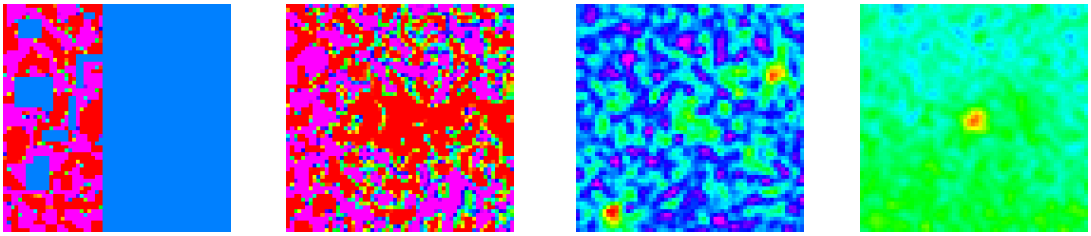

(a) NB edge (b) Star jet (c) Cross-talk (d) Star halo

Figure 5.4: Examples of bad objects. (a) shows an object near the edge of the narrow band strip, (b) shows an object which is actually a jet from a star, (c) may very well be cross-talk, and finally (d) shows an object that certainly is real and looks fine in NB, but the J cutout reveals that it is close to a foreground star. These objects all have the label 'bad'.

5.1.1.2 Maybe outliers

Some outliers are close to foreground galaxies or stars and might be affected by them, or some outliers are faint and almost indiscernible from background. However, the faults they carry are not grievous enough to label them 'bad' and is thus labeled 'maybe'. Determining the severity of the faults is done on a subjective and case to case basis and with the same method for 'bad' outliers. Few objects from the 'bad' category may thus be considered 'maybe' objects on vice versa. Examples of this label can be seen en figure 5.5.

This raises the question of whether or not these labels are misleading and unscientific. It is important to remember, however, that the labels are only meant for coarse sorting. Further analysis on labeled outliers can still be carried out. It is, however, not done in this thesis.

They can roughly be divided in three redshift intervals: $\Delta z = 2.5 - 3.0, \Delta z = 3.0 - 3.5, \Delta z = 3.5 - 4.0$. As will be discussed later, the first interval may correspond to [OII] emission, the second to MgII emission and the last interval may also be MgII emission but it is not certain.

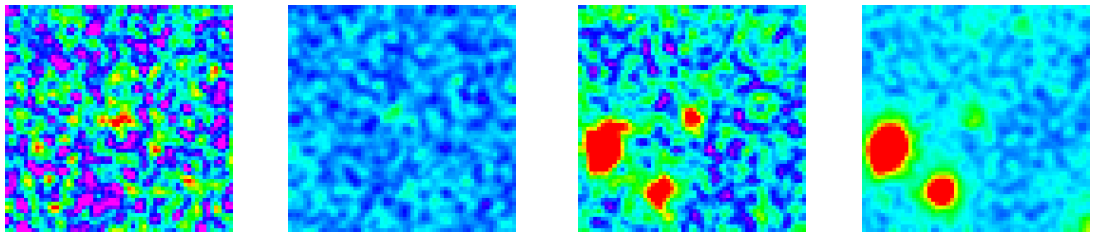

(a) NB faint (b) J faint (c) NB crowded (d) J crowded

Figure 5.5: Examples of maybe objects. (a) and (b) are of the same object. While it is clear that there is an object in the NB image, it is almost indiscernible in J. (c) and (d) are also of the same object. Here, it is also clear in NB that there is an object, but it is located next to two galaxies to the lower left and in a star halo. It is, however, clear that this object has a strong NB excess despite the background.

5.1.1.3 Low outliers

Lastly, a label is applied to galaxies that show signs of O II emission in NB118 (as discussed below) and thus have a redshift of 2.2 or a break between Y and J coupled with a low redshift ($\lesssim 2.8$) which indicates that the 4000-Å break is present between or in the Y and J bands. Many outliers exhibit a photometric redshift just above the cut (i.e $z = 2.54$). In fact, this is the most common label with almost twice as many objects as the two other labels combined and only 5 objects short of the number of good outliers.

O II emitters are identifiable by the lack of features towards lower wavelengths from NB118 except a steady drop in brightness towards lower wavelengths. Also, the PDZ generally tends towards lower photometric redshifts. There is some indication of a break between Y and J, but it is not significant, i.e they are the same within their errors.

The other type of objects in this label is similar to O II emitters in some regards. The large break between Y and J can partially be explained by a 4000-Å that extends far into lower wavelengths ($\sim$ 3200Å), which is not uncommon for old galaxies or dusty star-forming ones, see figure 5.6 (Kriek et al. (2011)). This does not explain the NB excess, though. It is expected that J will be fainter towards lower wavelengths. NB118 is located in the low-wavelength part of J and is thus expected to be fainter - NOT brighter as is required for an excess.

A prime suspect for this is O II, in which case these types are similar to the previously described O II emitters. The only difference between the two types are then the type of galaxy. A small 4000-Å break is found in star-forming galaxies while increasingly significant breaks are found in dustier and older galaxies. This also means that the photometric redshift is systematically wrong for these outliers since they range from $\lesssim 2.6 - 2.9$ when the correct redshift would be 2.2.

It is possible that this error arises from the fact that the 4000-Å break is located at 12800Å at redshift 2.2. This places it in the middle of the J band. However, the strength of the break varies greatly with type of galaxy. This, coupled with the fact that Y and J do not overlap (see figure 2.4) a range that covers the tail of the break for galaxies near this redshift means that correctly identifying the strength of the break is difficult. Having a broad band filter here could aid in correctly identifying the strength of the 4000-Å break and thus redshift of galaxies near a redshift of 2.2.

It should be noted that [NeV] and HeI are candidate emission lines at these redshifts (2.5 and 2.8 respectively). They are, however, not as common as [OII] and the high ionization potential of [NeV] required a hard ionizing spectrum which is unlikely to arise from star formation (Vignali et al. (2014), and references therein) but can from AGNs. Furthermore, the PDZ of the galaxies with this label tend to extend to a redshift of 2.2. In order to have

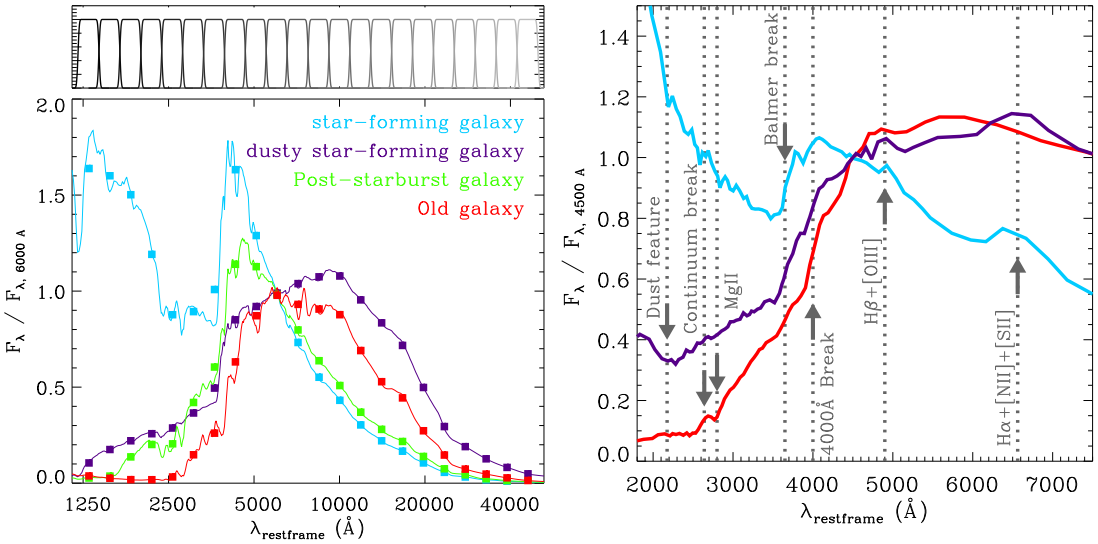

Figure 5.6: From Kriek et al. (2011). To the left is 22 synthetic rest-frame filters on top and below is four different galaxy types. This figure is meant to show the overall shapes of different galaxies. To the left is the same galaxy types but zoomed in on the wavelength interval between 2000Å and 7500Å. Here, many spectral features are visible such as the Balmer- and 4000-Å break and the flat SED towards lower wavelengths for old galaxies and dusty-star forming ones. Star-forming galaxies see a rise in flux at low wavelengths.

a robust sample of good outliers, galaxies whose PDZ includes [OII] are labeled as 'low', i.e suspected [OII] emitters

Also worth noticing is that if these labeled galaxies are indeed [OII] emitters, a photometric redshift above 2.68 means that their photometric redshifts are catastrophic failures in as defined in Laigle et al. (submitted).

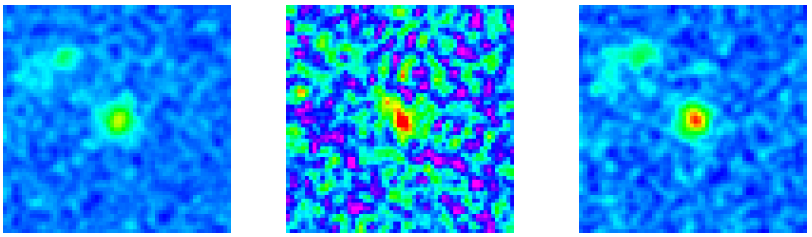

(a) Y cutout (b) NB118 cutout (c) J cutout

Figure 5.7: Examples of a low object. The cutouts are all of the same object, J100215.97+021356.0. Here, it can be seen that the object is very bright in NB118 and J but weaker in Y. This is indicative of a break between the two broad bands. The photometric redshift of the object is 2.73 with 68% confidence interval of [2.64, 2.83] places the 4000Å-break at between ∼14500Å - 15500Å.

5.1.2 Effects of changing parameters

It has been inferred from chapter 4 that changing the parameters for source extraction and candidate selection can influence the final results to a large degree. The source extraction parameters are important for photometric measurements such as magnitude and error while object selection parameters are important for the robustness of selected outliers.

The detection parameters strongly influence the total number of objects and stricter thresholds especially cause faint objects to be ignored whereas choice of background can

decide whether objects fulfill the selection criteria or not. The two detection parameters that are examined are `DETECT_THRESH` (= σ) and `DETECT_MINAREA` (= Min area).

From table 5.2, it can be seen that changing the detection threshold has a large effect on the number of good outliers. The total number of objects is roughly the same (within 25%), but the number of matched objects is much different. Going from 1.5σ to 2.0σ reduces the number of matched objects by more than 50%. Roughly the same percentage of the matched objects are outliers (3.23% and 3.06%) and the same percentage of those are good outliers (41.98% and 43.34%) The same story repeats itself when looking at 2.5σ. First, the total number of objects is roughly the same as with 2.0σ, but the number of matched objects is is 46.07% smaller. The following reductions are of similar size: 3.83% of matched objects are outliers and 36.00% of those are good.

Min area: 5	σ			σ: 1.5	Min area		
	1.5	2.0	2.5		3	5	7
Total	138,530	113,460	97,040		140,940	138,530	136,240
z > 2.5 matched	2371	1174	626		2521	2371	2247
Outliers	75	36	22		79	75	74
Good outliers	**32**	**14**	**8**		**35**	**32**	**32**
Highest redshift	5.42	4.42	4.42		5.42	5.42	5.42
Median redshift	3.25	3.09	3.01		3.28	3.25	3.25
Mean redshift	3.40	3.21	3.19		3.38	3.40	3.40

Table 5.2: Table showing the effects of changing the input parameters. The left columns have altering σ(=`DETECT_THRESH`) for a minimum pixel area of 5 and the right columns have altering minimum areas for $\sigma = 5$. It is interesting to note that changing the minimum area parameter does not affect the results much whereas changing σ does. Obviously, a larger step size in minumum area or smaller step size for σ can lead to changes of similar size. These numbers stress that a low σ is important and a reasonable minimum area makes selecting outliers easier. **DISCLAIMER:** These numbers are not correct for the newest catalog received a week before submission deadline.

These numbers support the notion that high redshift objects are especially vulnerable to the detection threshold. It is likely to be faint objects that are not included by using a 2.0σ threshold or higher. An example of an object that has not been detected using 2.0σ as threshold is J100023.18+020246.7. A further discussion of this object is found in section 5.2.1.14 but the point is that it is a real object although it is very faint and diffuse.

Another parameter that has been mentioned is `BACKPHOTO_TYPE` - i.e whether to use a global background map or recompute a local one. Using a local background yields the aforementioned 105 selected candidates with $\langle z \rangle = 3.08 \pm 0.62$ while a global background map gives 95 outliers with $\langle z \rangle = 3.06 \pm 0.62$. The main difference thus the number of outliers albeit a small difference. An explanation for the difference may be that in the non-uniform background of NB118 images, a local background map better highlights objects hidden in the noise.

Changing c1 and c2 also affects the number of outliers. Table 5.3 shows what happens when varying c1 between 0.1 and 1.2 in increments of 0.1 and c2 between 2.0 and 4.0 in increments of 0.5. Changing c2 shows a gradual decline in outliers with increasing value while c1 show a slow decline to begin with but a rapid drop at between 0.4-0.7 depending on c2.

Another thing to consider is what type of outliers are picked by changing c1 and c2. One way to quantize this is to look at the average redshift and the standard deviation of it. Using $c1 = 0.1$ and altering c2 yields:
$\langle z \rangle \simeq 3.14 \pm 0.55$ for $c2 = 2.0$, $\langle z \rangle \simeq 3.13 \pm 0.61$ for $c2 = 2.5$,

		Condition 1											
		0.10	0.20	0.30	0.40	0.50	0.60	0.70	0.80	0.90	1.00	1.10	1.20
Condition 2	2.0	271	265	252	220	168	131	85	60	44	28	21	13
	2.5	168	165	160	152	127	113	83	58	44	28	21	13
	3.0	106	105	105	101	92	87	68	55	44	28	21	13
	3.5	70	69	69	67	64	60	54	47	39	26	20	13
	4.0	45	45	45	44	41	38	35	31	27	20	16	12

Table 5.3: Number of selected candidates dependent on c1 and c2. A visual representation can be seen in figure 5.8.

$\langle z \rangle \simeq 3.08 \pm 0.62$ for $c2 = 3.0$, $\langle z \rangle \simeq 3.00 \pm 0.62$ for $c2 = 3.5$, and
$\langle z \rangle \simeq 2.96 \pm 0.59$ for $c2 = 4.0$.
Using $c2 = 2.0$ and altering c1 roughly yields:
$\langle z \rangle \simeq 3.14 \pm 0.60$ for $c1 \in [0.1 : 0.5]$, $\langle z \rangle \simeq 3.16 \pm 0.67$ for $c1 = 0.6$,
$\langle z \rangle \simeq 3.11 \pm 0.67$ for $c1 = 0.7$, $\langle z \rangle \simeq 3.05 \pm 0.68$ for $c1 \in [0.8 : 1.0]$, and
$\langle z \rangle \simeq 2.98 \pm 0.58$ for $c1 \in [1.1 : 1.2]$
The trend is that stricter conditions gradually lower the mean redshift of the selected outliers while the standard deviation roughly remains the same. Condition 1, though, has a large interval between 0.1-0.5 where little occurs. At $c1 \geq 0.6$, the mean redshift becomes lower while retaining a large standard deviation. This may just be indicative of the lower sample size. At $c1 \geq 1.1$, the mean redshift dips below 3.00 suggesting many high redshift outliers are rejected. Condition 2 gradually reduces the mean redshift and standard deviation indicating fewer and fewer high redshift outliers with increasing c2.

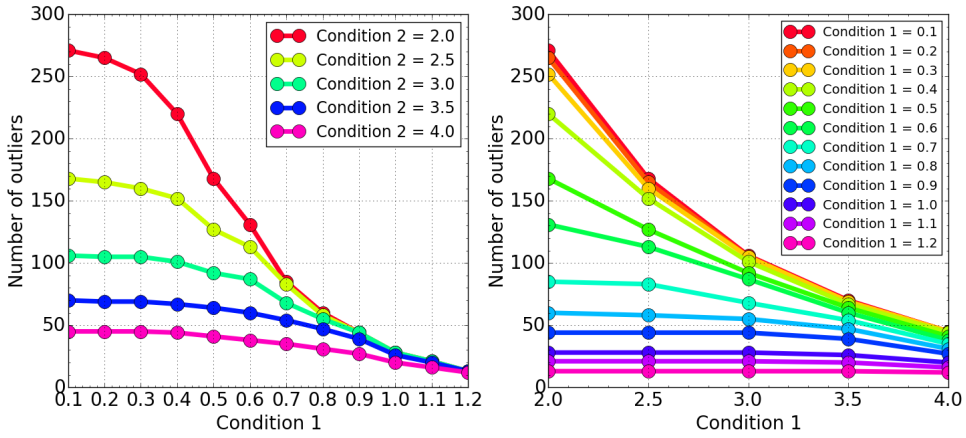

Figure 5.8: Visual representation of c1 and c2 changes. Table values can be found in table 5.3

5.2 Good outliers

Outliers that have not been labeled are considered good outliers. These outliers will be treated on a case to case basis but also put into different categories. Exact descriptions are difficult since SEDs are only so detailed. Though the photometric redshifts are of good quality, they are not always accurate enough for emission line identification in the NB118 filter. In several cases, it is ambiguous which emission line NB118 covers, and without additional identifiers such as color excess in other narrow-bands or intermediate-bands, proper identification proves difficult.

Despite these difficulties, attempts are made to accurately describe and categorize the good outliers. The SEDs are used for identification of spectral lines and type of galaxy while visual inspection of the objects provide information of the morphologies of the outliers. However, the Y, J and NB118 images have only have a pixelsize of 0.15". Cutouts from the F814W (I-band)[2] is used since its pixelsize is 0.03" per pixel providing better resolution information about the morphology of the outliers. A table containing all the good candidates with quick descriptions can be seen in table 5.4.

Laigle et al. (submitted) make a comparison between the spectroscopic redshift and photometric redshift and find a 1σ error on the photometric redshift of roughly 0.1-0.4 depending on i^+ magnitude (the fainter $i^+ > 20$ the larger) and redshift. A galaxy with $z = 3.50$ places NB118 no where near any strong emission lines. MgII is at redshift 3.26 where $\Delta z = 0.24$ - well inside the 1σ photometric redshift error. On the other hand, the photometric redshift may be very precisely determined with a 68% confidence interval of only ± 0.05. Hence, the precision may not allow any strong emission lines in NB118 but the low accuracy can.

Another explanation can simply be that the photometric redshift is correct and that there is an emission line that is not considered. It may be an emission line that is very unusual and only covered by little literature. The possible explanations are then way too numerable to discuss without spectra.

5.2.1 Description of each candidate

Here, a description is provided for each good candidate. Following is an attempt at categorizing them. Photometric redshift, SFR, and stellar mass can be found in table 5.4 if not mentioned. Additionally, plots of the SEDs along with image cutouts, PDZ, and derived properties can be found in appendix A or on a webserver as mentioned in the beginning of the chapter. Also, mentions of redshift refers to the photometric redshifts.

5.2.1.1 J095753.08+013754.7

Its low redshift (2.68) would have given it the 'low' label but unusual intermediate band photometry make it interesting. However, upon visual inspection of these bands (IA464, IA484, IA505, IA527, and IA427 to some degree) reveal that they are artifacts from a nearby star. The effect on the bands can be seen in figure 5.9.

It is still included in the total good candidate sample due to labeling being done before Subaru inspection. It is consequently not used due to its unusual SED but rather its implications on candidate selection; intermediate band photometry (or more specifically Subaru imaging) is not to be used uncritically.

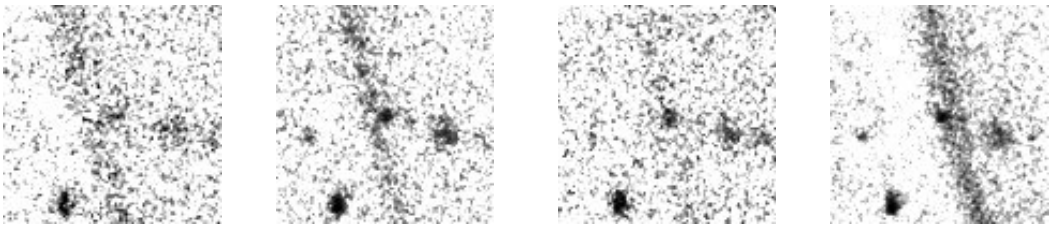

(a) IA464 (b) IA484 (c) IA505 (d) IA527

Figure 5.9: J095753.08+013754.7 Subaru artifacts

[2]from `http://irsa.ipac.caltech.edu/data/COSMOS/index_cutouts.html`

No.	Name	Redshift	log SFR	log $M_\star$	NB118 estimate	Further identifiers	Additional comments	Cat.
1.	J095753.08+013754.7	$2.68^{+0.22}_{-0.14}$	$0.56^{+0.36}_{-0.11}$	$9.61^{+0.09}_{-0.13}$	[OII]	None	Artifacts in Subaru	3
2.	J100009.82+014227.2	$3.55^{+0.08}_{-0.06}$	$1.45^{+0.12}_{-0.09}$	$9.80^{+0.07}_{-0.09}$	MgII	IA527abs	IA527 Lyα	2
3.	J095914.48+014306.8	$2.76^{+0.11}_{-0.20}$	$1.93^{+0.14}_{-0.26}$	$11.02^{+0.06}_{-0.08}$	[OII]	Y-J break	Low SFR	3
4.	J095924.96+014513.2	$3.14^{+0.01}_{-0.01}$	$2.19^{+0.08}_{-0.07}$	$9.94^{+0.06}_{-0.06}$	MgII	Yes, many	Likely QSO	1
5.	J095919.74+015213.2	$3.63^{+0.10}_{-0.10}$	$1.55^{+0.11}_{-0.29}$	$9.72^{+0.15}_{-0.11}$	MgII	NB711ems[1]	NB771:C IV?	2
6.	J100034.41+015640.1	$5.44^{+0.07}_{-0.08}$	$1.67^{+0.10}_{-0.11}$	$9.78^{+0.12}_{-0.13}$	CIII]	Ly-break	Highest redshift	2
7.	J095846.84+015802.7	$3.08^{+0.05}_{-0.04}$	$1.94^{+0.47}_{-0.11}$	$10.20^{+0.09}_{-0.18}$	MgII	IA427ems[1], point[2]	AGN? lack lines	1
8.	J100018.16+015822.6	$3.42^{+0.76}_{-0.16}$	$2.81^{+0.23}_{-0.24}$	$11.55^{+0.10}_{-0.13}$	MgII	Y-J break	Strange PDZ	1
9.	J095930.43+015908.1	$2.68^{+0.11}_{-0.02}$	$1.71^{+0.08}_{-0.08}$	$10.05^{+0.06}_{-0.09}$	[OII]	Point		3
10.	J095842.35+015910.7	$2.91^{+0.19}_{-0.19}$	$1.97^{+0.12}_{-0.40}$	$10.39^{+0.13}_{-0.10}$	[OII]/MgII	None	Noisy, faint	3
11.	J095915.57+020026.6	$3.16^{+0.10}_{-0.10}$	$1.17^{+0.39}_{-0.11}$	$9.87^{+0.08}_{-0.16}$	MgII	Weak ems lines[1]	Faint	1
12.	J100217.74+020134.1	$3.50^{+0.05}_{-0.05}$	$1.56^{+0.09}_{-0.09}$	$9.54^{+0.09}_{-0.08}$	MgII	Ly-break	Flat SED	2
13.	J100030.08+020234.1	$3.36^{+0.07}_{-0.09}$	$1.53^{+0.10}_{-0.13}$	$10.14^{+0.08}_{-0.08}$	MgII	None	Compact	1
14.	J100023.18+020246.7	$3.40^{+0.17}_{-0.15}$	$1.88^{+0.30}_{-0.19}$	$10.59^{+0.10}_{-0.14}$	MgII	Ly-break		1
15.	J095745.01+020532.7	$3.51^{+0.05}_{-0.04}$	$1.33^{+0.10}_{-0.38}$	$9.35^{+0.14}_{-0.13}$	MgII	IA505+IA527[1]abs,Ly-break		2
16.	J100216.98+020553.3	$3.93^{+0.82}_{-3.61}$	$0.95^{+0.13}_{-0.12}$	$8.94^{+0.18}_{-0.19}$		Ly-break	Very strange PDZ	3
17.	J095854.97+021233.2	$4.42^{+0.14}_{-0.13}$	$1.69^{+0.11}_{-0.38}$	$10.09^{+0.14}_{-0.16}$	CII]	IA827ems, Ly-break	NB827:C IV	2
18.	J095919.71+021320.9	$3.68^{+0.05}_{-0.04}$	$1.06^{+0.47}_{-0.12}$	$9.31^{+0.14}_{-0.21}$	MgII	IA574ems, Ly-break	IA564 Lyα	2
19.	J100049.56+021329.9	$3.18^{+0.17}_{-0.12}$	$1.32^{+0.11}_{-0.34}$	$10.07^{+0.08}_{-0.08}$	MgII	Bright in H, Ks	F814; edge-on gal	1
20.	J095852.72+021514.1	$3.05^{+0.08}_{-0.07}$	$1.38^{+0.41}_{-0.12}$	$9.90^{+0.09}_{-0.15}$	MgII	IA484abs	IA484 Lyα	1
21.	J100216.54+021726.0	$4.38^{+0.07}_{-0.08}$	$1.80^{+0.07}_{-0.07}$	$9.97^{+0.10}_{-0.10}$	CII]	IA624abs, point	IA624 Lyα	2
22.	J095743.08+021907.3	$2.80^{+0.04}_{-0.23}$	$1.82^{+0.07}_{-0.08}$	$10.06^{+0.04}_{-0.05}$	[OII]	IA464+IA574abs[1]		3
23.	J100055.29+022121.0	$2.81^{+0.20}_{-0.19}$	$2.10^{+0.18}_{-0.33}$	$10.66^{+0.12}_{-0.12}$	[OII]	Faint below 10k Å		3
24.	J100048.45+022224.8	$3.63^{+0.09}_{-0.07}$	$1.87^{+0.46}_{-0.10}$	$10.57^{+0.06}_{-0.13}$	MgII	Ly-break		2
25.	J100220.34+022233.2	$3.04^{+0.18}_{-0.08}$	$1.30^{+0.30}_{-0.08}$	$10.80^{+0.05}_{-0.07}$	MgII	vHigh IRAC, weak Ly-break		1
26.	J095920.20+022500.1	$3.28^{+0.03}_{-0.02}$	$1.08^{+0.36}_{-0.16}$	$9.43^{+0.16}_{-0.18}$	MgII	None	Artifacts in Subaru	1
27.	J095741.34+022942.9	$3.37^{+0.14}_{-0.10}$	$1.61^{+0.10}_{-0.10}$	$10.04^{+0.10}_{-0.10}$	MgII	None		1
28.	J100140.52+023011.5	$2.71^{+0.19}_{-0.15}$	$1.86^{+0.10}_{-0.09}$	$11.10^{+0.04}_{-0.04}$	[OII]	Y-J break	F814; two peaks	3
29.	J095918.57+023053.5	$3.14^{+0.15}_{-0.21}$	$1.25^{+0.33}_{-0.10}$	$10.73^{+0.04}_{-0.05}$	MgII	Faint below 10k Å	F814; empty	1
30.	J100144.61+023145.4	$2.97^{+0.06}_{-0.06}$	$1.96^{+0.45}_{-0.14}$	$10.28^{+0.08}_{-0.08}$		None	Cluster	3
31.	J095757.60+023555.8	$2.90^{+0.05}_{-0.04}$	$2.10^{+0.07}_{-0.07}$	$9.85^{+0.05}_{-0.06}$		None	F814; 4 peaks	3
32.	J100223.44+024741.9	$3.50^{+0.05}_{-0.05}$	$2.06^{+0.41}_{-0.14}$	$10.37^{+0.12}_{-0.18}$	MgII	Point, bright IRAC	AGN?	2
33.	J100025.96+014633.2	$3.07^{+0.11}_{-0.13}$	$1.04^{+0.38}_{-0.11}$	$9.62^{+0.09}_{-0.17}$	MgII	IA484abs	IA484 Lyα	1
34.	J095919.91+021313.4	$3.72^{+0.04}_{-0.04}$	$1.65^{+0.08}_{-0.09}$	$9.54^{+0.06}_{-0.08}$	MgII	Lyman break		2

Table 5.4: Table showing good outliers. [1]: Features that are weak or almost insignificant. [2]: Point means that objects appears as point-like objects in all available filters. Category 1, 2, 3 are MgII emitters, Precise, and Lowlike categories. The last two outliers were added with the arrival of the final catalog from Laigle et al. (submitted).

5.2.1.2 J100009.82+014227.2

The redshift of 3.55 places NB118 nowhere near considered emission lines (MgII at $z = 3.26$, NeIV at $z = 3.90$). Additionally, its SED is very flat except at 6000 Å where the brightness drops towards lower wavelengths. This is most likely due to Lyman features. This is in correspondence with the redshift.

From F814W, a double peaked appearance is found, and the RGB image shows both distinct red, green, and blue areas with a white center. It might have local areas of increased star formation - it does have a slightly high SFR compared to its stellar mass (Karim et al., 2011).

5.2.1.3 J095914.48+014306.8

Another galaxy that may fall under the label 'low' but it has a somewhat higher and precise redshift. Also, it has a very high stellar mass ($\approx 10^{11} M_{\odot}$) which places it among one of the most massive ones in the sample. It appears larger on the sky than other objects in RGB but is not visible in F814W.

Looking at its SED, it is much more luminous in SPLASH and faint below the J-band. As such, its restframe optical radiation is faint. These points are all consistent with luminous infrared galaxy (LIRG), which are very gas rich (as discussed in chapter 2). While its SFR is below average to average, it is not consistent with the extremely low SFR (~ 10 $M_{\odot}$/yr) of ULIRG (Fang et al., 2014).

5.2.1.4 J095924.96+014513.2

As one of the brightest objects selected, this object shows a solid excess that is well-determined. Besides the NB118 excess, several other narrow band filters also show excess compared to what looks like a continuum. IB427, IA527, IA679, and NB816 all show signs of excess. In F814, it looks similar in size and shape.

The PDZ curve is very narrow, but this may be a consequence of the bad photo-z template fit, shown by the very large reduced chi-square value of around 14. Assuming this redshift is true, MgII is the closest important line. Using this redshift for the other narrow band filters, the filters have rest wavelengths of 1030 Å, 1273 Å, 1641 Å, and 1973 Å respectively. If we assume the redshift to be 3.25, the wavelengths become 1001 Å, 1237 Å, 1594 Å, and 1917 Å. Strong quasar emission lines include OVI at 1033 Å, Ly-a/NV at 1215/1240 Å, CIV at 1549 Å and CIII] at 1908 Å.

Another feature is the strong break at wavelengths lower than 4000 Å. The U filter brightness is one magnitude lower than the next broad band, B. At redshift 3.13/3.25, the Lyman limit is expected at 3766Å/3876 Å, which is pretty close the central wavelength of the U filter.

All of these points suggest that this is a quasar at photometric redshift 3.13/3.25. The fact that 5 narrow band filters show excess and correspond to strong quasar emission lines for the same redshift supports the notion.

5.2.1.5 J095919.74+015213.2

Its redshift does not place any emission lines in NB118. The SED does not reveal much, either. It is somewhat flat 7000 Å to 15000 Å, and even SPLASH and K_s filters are not much brighter. It does appear to have a drop in brightness below 7000Å, which corresponds to with Lyman features at this redshift. A possibility for the excess is MgII if the redshift is considered to be inaccurate.

It has relatively low stellar mass but above average SFR. Its appearance is fuzzy in Y and J but almost elongated in NB118. In F814W, there is a compact core embedded in

an an asymmetric envelope. Its irregular appearance and somewhat high but not extreme SFR may indicate some sort of merger or galactic interaction. A sample of local interacting galaxies are shown to have only a slight increase in SFR (Knapen et al., 2015).

5.2.1.6 J100034.41+015640.1

This galaxy holds the highest redshift ($z = 5.44$) of the good candidates. One of the most prominent features is the Lyman break which shows itself as a very sharp drop in brightness below 8000 Å. Despite this, it is still visible in F814W although faint. Additionally, it has a comparatively high SFR for its stellar mass, and its appearance in RGB and F814W is similar to that of the previous galaxy, J095919.74+015213.2

At this redshift, NB118 is situated close to CIII], which is an emission line commonly found in AGNs. However, the Lyman break and high SSFR suggests a different solution. CIII] is not usually associated with star formation, though Stark et al. (2015) and Patrício et al. (2015) have found this emission in young and star forming galaxies.

5.2.1.7 J095846.84+015802.7

In VISTA images, this object appears small, bright, and well-defined, and in F814W is has a compact core inside a small envelope. Its redshift is consistent with MgII emission in NB118, although it almost does not fulfill both selection criteria (c1: 0.31, c2: 3.10). It appears continuum dominated with a Lyman break at 5000 Å.

It is in some regards similar to the suspected quasar (J095924.96+014513.2) in the sample with regards to stellar mass and SFR, although it shows no signs of emission lines in the intermediate bands. It may be an AGN that is not as luminous and thus lack broad emission lines (Elitzur and Ho, 2009). Other explanations include a small starburst or similar that cause a significant increase in SFR in especially its nucleus. The presence of an AGN may quench SF (Mo et al., 2010) and is thus not consistent with the high SFR, although the derived SED properties may not be trustworthy in the presence of an AGN.

5.2.1.8 J100018.16+015822.6

With the latest catalog, this object changed dramatically. It is now similar to J095914.48+014306.8 (section 5.2.1.3) although its high redshift of 3.42 makes it a likely MgII emitter. Written before was:

"This galaxy is simultaneously the one with highest stellar mass and SFR (log $M_\star$ = 11.55 and log SFR = 3.40). Its SPLASH magnitudes are among some of the brightest seen in the sample despite being faint in especially towards optical filters. In fact, it is not visible in F814W. In RGB, it is area-wise large with a green core. Accompanying the main area is another area ~ 1.5" to the south. Whether or not these two areas are connected is impossible to tell, although the morphology and SFR would be consistent with a nuclear star burst caused by a merger (Mo et al., 2010; Smolčić et al., 2015)

It shares many properties with sub-mm galaxies and is suspected to be such. However, as mentioned in Smolčić et al. (2015), some degeneracies exist in SED-derived properties. Looking within this sample itself, this galaxy has some similarities with J095914.48+014306.8 (section 5.2.1.3) such as high SPLASH brightness, invisible in F814W, and large sky coverage in e.g J, though it is visible in optical bands. However, its redshift is much lower (2.77) and as is the log SFR (1.95). "

The only difference is a slight increase (δmag ~ 0.3) in brightness in SPLASH1 and SPLASH2 and suddenly its redshift is 0.8 lower and its SFR (log 2.81) places it as a main sequence star forming galaxy rather than a star burst with a stellar mass of log

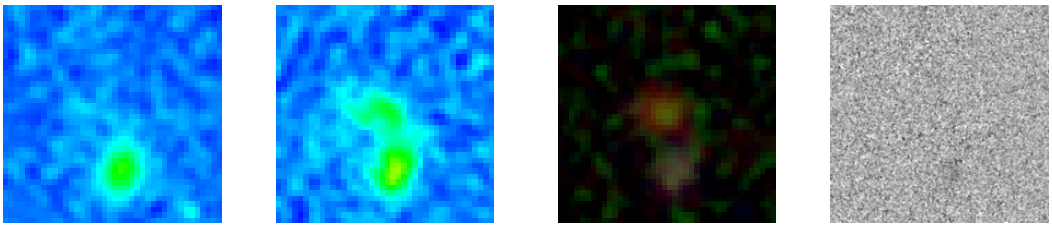

(a) Y (b) J (c) RGB (d) F814W

Figure 5.10: J100018.16+015822.6 morphology.

11.55. This stresses the importance of infrared measurements for deriving accurate SFR and stellar masses.

Note, however, that the large confidence interval in both redshift, SFR, and stellar mass may be due to the fact that the old best template still has a low χ^2 and may still be a considered a good explanation for this object.

5.2.1.9 J095930.43+015908.1

This candidate also changed its properties significantly with the final catalog. It is now similar to J095743.08+021907.3 (section 5.2.1.22). Previously written was:

"While this galaxy has a low redshift, it is much more luminous than objects with the 'low' label. Further inspection of its SED derived parameters also reveal a very high SFR. Galaxies on the main sequence of star formation (MSSF) at redshift 2.6 with an average log stellar mass of 9.50 has an average SFR of $12 \pm 5 M_{\odot}/yr$ (Karim et al., 2011) whereas this galaxy has one of 158 $M_{\odot}/yr$.

Its F814W appearance is irregular with a compact main core with a small core close to it (< 0.5"). Additionally, a diffuse cloud is visible around the cores. Its brightness may also be explained by the presence of an AGN, although AGNs tend to suppress star formation Silk and Rees (1998); Ilbert et al. (2013)."

5.2.1.10 J095842.35+015910.7

The brightness of this galaxy decreases monotonically towards lower wavelengths on a logarithmic scale and no other spectral features can be inferred from the SED partially due to the errors. The PDZ extents towards [OII], which may be the explanation for the NB118 excess.

5.2.1.11 J095915.57+020026.6

The redshift suggests MgII is placed on top of NB118 which shows a large excess (c1: 0.66) that almost is not significant (c2: 3.15). Excesses in the intermediate bands are perhaps present, but they are not significant. Another spectral feature is the Lyman break near 5000 Å, which supports the redshift of 3.16.

Morphologically, it is green in the center of an elongated red disk with a spatially small green companion just above the plane of the disk. The companion may be a background object, though. The idea of a disk galaxy may be inferred from F814W as well, which shows a diffuse elongated cloud with a bright center.

Its SFR and $M_{\star}$ places it as an average galaxy on the MSSF. MgII emission is seen in star forming galaxies (Kornei et al., 2013), although it is somewhat rare.

5.2.1.12 J100217.74+020134.1

Spectrally, it is very flat between above 5500 Å below which is a clear Lyman break. H, K_s, and SPLASH are slightly brighter than the flat part of the SED.

It is similar in appearance in RGB to the previously described galaxy but it is brighter and more compact in F814W. Additionally, its redshift does not match NB118 to any strong lines, yet MgII remains a good candidate if the photometric redshift is considered inaccurate.

5.2.1.13 J100030.08+020234.1

The extent of this galaxy is small in both RGB and F814W. It is almost entirely white with only a small red dominance in the periphery. In F814W, it appears compact and point like, which may point towards an active nuclei that dominate the host. Furthermore, NB118 most likely probes MgII given the redshift.

The SFR is below average for a galaxy of this stellar mass, which may be suppressed if there is indeed an AGN. Additionally, the Lyman break is very weak. Strong Lyman breaks are usually associated with young stellar populations and star forming galaxies (Mo et al., 2010). The weak Lyman break might thus be indicative of a UV continuum that stars cannot produce while an AGN can.

5.2.1.14 J100023.18+020246.7

The redshift is indicative of MgII in NB118 in which case the redshift of 3.40 is slightly wrong. Its SED is, however, difficult to interpret properly due to the large errors on most data points. Inspecting it in other images (Subaru and F814W) reveal that it is very faint, but there is definitely an object. A possible excess in NB711 can be seen, and assuming a redhift of 3.26 places it at 1670Å where both OIII] and HeII is located. They are, however, commonly associated with AGNs (Tilton and Shull, 2013).

Its SSFR is below average to average, yet it is hardly visible in several filters, including Y and F814W. It might indicate a red and dusty galaxy, which the RGB image somewhat confirms; red in the center with discrete green clumps.

5.2.1.15 J095745.01+020532.7

The SED, redshift, and appearance in RGB is very similar to that of J100217.74+020134.1 (section 5.2.1.12). The main difference is its low stellar mass (log 9.35) which may explain its lower brightness. It is not covered by F814W, but from its similarity to J100217.74+020134.1 suggests a similar compact structure.

Its redshift does not match with MgII. Additionally, the redshift is well-determined which makes arguing for large corrections troublesome. However, of the considered emission lines in this redshift regime, MgII remains a strong candidate.

5.2.1.16 J100216.98+020553.3

The SPLASH measurements on this object are either non-existent or have large errors. Lin et al. (2015) mention the importance of SPLASH data for accurate measurements of stellar mass of galaxies, which also manifests itself in the large 68% confidence interval (8.94 ± 0.20). As such, stellar mass and SFR may not be accurate for this galaxy. It is worth noting that the final Laigle catalog provides SPLASH1 and SPLASH2 measurements for this object but with magnitudes of $\sim 25.5 - 26.0$ and errors of 0.5 mag.

Morphologically, it is very compact and point like, especially in F814W, although it may appear to have a faint tidal tail.

No good explanations are found for the NB118 excess, although it is significant. A different redshift will place NB118 at either CII] or [NeIV]. They are, however, not strong candidates. CII] are sometimes found in AGNs and the compact appearance supports this notion. Additionally, IA624 seems to have a 1σ excess compared to the R filter. Assuming $z = 4.12$ which would correspond NB118 with CII], IA624 would cover 1210 Å - a wavelength that corresponds well with Lyα.

Another explanation may be that it is simply an object with a redshift of 0.5, which the PDZ suggests.

5.2.1.17 J095854.97+021233.2

The spectral and spatial appearance of this galaxy is very similar to the galaxy described above although it is several magnitudes brighter in SPLASH. Another difference is the well-determined redshift. The redshift does not correspond to any strong emission lines, but CII] at 4.12 may be a candidate.

5.2.1.18 J095919.71+021320.9

This galaxy is very similar to J100217.74+020134.1 (section 5.2.1.12), though almost a magnitude fainter. A feature of this galaxy is a significant excess in an intermediate band, IA574. A redshift of 3.68 places Lyα right on top of band. If this indeed is the case, it is not MgII in NB118. As will be discussed in section 5.2.3, there are galaxies with similar redshift that have no good explanation. However, the excess in NB118 appears more significant than the one in IA574 and as such more trustworthy. The nearest strong emission line is MgII and is therefore the prime candidate for the NB118 excess.

5.2.1.19 J100049.56+021329.9

Spectrally, it is similar to J100023.18+020246.7 (section 5.2.1.14) with although it is slightly fainter at wavelengths larger than 20000Å.

Its appearance is also similar in RGB but appears elongated in F814W. A possible explanation is that it is a galaxy viewed edge-on.

5.2.1.20 J095852.72+021514.1

The SED is very similar to that of J095915.57+020026.6 (section 5.2.1.11), although the properties derived from the SED is slightly different. It has an average SFR for its stellar mass content and is also slightly brighter ($\sim 0.1 - 0.4$ mag) between 5000Å and 50000Å.

5.2.1.21 J100216.54+021726.0

With a redshift of 4.38, there are no matching emission lines in NB118. It is somewhat similar to J095854.97+021233.2 (section 5.2.1.17) but is a lot brighter (1.0-1.5 mag) in several broad band filters, including Y and J. Additionally, it exhibits a strong Lyman break and absorption in an intermediate band (IA624). This may be due to Lyα absorption in either outflows or the intergalactic medium.

5.2.1.22 J095743.08+021907.3

Though not covered by F814W, it has a very irregular and diffuse shape in RGB where it is mostly red with lumpy green areas. The SED has a linear evolution using a logarithmic wavelength scale. Its low redshift might suggest [OII] in NB118, and its SFR, stellar mass and brightness suggests that this is a galaxy with average star formation.

5.2.1.23 J100055.29+022121.0

This galaxy is very similar to J095842.35+015910.7 (section 5.2.1.10) in all properties, althought its stellar mass is slightly higher with a SFR to match.

5.2.1.24 J100048.45+022224.8

In RGB, it shows a well-defined white center within a red halo, which is the same description in NB and J. In Y, however, it is fainter but still has a distinctive center. F814W substantiates this view, although the center is offset from a diffuse envelope.

The redshift does not correspond to any strong emission lines and its SED lacks further identifiers from intermediate bands. It does, however, have a prominent Lyman break.

It is worth noting that this galaxy has significantly changed its properties with the latest catalog. Before, it had log SFR= 2.27 and log $M_\star = 10.02$ and was described as:

"[...] the derived SED properties reveal a galaxy with above average stellar mass and very high SFR. On the SFMS, a galaxy of this stellar mass is expected to have a SFR of 38 ± 19 $M_\odot$/yr (Karim et al., 2011) whereas this one has a SFR of 186 ± 40 $M_\odot$/yr.

The high SFR and brightness point towards a starburst, which is also supported by the unusual appearance in F814W."

The latest catalog, though, it is has a low SFR (log SFR= 1.87) and higher stellar mass (log $M_\star = 10.57$). The main difference between the previous catalog and the new one is corrected SPLASH magnitudes. Indeed, this object has had its SPLASH1 and SPLASH2 magnitudes changed from $\sim 23.00, 22.45$ to $\sim 22.45, 22.30$ which has caused the log SFR to become 1.87 and log $M_\star = 10.57$. It has gone from an intermediate stellar mass and highly star forming galaxy to a heavy one with below average to average star formation. The large confidence intervals, though, may point towards the old best fitted template is still a very good fit.

5.2.1.25 J100220.34+022233.2

Spatially, it appears very small (~ 0.75") in RGB and F814W, but it is unusually bright in SPLASH channels and to some degree in H and K_s. Even in H and K_s, though, it is spatially very small (~ 0.75"). Further inspection in F814W reveals that it consists of 2-3 discrete clumps confined within 0.3".

It is a massive galaxy with a stellar mass of log 10.80 $M_\odot$ but coupled with a very low SFR of 1.30 $M_\odot$/yr. It is thus a somewhat massive and quiescent galaxy with a very small light radius. This is not unusual and has been studied in detail by e.g Toft et al. (2007) and Kriek et al. (2009).

5.2.1.26 J095920.20+022500.1

With a log stellar mass of only 9.43, it is one of the lightest in the sample. It is similar to other low stellar mass galaxies (J100217.74+020134.1, J095745.01+020532.7) in several aspects: (1) low stellar mass with high SFR, (2) flat SED between the Lyman break and SPLASH, and (3) bright peak(s) embedded in a diffuse halo.

There are a few buts in the comparison between this galaxy and the others. It has a redshift of 3.28, which strongly suggests MgII emission in NB118 - something that is not strongly suggested for the other two. Furthermore, the Lyman break is not as pronounced, but this may be due to the intermediate bands of Subaru. Upon inspection of these, it is seen that artifacts such as the ones described in section 5.2.1.1 exist in several of them.

5.2.1.27 J095741.34+022942.9

Both spectrally and spatially (in RGB) is similar to J100030.08+020234.1 (5.2.1.13) and is not given further description. The only difference is that this is not covered by F814W, but a similar compact appearance is expected.

5.2.1.28 J100140.52+023011.5

SED wise, it is similar to J100220.34+022233.2 (section 5.2.1.25) though roughly 0.5 magnitudes brighter as well as less redshifted. The derived properties are similar as well: massive and low SFR. As such, it follows the same considerations with a key difference. Its redshift of 2.88 places NB118 somewhere in between [OII] and MgII, but its SED suggest a less redshifted galaxy than J100220.34+022233.2. Therefore, the NB118 excess may very well be [OII].

5.2.1.29 J095918.57+023053.5

Although not as massive as J100220.34+022233.2, they are similar in several aspects. A significant difference, though, is the fact that this galaxy is not visible in F814W.

On another tangent, there is a possibility that this is not a real object. Just above it ($\sim$ 3") is a very bright source, above which again is another fuzzy cloud the same distance away from the bright source that appears brighter than this galaxy. In some broad and intermediate bands (see figure 5.11), these three lumps (i.e the target galaxy, the bright spot above, and the additional fuzzy cloud) appear connected and the non-central objects may be jet lobes. This is, however, *very* speculative.

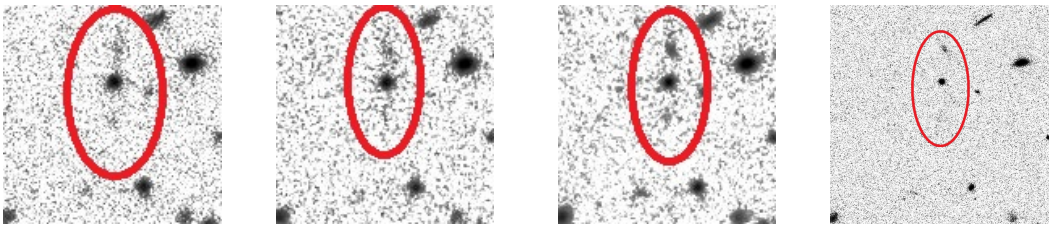

(a) Subaru U (b) Subaru IA767 (c) Subaru I (d) F814W

Figure 5.11: J095918.57+023053.5

5.2.1.30 J100144.61+023145.4

Its appearance is similar to that of J095743.08+021907.3 (section 5.2.1.22) as is its SED and the derived properties. The Lyman break is slightly stronger, though.

The photometry of this galaxy may be slightly contaminated by nearby objects. A faint band of light is seen across the 6" cutout with bright end points. Whether or not these objects are correlated to each other and how significant their impact on the photometry is are difficult to tell.

5.2.1.31 J095757.60+023555.8

As with the previously described galaxy, F814W reveals many bright peaks within a length of $\sim$ 1.5". The RGB image, though, show a clear separation of a red and green part. This may indicate that the different peaks are different objects.

Assuming this candidate is only a single candidate, though, it can be seen to share many similarities with J095930.43+015908.1 (section 5.2.1.9). They both have a high SFR, low stellar mass, a nearly flat SED, and an irregular appearance in F814W.

5.2.1.32 J100223.44+024741.9

This is in many ways similar to J095846.84+015802.7 (section 5.2.1.7) and J100048.45+022224.8 (section 5.2.1.24) and for a discussion is referred to the respective chapters.

5.2.1.33 J100025.96+014633.2

This is similar to J095915.57+020026.6 (section 5.2.1.11)

5.2.1.34 J095919.91+021313.4

This is similar to J100217.74+020134.1 (section 5.2.1.12)

5.2.2 MgII emitters

One category is used to describe a class of objects that has photometric redshifts near 3.26. This redshift places NB118 right on top of MgII. 13 objects are put into this category with redshifts ranging from 3.04 to 3.42 with moderate star formation rates (log SFR/$(M_\odot/yr) \sim 1.5$) and a wide range of stellar masses (log $M_\star/M_\odot \sim 9.70 - 10.95$). Generally, objects in this category have a small decline in magnitude towards lower wavelengths until the V-band where it drops sharply, which is due to the Lyman limit. Their appearance in RGB is usually a smooth red circle with declining brightness along the radius with green patches in the periphery and the center. Additionally, most of them are featureless in the intermediate bands. The bands appear to lie in the continuum as measured by the broad bands.

Despite their similarities, there are some differences. Inspecting their SEDs, derived properties, and appearance in F814W reveals two types: (a) Bright, low to moderate $M_\star$, and high SFR and (b) massive galaxies with low SFR.

Example F814W cutouts from each group can be seen in figure 5.12. Belonging in each group is ((number), name):

Type a (4.) J095924.96+014513.2, (7.) J095846.84+015802.7, (11.) J095915.57+020026.6, (13.) J100030.08+020234.1, (19.) J100049.56+021329.9, (20.) J095852.72+021514.1, (26.) J095920.20+022500.1, (27.) J095741.34+022942.9, and (33.) J100025.96+014633.2. Though galaxy 27 is not covered by F814W, its SED, SFR, and $M_\star$ is very similar to galaxy 13.

Type b (8.) J100018.16+015822.6, (14.) J100023.18+020246.7, (25.) J100220.34+022233.2, and (29.) J095918.57+023053.5. They are the galaxies with the highest stellar masses in this category

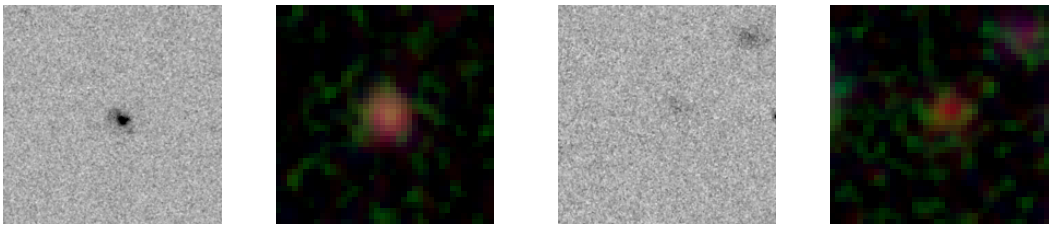

Type a F814W Type b RGB Type a F814W Type b RGB

Figure 5.12: Two types of MgII emitters in F814W and RGB. Type a (MgIIa) show a bright nucleis embedded in a shroud. Type b (MgIIb) have high stellar masses and are faint in F814W

Following is a discussion of what the nature of each type is.

5.2.2.1 Type a

These galaxies tend to be very bright and white in RGB images in the center with one or few green patches nearby. Overall, they are more red than green. The very bright centers and limited spatial extent is a feature observed in active galactic nuclei (AGN). Almeida et al. (2011) have studied the morphologies of intermediate redshift ($0.05 < z < 0.7$) radio galaxies similar in appearance to these and Bessiere et al. (2012) have numerous low redshift type 2 quasars with similar features. AGNs are among known causes for MgII emission lines due to the highly ionizing UV photons.

If AGNs are the cause of the MgII emission, other UV emission lines are expected. However, these objects are mostly featureless despite several strong lines are anticipated in the intermediate bands. One possible explanation for the lack of emission lines in the intermediate bands is low equivalent widths. In intermediate and broad bands, low equivalent widths are smoothed out. It can be speculated that obscuration of the broad line region (BLR) or weak emission from it can be the cause (Elitzur and Ho, 2009).

Another explanation of MgII emission is star formation. Kornei et al. (2013) observed that MgII emission strength is strongly correlated to specific star formation rate (SSFR), although dust attenuation and stellar mass also affect the emission strength. Furthermore, Kornei et al. (2013) speculate that galaxies with high SSFR, low attenuation, and low $M_\star$ represent a bursty, minimally-attenuated, low-mass stage of galaxy evolution. The emission is believed to be from scattering in outflowing gas and galactic winds caused by young and luminous stars due to the often-observed P Cygni profile of MgII (Martin et al., 2013; Weiner et al., 2009).

One galaxy that stands out in type sample is galaxy 4. The derived properties are very similar to that of other galaxies of this type, but as the only galaxy in the whole sample, it shows strong emission in the intermediate bands. Recalling from section 5.2.1.4, it is strongly suggested that this is a QSO. No other galaxies exhibit such strong evidence. While the rest of the galaxies of this type may show MgII emission due to star formation, the explanation is different for galaxy 4 - it is ionizing UV radiation from the central engine.

5.2.2.2 Type b

Galaxies with stellar masses upwards of $\log M_\star = 10.60$ are expected to have a SFR of 180 $M_\odot$/yr or more on the MSSF, yet these galaxies have below 100 $M_\odot$/yr (except galaxy 8 which has large confidence intervals on its properties). A different explanation from type a, i.e mostly star formation and AGNs to some degree, for MgII emission may thus be needed. Further evidence for this need is the correlation between MgII emission strength and low stellar mass, high SFR, and low dust attenuation (Kornei et al., 2013) - properties that type b galaxies all exhibit the opposite of.

Kriek et al. (2009) have found faint emission lines typical of low-ionization nuclear emission line regions in massive and low star forming galaxies. This suggests that a compact quiescent galaxy may contain a low luminosity AGN, though its contribution to the total optical light is only $\lesssim 8\%$. Toft et al. (2007) propose that the light is dominated by red and old stars - not an AGN or dust-enshrouded SF. However, that is not to say that these two contributions are ruled out. Toft et al. (2007) and Toft et al. (2007) looked at massive ($\gtrsim 10^{11}$ $M_\odot$) galaxies while type b galaxies are less massive and thus the results may not be directly transferable. The contribution to MgII emission may be a combination of outflows driven by SF, although they appear very dusty based on not being visible/faint in F814, and low-level AGN activity.

5.2.3 Precise redshift, no matching lines

A number of galaxies show very precise photometric redshifts that are not consistent with any of the considered strong galactic emission lines. There are several possible explanations for all objects and individual galaxies. The redshift can simply be wrong or there is an emission line that is not considered. An ever existing possibility is fluorescent FeII*. There are a total of 11 galaxies in this category, which can be subdivided into three further groups: (a) 3.6 redshift galaxies with 8 objects, (b) 4.4 redshifts galaxies with two objects, and (c) a 5.4 redshift galaxy. Thus, this group spans a large redshift range. Despite this fact, they show remarkably similar features: Low stellar masses ($\log M_\star \sim 9.5$) with above average SFR for their stellar masses (Karim et al., 2011). Some of these galaxies are observed in IRAC and generally show a low luminosity in it. RGB images of these galaxies are more red than blue, but they tend to be more green than anything. Most of them are also covered by F814W and they are all visible with lower redshift galaxies being slightly brighter.

Example F814W cutouts from each group can be seen in figure 5.14. Belonging in each group is ((number), name):

Type a (2.) J100009.82+014227.2, (5.) J095919.74+015213.2, (12.) 100217.74+020134.1, (15.) J095745.01+020532.7, (18.) J095919.71+021320.9, (24.) J100048.45+022224.8, (32.) J100223.44+024741.9, and (34.) J095919.91+021313.4. The stellar masses of the last two are slightly higher ($\log M_\star > 10$), but otherwise very similar to the rest in both SED and morphology.

Type b (17.) J095854.97+021233.2, and (21.) J100216.54+021726.0. They are different in regards to brightness but similar in everything else.

Type c (6.) J100034.41+015640.1. This is incidentally the highest redshift of all the candidates and show properties similar to the other galaxies in this category despite being at a different redshift.

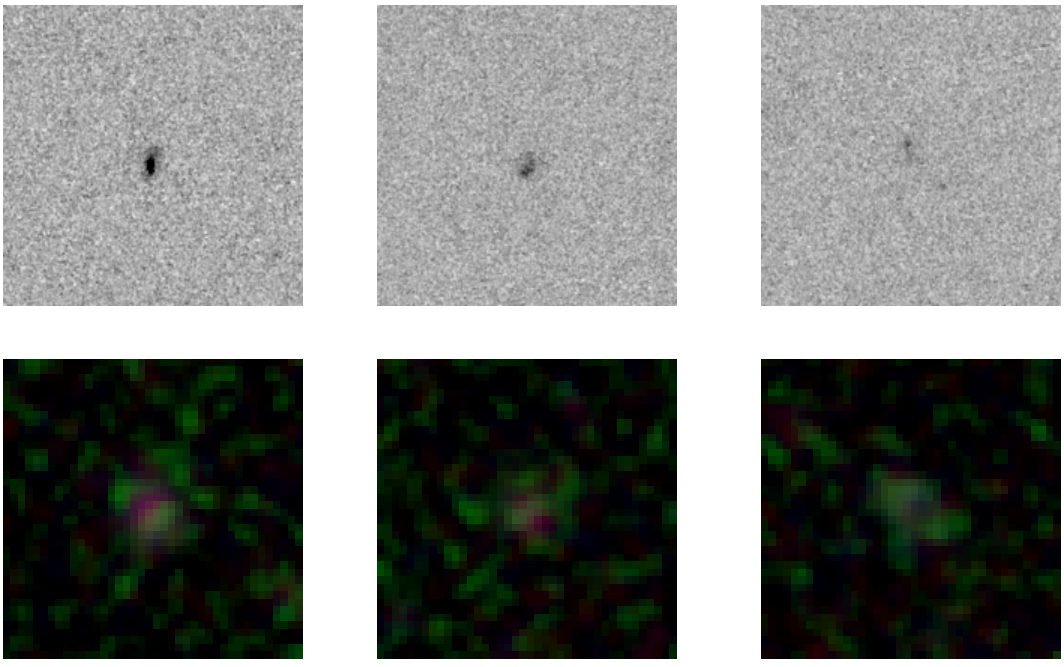

Type a Type b Type c

Figure 5.14: Different types of galaxies with precise redshifts but undetermined NB118 lines.

Following is a discussion of what the nature of each type is.

5.2.3.1 Type a

Type a galaxies have well-determined redshifts between 3.49 and 3.70 which corresponds to a wavelength inter void of strong emission line candidates for NB118. Despite this, MgII is considered a contender due to the similarities of these galaxies and the ones described in section 5.2.2.1.

To further correlate this type of galaxies with the ones in section 5.2.2.1, galaxy 7 and 32 are almost identical in all aspects. The log SFRs are the same (1.92 vs 1.99) with the same confidence interval, the log stellar masses are the same (10.30) and their magnitudes upwards of 6000 Å are similar $\Delta mag \lesssim 0.1$). Even their appearances are similar in both RGB and F814W: Very bright centers embedded in a diffuse but compact halo. The main difference is thus the redshift (3.08 vs 3.49).

Two spectral features that are weighted in computing the photometric redshift are the 4000-Å break and the Lyman break. The 4000-Å break is situated at 16320 Å and 17960 Å at these redshift which is near the central wavelength of the H ($\sim 16500 \pm 2900$ Å) band. It is possible that the brightness in H compared to the neighboring bands (J and K_s) plays a pivotal role in determining the position of the 4000-Å break, though that remains speculative. The Lyman break lies in the middle of several broad bands between $\sim 4000 - 6000$ Å. Galaxies in both this category and the ones described in section 5.2.2.1 exhibit a Lyman break feature. The exact position of this may be the deciding factor for the redshift computation.

Precise type a galaxies have the same explanation as the ones in section 5.2.2.1, which is referred to for a discussion of the origin of emission. This implies that MgII is suspected to be the origin of the NB118 excess and that the photometric redshift is wrong. It should be noted, though, that another likely explanation is FeII*. FeII* emission strength is found to be stronger with lower SFR (Kornei et al., 2013). The SFR of these galaxies are all larger than the average, which weakens the argument for FeII*. A third and equally likely explanation is that NB118 covers an emission line not considered. A significant number of the good outliers are in this category ($8/34 \sim 24\%$) which suggests a class of galaxies different from the MgII emitters.

5.2.3.2 Type b

A type of galaxy much similar to the previously described, however with a much higher redshift of 4.43. They both have low stellar masses with above average SFR. Appearance wise, they are both compact with a bright center within a spatially small diffuse cloud. The brighter of the two, galaxy 21, has a higher SFR and lower stellar mass, though, which may explain its brightness; more star light and possibly less dust attenuation.

As for possible emission lines, the discussion becomes difficult. CII] is located close to this redshift ($z \sim 4.12$), and the PDZ for both galaxies definitely allow a shift to this redshift. However, it is a line found in high redshift radio galaxies (HzRG) in their extended emission line region (De Breuck et al., 2000) and other types of AGNs, and it is found that CII] emission is stronger in shock ionization models compared to photo-ionization models. This may point towards low luminosity AGNs causing the emission. Radio data may aid in determining whether or not the NB excess is due to CII] but such data are not available.

5.2.3.3 Type c

The last type in this category only contains a single object, namely J100034.41+015640.1. A discussion of this object can be found in 5.2.1.6

5.2.4 Lowlike galaxies

As with the galaxies that received the label 'low' after the initial investigation of the selected candidates, galaxies in this category may also be [OII] emitters and will not receive an exhaustive analysis. They are, however, similar to several of the previously discussed types and their redshifts are precise at a redshift of 2.8. [NeV] is expected near 2.5 and HeI at 2.7. They may be the cause, but they are not common or found in many types of galaxies. [OII] is, though, which is why it remains a strong suspect.

Generally, the 10 galaxies in this category can be divided into two groups: (a) Main sequence star forming galaxies and (b) quiescent galaxies. Type a is the most numerous one with 8 galaxies while there only is two type b galaxies. The distributions and name are the following:

Type a (1.) J095753.08+013754.7, (9.) J095930.43+015908.1, (10.) J095842.35+015910.7, (16.) J100216.98+020553.3, (22.) J095743.08+021907.3, (23.) J100055.29+022121.0 (30.) J100144.61+023145.4, and (31.) J095757.60+023555.8.

Type b (3.) J095914.48+014306.8. and (28.) J100140.52+023011.5.

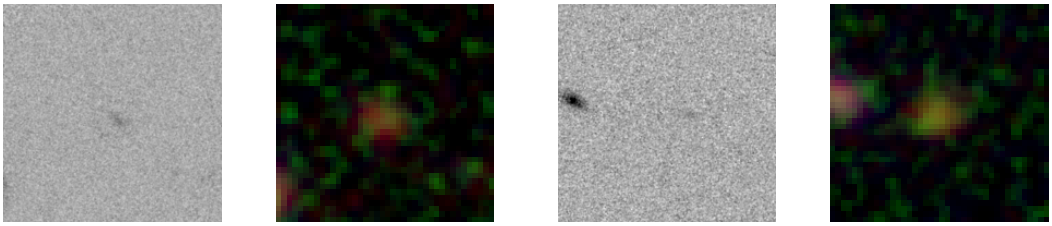

Type a F814W Type a RGB Type b F814W Type b RGB

Figure 5.15: Two types of low galaxies with type a being normal star-forming ones while type b is quiet.

5.2.4.1 Type a

The type a galaxies in this category have SFR and stellar masses that place them on the MSSF, in which case [OII] emission is a likely candidate for NB118 excess since it is a solid indicator of SF. The MSSF from Karim et al. (2011) describes them as slightly more star-forming than ordinary star-forming galaxies with their respective stellar masses.

5.2.4.2 Type b

Both galaxies have stellar masses above 10^{11} $M_\odot$ but star formations below 100 $M_\odot$/yr. This places them as somewhat quiet galaxies, but they may also be considered regular star-forming galaxies within their respective SFR and stellar mass confidence intervals. They do represent highest stellar mass objects with $z < 3$.

5.2.5 Main sequence of star formation

The selected galaxies can be plotted on the main sequence of star formation as given in Daddi et al. (2007). The sequence is roughly given as SFR $= 200 M_{11}^{0.9}$ where M_{11} is the stellar mass of a galaxy given in units of $M_\odot^{11}$. Figure 5.16 shows the main sequence given as a solid black line, and the dashed lines are $4^{\pm 1}\times$MS while the dotted lines are $10^{\pm 1}\times$MS. Thus it follows the appearance of figure 2.2. Additionally, the equation Karim

et al. (2011) found for SFR is plotted at three different redshifts as dash-dotted lines ($SSFR \propto M_\star^\beta\,(1+z)^n$).

It needs to be mentioned that the stellar mass and redshift regimes examined in Rodighiero et al. (2011) and Karim et al. (2011) are different from this study. As such, it is not possible to translate their findings directly to the ones in this study. Even then, certain trends appear in figure 5.16

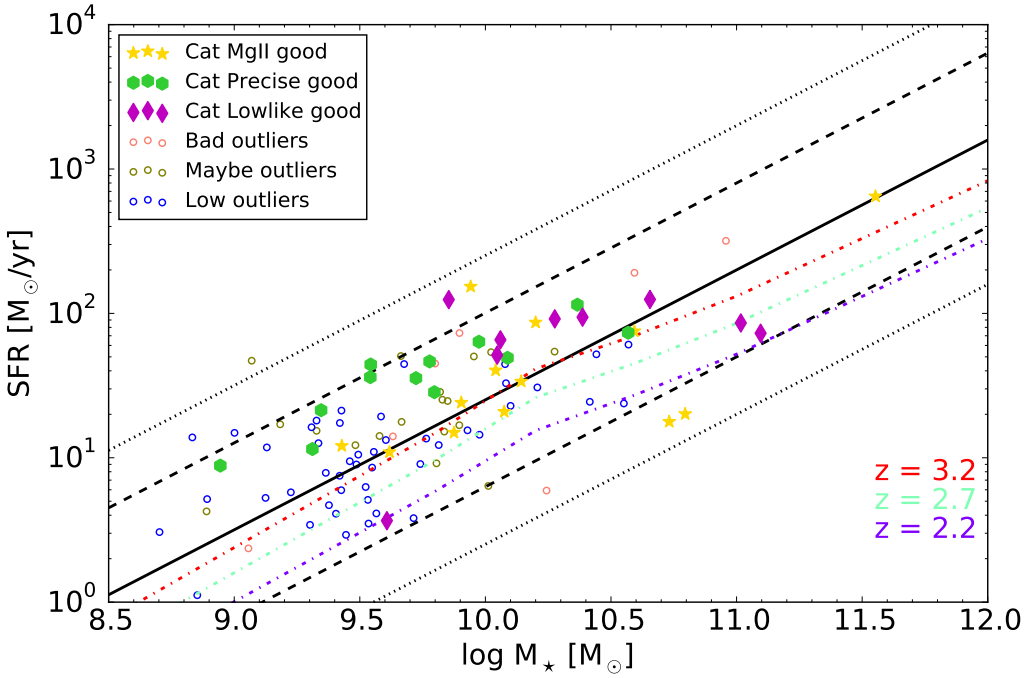

Figure 5.16: SFR versus stellar mass plot, imitating figure 2.2. It contains all of the selected candidates in their respective labels (see section 5.1). The good outliers are further subdivided into their categories as discussed in section 5.2. Two MSSF implementations are plotted alongside the data. The black lines follow the Daddi et al. (2007) relation SFR $= 200 M_{11}^{0.9}$ relation where the dashed lines are $4^{\pm1}\times$MS while the dotted lines are $10^{\pm1}\times$MS. The colored dash-dotted lines are from Karim et al. (2011) using the SSFR $= C\,M_\star^\beta \times (1+z)^n$ relation with values of $\beta = -0.44$, $n = [3.02, 3.42, 4.62, 3.48, 3.40, 3.40]$ in certain stellar mass intervals, $\log M_\star \in [8.5, 9.8, 10.2, 10.6, 11.0, 12.0]$, and $C = 10^{0.43}$. It should be noted that both models are limited to a max redshift of 2.5 and may thus not be representative for the sample of objects in this study.

MgII emitters closely follow the solid black main sequence, although three of them are clearly outliers. They are, however, easily identified as type MgIIb and J095924.96+014513.2 - the suspected quasar. Thus, type MgIIa appears to be main sequence star-forming galaxies while MgIIb galaxies are moderately massive quiescent galaxies with the exception of J100018.16+015822.6 (see section 5.2.1.8 for a discussion of this object).

Precise galaxies seem to have higher star formation across several magnitudes of stellar masses compared to MgII emitters. Type a are speculated to be MgII emitters themselves but their above average SFR may further indicate other processes. An explanation for their higher redshift may be more prominent Lyman breaks which are expected if the stellar population is somewhat young Mo et al. (2010).

While galaxies in the Lowlike category received little analysis, there is a clear distinguish between them and the galaxies that received the label 'low' prior to deeper analysis. The galaxies in the Lowlike *category* were the ones that made the cut for deeper analysis while

the *labeled* ones were not considered for an in-depth analysis. Generally, the category galaxies have the highest SFR of the two groups (with the exception of J095753.008+013754.4, log SFR=0.56, which is noticeably affected by Subaru artifacts), though not necessarily the highest masses.

The labeling was done on a subjective basis so the explanation is most likely to due with the author. However, the process involved inspection of the PDZ. Perhaps some galaxies with [OII] emission have SEDs that are degenerate with higher redshift low SFR galaxies which may translate into a broad PDZ.

6 | Conclusions

This section will summarize the findings from the previous chapters both in regards to the parameters of source extraction and candidate selection, but also the discussion and categorization of the selected candidates.

6.1 Parameters

The parameters discussed in this study include both source extraction and candidate selection with tables 5.2 and 5.3, respectively, showing the impact of changes to the values. Though table 5.2 is not updated with the final catalog, the conclusions remain the same.

Source extraction is very dependent on the detection threshold, especially on faint and high redshift objects. The chosen value, $\sigma = 1.5$ is in accordance with the value in Laigle et al. (submitted) and it seems to give good results. Higher values quickly diminish the number of redshift-matched objects indicating that high redshift objects are vulnerable to high detection thresholds. The detection area, though, does not have as large an effect, but it should be noted that only a small area regime has been examined. Laigle et al. (submitted) uses a minimum area value of 10 while this study only examined 3, 5, and 7. A minimum area of 5 is used for this study.

Candidate selection was made from condition 1 and 2 (equations 4.5 and 4.6) and shows that condition 2 gradually reduces the number of outliers while condition 1 has a slow drop until a cut-off value near 0.4. Having a strict (i.e high) condition 2 seems to be favorable as it ensures only robust candidates are found and a value of 3.0 seems appropriate for a study like this.

6.2 Selected candidates

The declared goal of this study is to find unusual galaxies at high redshifts ($\gtrsim 2.5$), though a large number of the 105 selected candidates, or outliers, shows signs of [OII] which places them at $z = 2.2$. Other outliers are the results of faults and defects in the detection image and are not suited for further analysis. They are, however, kept in the total sample for analysis purposes. Lastly, some outliers may be fine but are not picked for in-depth analysis due to uncertainty regarding their properties. The three distinctions yield the labels 'low', 'bad', and 'maybe', respectively. The outliers that are not labeled are considered good outliers.

The most numerous label is the 'low' label with 46 outliers while 'maybe' contains 18 and 'bad' has 7. This means that the remaining unlabeled 34 outliers are picked for in-depth analysis. The objects labeled 'low' and 'maybe' are still described briefly, though, and may be roughly classified according to what emission line their NB118 excesses cover. 'Low' labeled objects are likely [OII] emitters while 'maybe' objects are split equally between [OII], MgII, and an unknown emission line.

With this in mind, the total sample of selected candidates (not counting bad objects) consists of 97 with $\sim$ 64% being [OII] emitters (although it may be a different emission line between 3050-3400Å). $\sim$ 13%(28%) are MgII emitters where the parenthesis indicate Precise type a 5.2.3.1 objects and 1/3 of 'maybe' objects are counted as MgII emitters. $\sim$ 2% may be CII] emitters while only $\sim$ 1% is showing signs of CIII] emission.

The large number of galaxies near $z = 2.7$ is indicative of either a type of galaxy that systematically has a too high photometric redshift (i.e in case of [OII] emission) or has emission lines more commonly found in AGNs. In the case of a systematically

wrong photometric redshift, the nature of [OII] emitters, which commonly are star-forming galaxies, needs to be considered for template SED fitting.

6.2.1 Good outliers

The good outliers are categorized in three bins: (1) MgII emitters, (2) precise redshift without matching emission line in NB118 (Precise), and (3) possibly 'low' type galaxies (Lowlike). MgII emitters are the most numerous with 13/34 outliers while Precise outliers comes second with 11/34 and last is Low category galaxies with the remaining 10/34 outliers.

MgII emitters are further categorized dependent on their SFR and stellar mass. Type a contains 9 emitters which appear to have regular SFR compared to their stellar masses while type b emitters have high stellar masses and average to below average SFR. The latter type may represent passive galaxies.

Precise outliers consist mainly of $z \sim 3.7$ outliers (8 out of 11) which may be MgII emitters but other likely explanations are FeII* or an unusual emission line not considered. Two galaxies have $z \sim 4.4$ and may have CII] emission, which is unusual for regular star-forming galaxies, but these galaxies mostly have above average SFR for their stellar masses. Some highly star forming galaxies have shown signs of such emission. The last outlier has a redshift of 5.2 which is somewhat consistent with CIII] emission, which also has been found in young star forming galaxies (Stark et al., 2015; Patrício et al., 2015).

The Lowlike category contains 10 outliers and are characterized by a higher SFR compared the outliers with the label 'low' which may explain the reason why they escaped the label and picked for further analysis.

6.3 Main sequence of star formation

Figure 5.16 shows that MgII emitters follow the MSSF from both Karim et al. (2011) and Rodighiero et al. (2011) although with a few outliers. Precise outliers are slightly above the MSSF but this may be explained by a higher redshift and corresponding higher SFR in the earlier universe. The Low category shows increased SFR compared to the $z = 2.7$ main sequence as found in Karim et al. (2011) but this result is not conclusive.

Some outliers have been found with both extremely high and low SFRs. An MgII emitter has very high SFR for its stellar mass, but the object in question is very likely a quasar and the derived properties are thus not trustworthy. The Lowlike category outlier with high SFR is possibly a superposition of several objects, although it may be a merger. In the opposite spectrum, two MgII emitters are seen with very low SFR. These may be quiescent or passive galaxies.

6.4 SED derived properties

As mentioned throughout chapters 4 and 5, the properties derived from SED fitting play a huge role in the description of objects. The importance of infrared measurements for derived properties such as SFR and stellar mass is mentioned in Daddi et al. (2009) and Laigle et al. (submitted). In practice, this was seen with the arrival of the final catalog from Laigle et al. (submitted) where SPLASH1 and SPLASH2 magnitudes were corrected. This update resulted in minor changes for most outliers, but three galaxies significantly changed their derived properties even though the change in magnitudes was small (δmag ~ 0.3).

A | SED plots

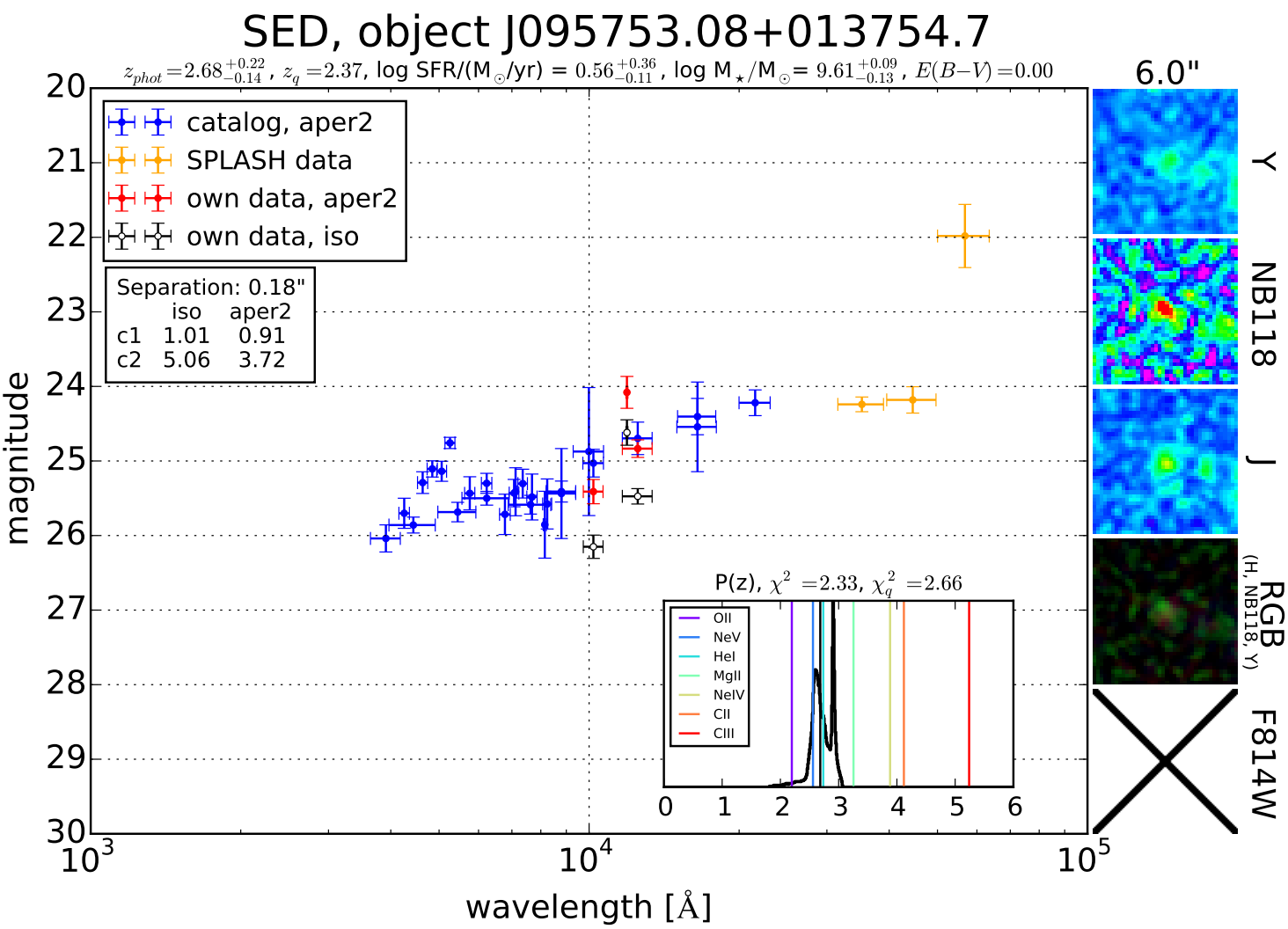
SED, object J095753.08+013754.7
$z_{phot}=2.68^{+0.22}_{-0.14}$, $z_q=2.37$, log SFR/(M$_\odot$/yr) = $0.56^{+0.36}_{-0.11}$, log M$_\star$/M$_\odot$= $9.61^{+0.09}_{-0.13}$, $E(B-V)=0.00$
catalog, aper2
SPLASH data
own data, aper2
own data, iso
Separation: 0.18"
iso aper2
c1 1.01 0.91
c2 5.06 3.72
P(z), $\chi^2=2.33$, $\chi^2_q=2.66$
OII
NeV
HeI
MgII
NeIV
CII
CIII
magnitude
wavelength [Å]
6.0"
Y
NB118
J
RGB
(H, NB118, Y)
F814W

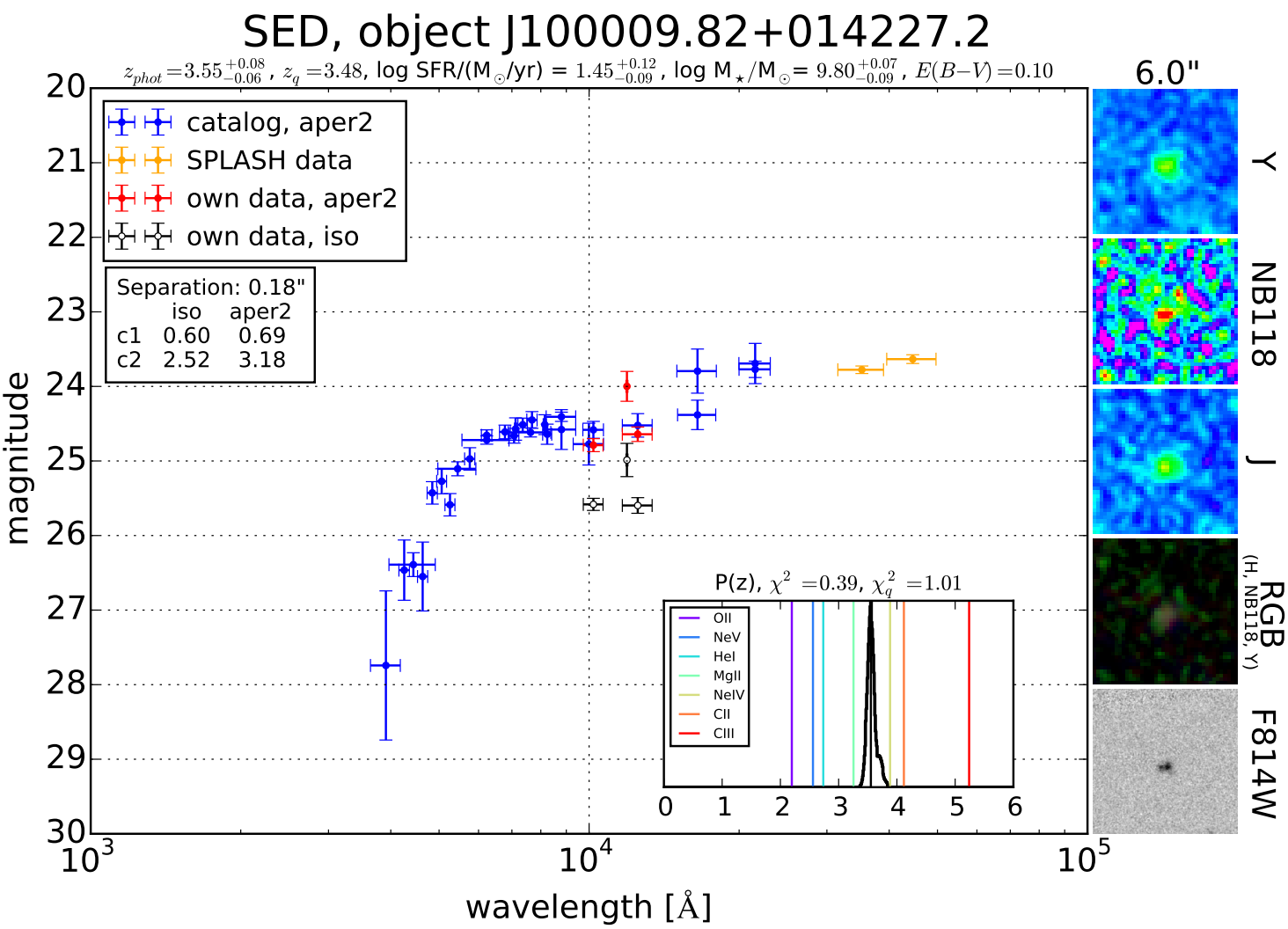
SED, object J100009.82+014227.2
$z_{phot}=3.55^{+0.08}_{-0.06}$, $z_q=3.48$, log SFR/(M$_\odot$/yr) = $1.45^{+0.12}_{-0.09}$, log M$_\star$/M$_\odot$= $9.80^{+0.07}_{-0.09}$, $E(B-V)=0.10$
catalog, aper2
SPLASH data
own data, aper2
own data, iso
Separation: 0.18"
iso aper2
c1 0.60 0.69
c2 2.52 3.18
P(z), $\chi^2=0.39$, $\chi^2_q=1.01$
OII
NeV
HeI
MgII
NeIV
CII
CIII
magnitude
wavelength [Å]
6.0"
Y
NB118
J
RGB
(H, NB118, Y)
F814W

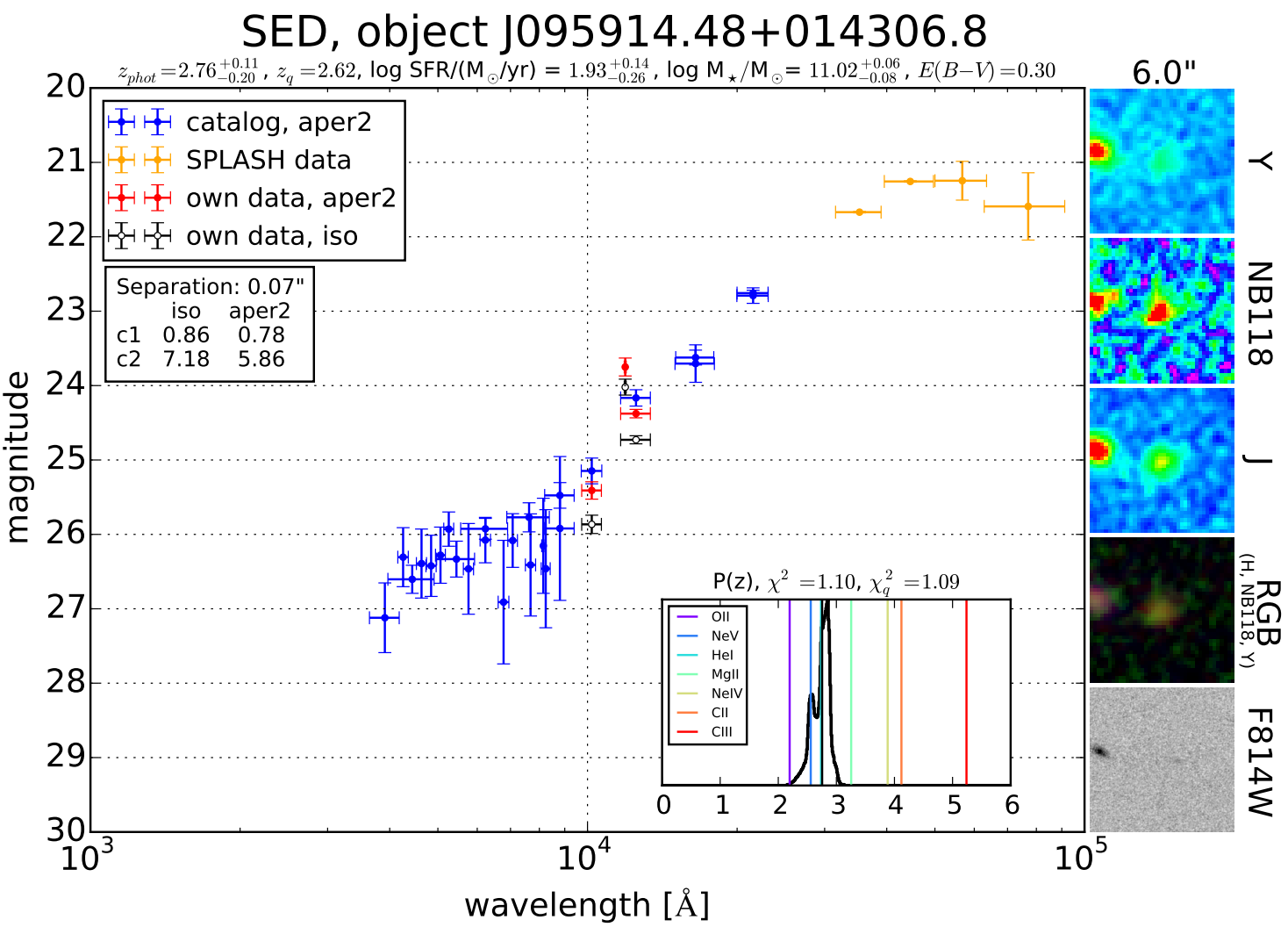
SED, object J095914.48+014306.8
$z_{phot}=2.76^{+0.11}_{-0.20}$, $z_q=2.62$, log SFR/(M$_\odot$/yr) = $1.93^{+0.14}_{-0.26}$, log M$_\star$/M$_\odot$= $11.02^{+0.06}_{-0.08}$, $E(B-V)=0.30$
catalog, aper2
SPLASH data
own data, aper2
own data, iso
Separation: 0.07"
iso aper2
c1 0.86 0.78
c2 7.18 5.86
P(z), $\chi^2=1.10$, $\chi^2_q=1.09$
OII
NeV
HeI
MgII
NeIV
CII
CIII
magnitude
wavelength [Å]
6.0"
Y
NB118
J
RGB
(H, NB118, Y)
F814W

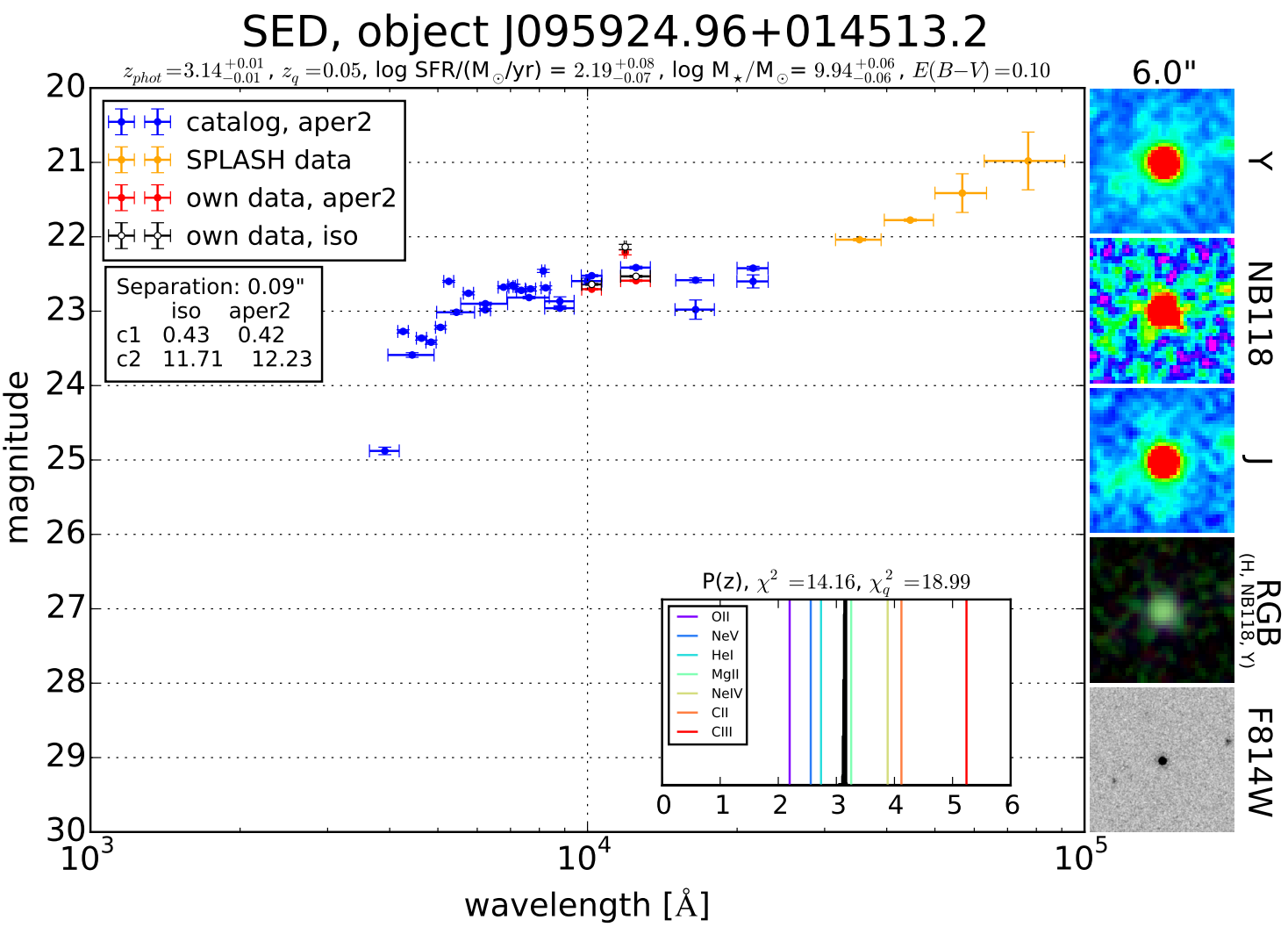
SED, object J095924.96+014513.2
$z_{phot}=3.14^{+0.01}_{-0.01}$, $z_q=0.05$, log SFR/(M$_\odot$/yr) = $2.19^{+0.08}_{-0.07}$, log M$_\star$/M$_\odot$= $9.94^{+0.06}_{-0.06}$, $E(B-V)=0.10$
catalog, aper2
SPLASH data
own data, aper2
own data, iso
Separation: 0.09"
iso aper2
c1 0.43 0.42
c2 11.71 12.23
P(z), $\chi^2=14.16$, $\chi^2_q=18.99$
OII
NeV
HeI
MgII
NeIV
CII
CIII
magnitude
wavelength [Å]
6.0"
Y
NB118
J
RGB
(H, NB118, Y)
F814W

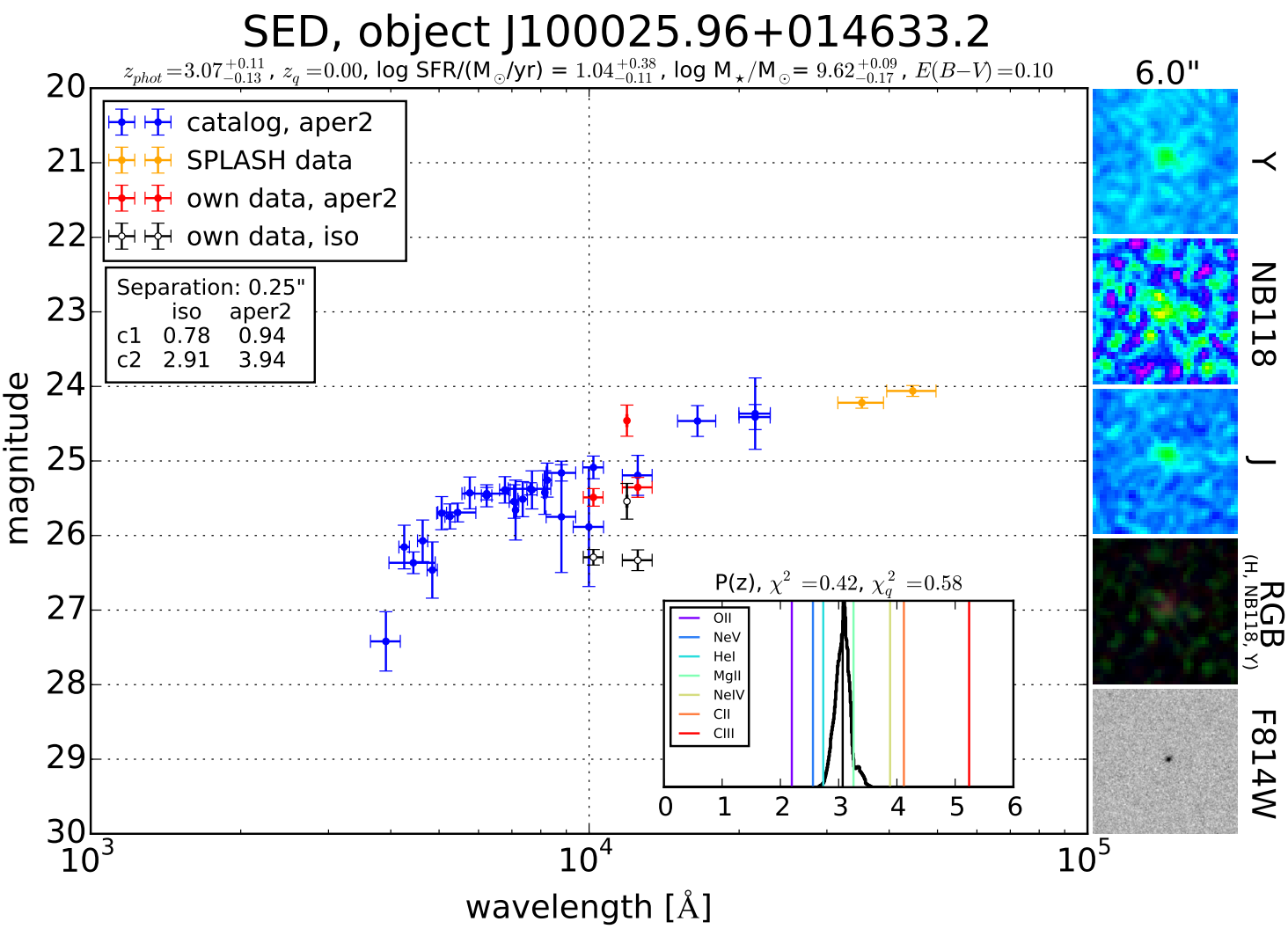
SED, object J100025.96+014633.2
$z_{phot}=3.07^{+0.11}_{-0.13}$, $z_q=0.00$, log SFR/(M$_\odot$/yr) = $1.04^{+0.38}_{-0.11}$, log M$_\star$/M$_\odot$= $9.62^{+0.09}_{-0.17}$, $E(B-V)=0.10$
catalog, aper2
SPLASH data
own data, aper2
own data, iso
Separation: 0.25"
iso aper2
c1 0.78 0.94
c2 2.91 3.94
P(z), $\chi^2=0.42$, $\chi^2_q=0.58$
OII
NeV
HeI
MgII
NeIV
CII
CIII
magnitude
wavelength [Å]
6.0"
Y
NB118
J
RGB
(H, NB118, Y)
F814W

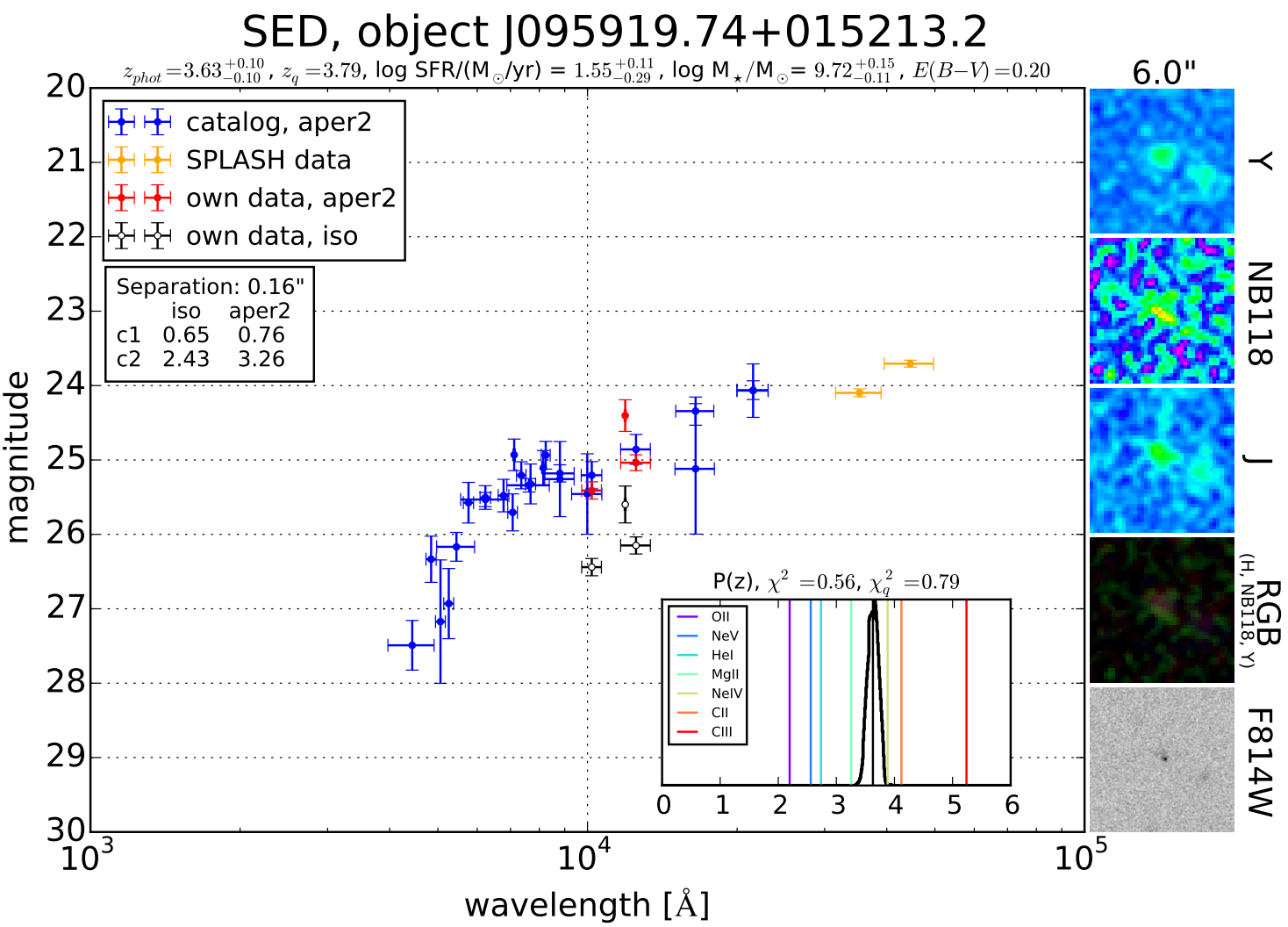
SED, object J095919.74+015213.2
$z_{phot}=3.63^{+0.10}_{-0.10}$, $z_q=3.79$, log SFR/(M$_\odot$/yr) = $1.55^{+0.11}_{-0.29}$, log M$_\star$/M$_\odot$= $9.72^{+0.15}_{-0.11}$, $E(B-V)=0.20$
catalog, aper2
SPLASH data
own data, aper2
own data, iso
Separation: 0.16"
iso aper2
c1 0.65 0.76
c2 2.43 3.26
P(z), $\chi^2=0.56$, $\chi^2_q=0.79$
OII
NeV
HeI
MgII
NeIV
CII
CIII
magnitude
wavelength [Å]
6.0"
Y
NB118
J
RGB
(H, NB118, Y)
F814W

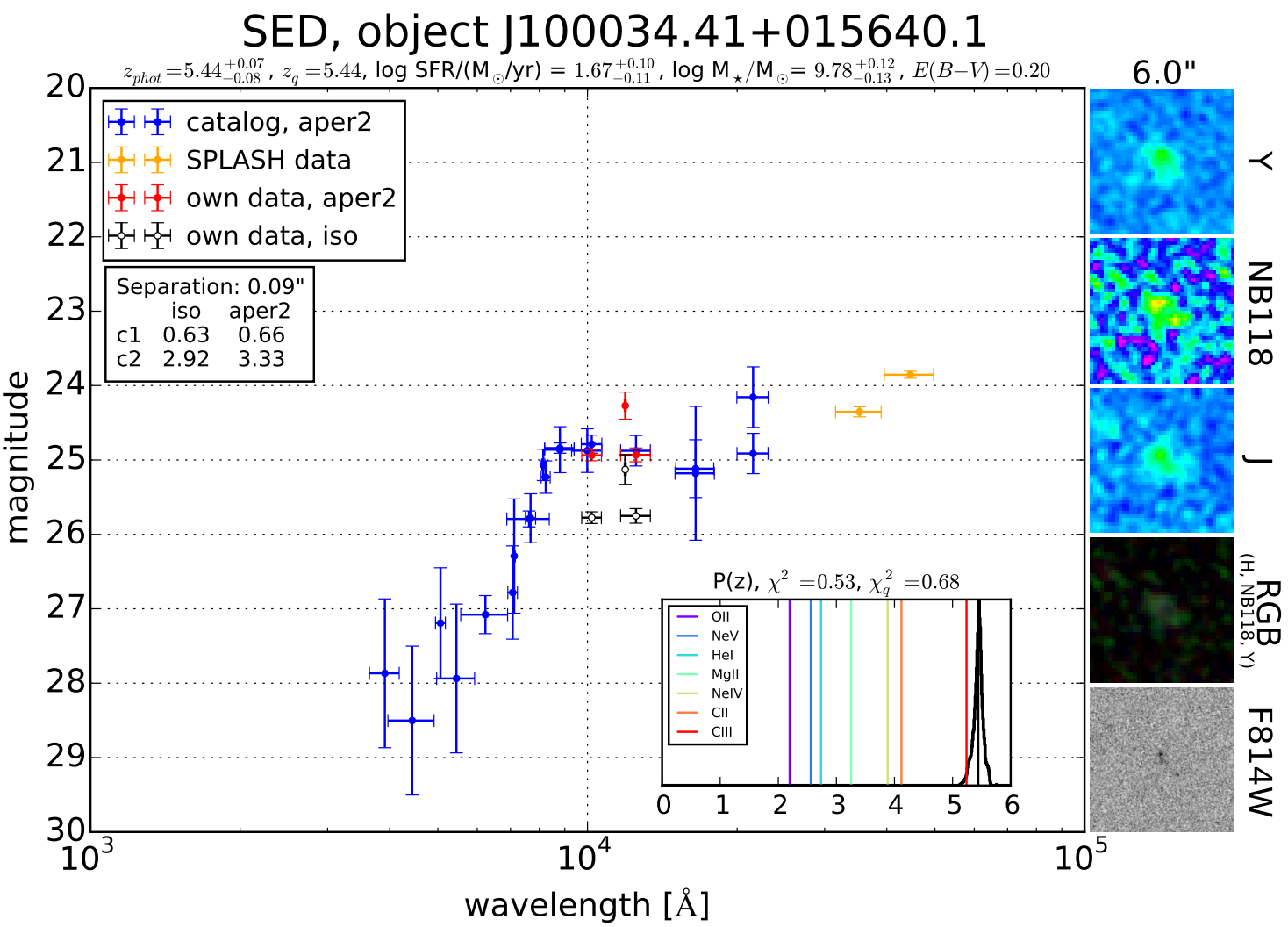
SED, object J100034.41+015640.1
$z_{phot}=5.44^{+0.07}_{-0.08}$, $z_q=5.44$, log SFR/(M$_\odot$/yr) = $1.67^{+0.10}_{-0.11}$, log M$_\star$/M$_\odot$= $9.78^{+0.12}_{-0.13}$, $E(B-V)=0.20$
catalog, aper2
SPLASH data
own data, aper2
own data, iso
Separation: 0.09"
iso aper2
c1 0.63 0.66
c2 2.92 3.33
P(z), $\chi^2=0.53$, $\chi^2_q=0.68$
OII
NeV
HeI
MgII
NeIV
CII
CIII
magnitude
wavelength [Å]
6.0"
Y
NB118
J
RGB
(H, NB118, Y)
F814W

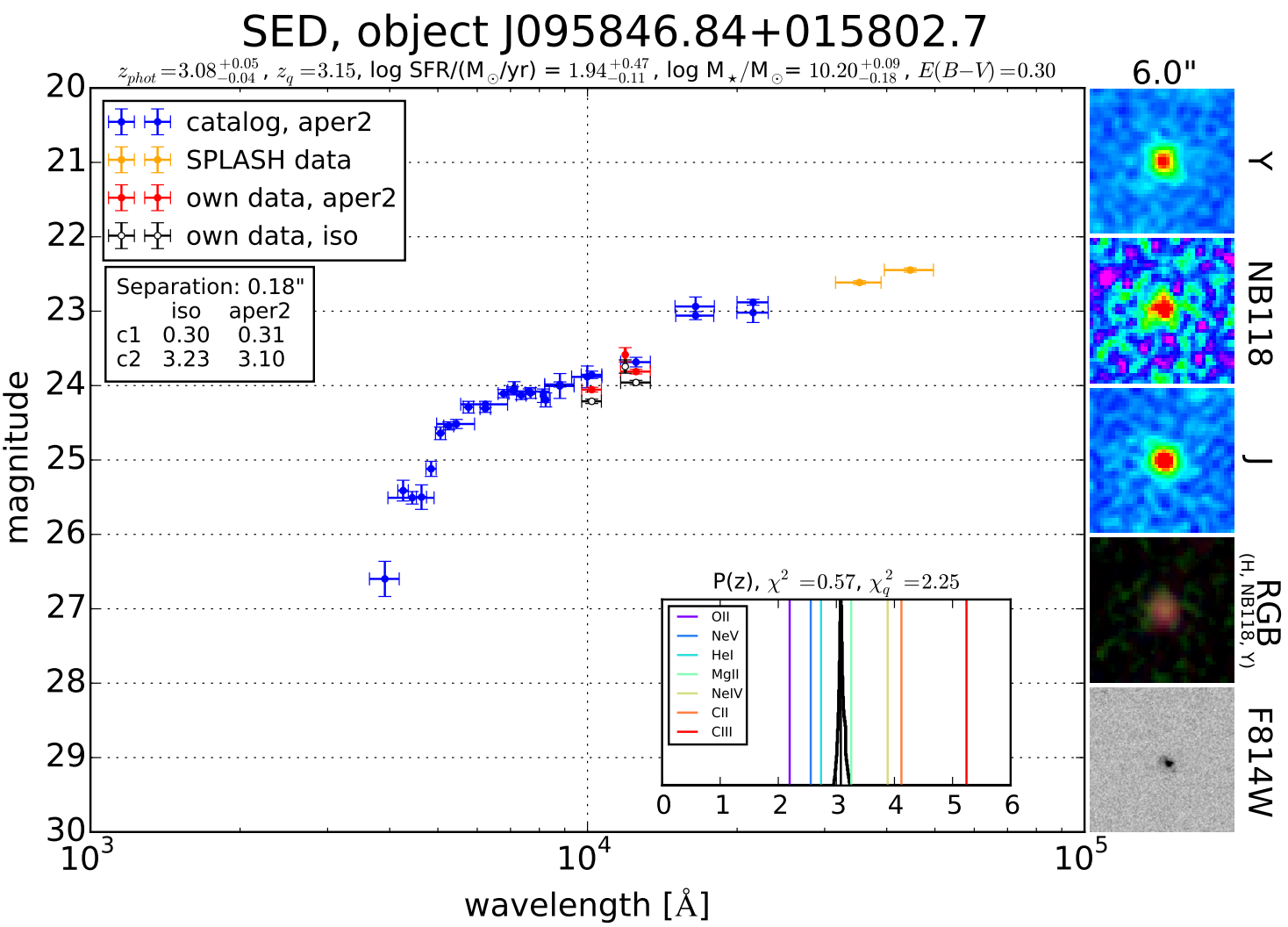
SED, object J095846.84+015802.7
$z_{phot}=3.08^{+0.05}_{-0.04}$, $z_q=3.15$, log SFR/(M$_\odot$/yr) = $1.94^{+0.47}_{-0.11}$, log M$_\star$/M$_\odot$= $10.20^{+0.09}_{-0.18}$, $E(B-V)=0.30$
catalog, aper2
SPLASH data
own data, aper2
own data, iso
Separation: 0.18"
iso aper2
c1 0.30 0.31
c2 3.23 3.10
P(z), $\chi^2=0.57$, $\chi^2_q=2.25$
OII
NeV
HeI
MgII
NeIV
CII
CIII
magnitude
wavelength [Å]
6.0"
Y
NB118
J
RGB
(H, NB118, Y)
F814W

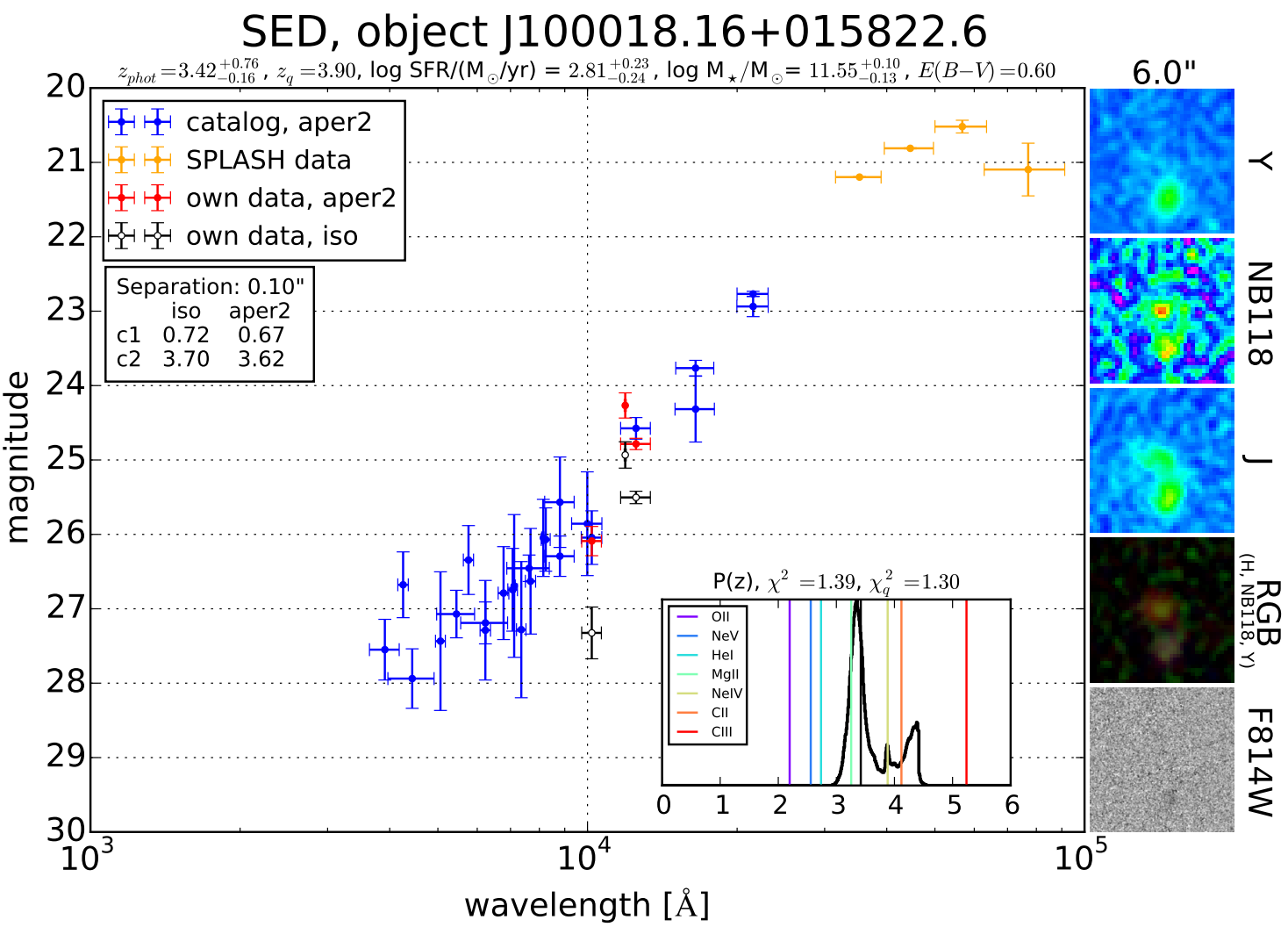
SED, object J100018.16+015822.6
$z_{phot}=3.42^{+0.76}_{-0.16}$, $z_q=3.90$, log SFR/(M$_\odot$/yr) = $2.81^{+0.23}_{-0.24}$, log M$_\star$/M$_\odot$= $11.55^{+0.10}_{-0.13}$, $E(B-V)=0.60$
catalog, aper2
SPLASH data
own data, aper2
own data, iso
Separation: 0.10"
iso aper2
c1 0.72 0.67
c2 3.70 3.62
P(z), $\chi^2=1.39$, $\chi^2_q=1.30$
OII
NeV
HeI
MgII
NeIV
CII
CIII
magnitude
wavelength [Å]
6.0"
Y
NB118
J
RGB
(H, NB118, Y)
F814W

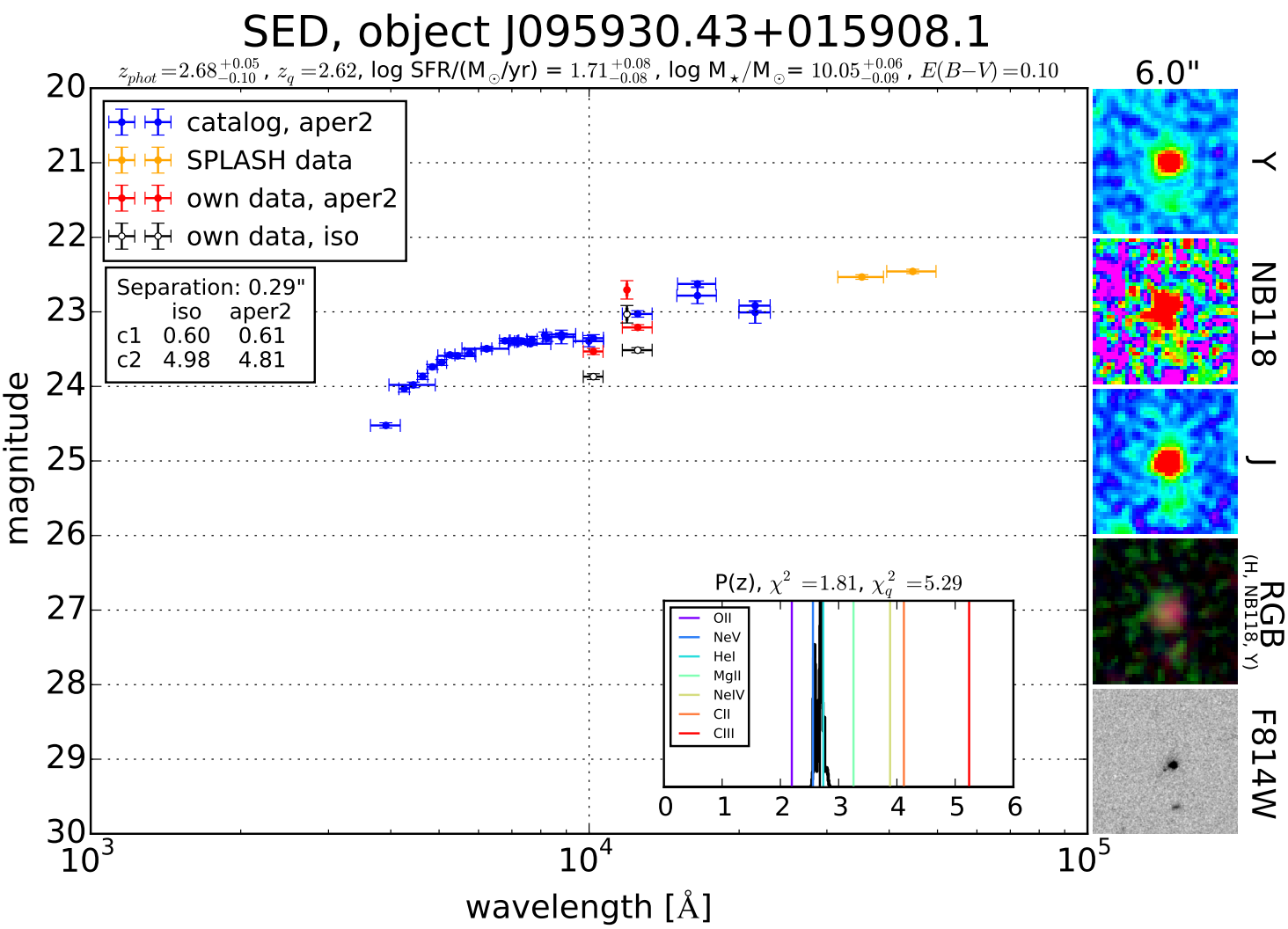
SED, object J095930.43+015908.1
$z_{phot}=2.68^{+0.05}_{-0.10}$, $z_q=2.62$, log SFR/(M$_\odot$/yr) = $1.71^{+0.08}_{-0.08}$, log M$_\star$/M$_\odot$= $10.05^{+0.06}_{-0.09}$, $E(B-V)=0.10$
catalog, aper2
SPLASH data
own data, aper2
own data, iso
Separation: 0.29"
iso aper2
c1 0.60 0.61
c2 4.98 4.81
P(z), $\chi^2=1.81$, $\chi^2_q=5.29$
OII
NeV
HeI
MgII
NeIV
CII
CIII
magnitude
wavelength [Å]
6.0"
Y
NB118
J
RGB
(H, NB118, Y)
F814W

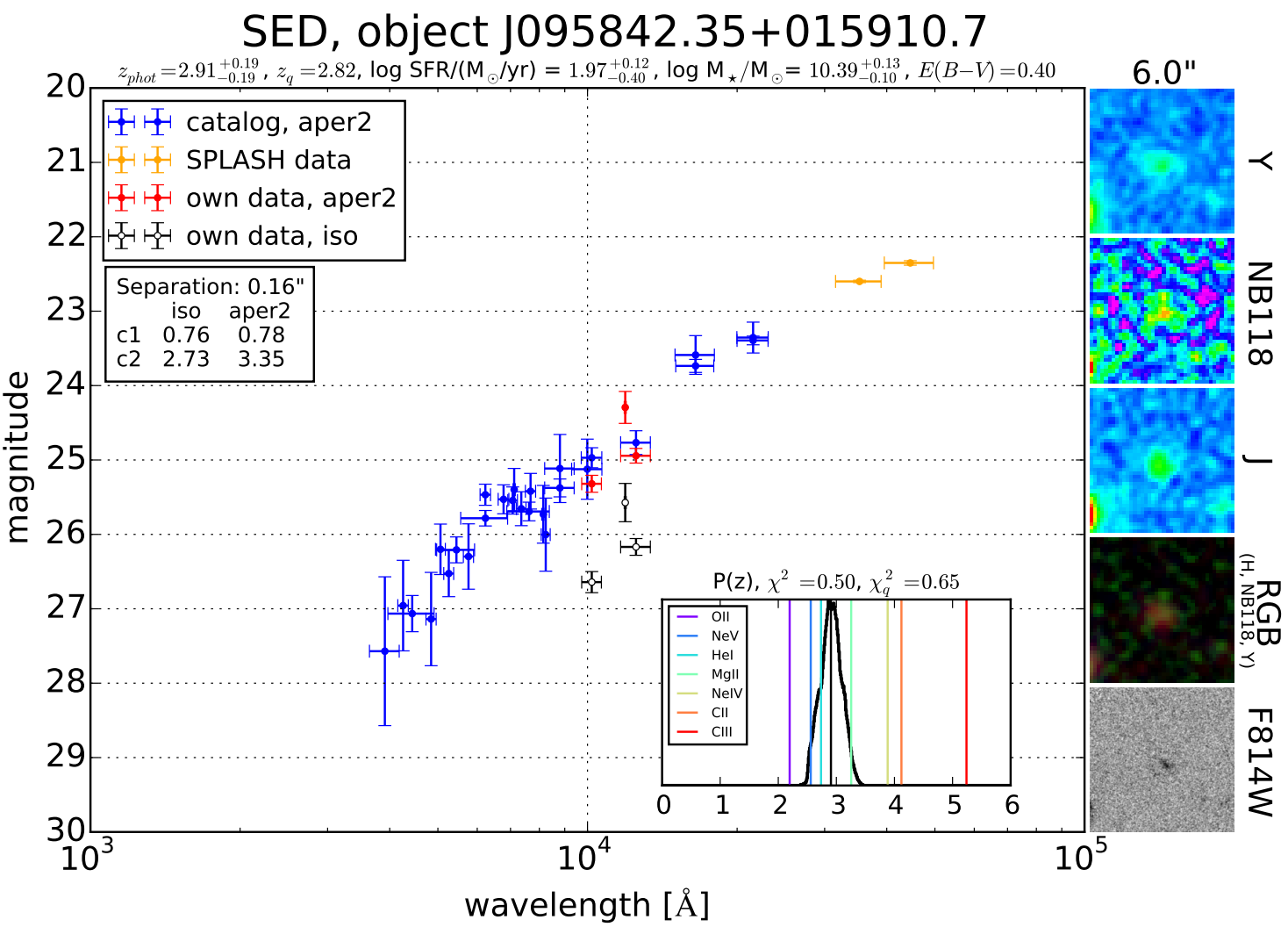
SED, object J095842.35+015910.7
$z_{phot}=2.91^{+0.19}_{-0.19}$, $z_q=2.82$, log SFR/(M$_\odot$/yr) = $1.97^{+0.12}_{-0.40}$, log M$_\star$/M$_\odot$= $10.39^{+0.13}_{-0.10}$, $E(B-V)=0.40$
catalog, aper2
SPLASH data
own data, aper2
own data, iso
Separation: 0.16"
iso aper2
c1 0.76 0.78
c2 2.73 3.35
P(z), $\chi^2=0.50$, $\chi^2_q=0.65$
OII
NeV
HeI
MgII
NeIV
CII
CIII
magnitude
wavelength [Å]
6.0"
Y
NB118
J
RGB
(H, NB118, Y)
F814W

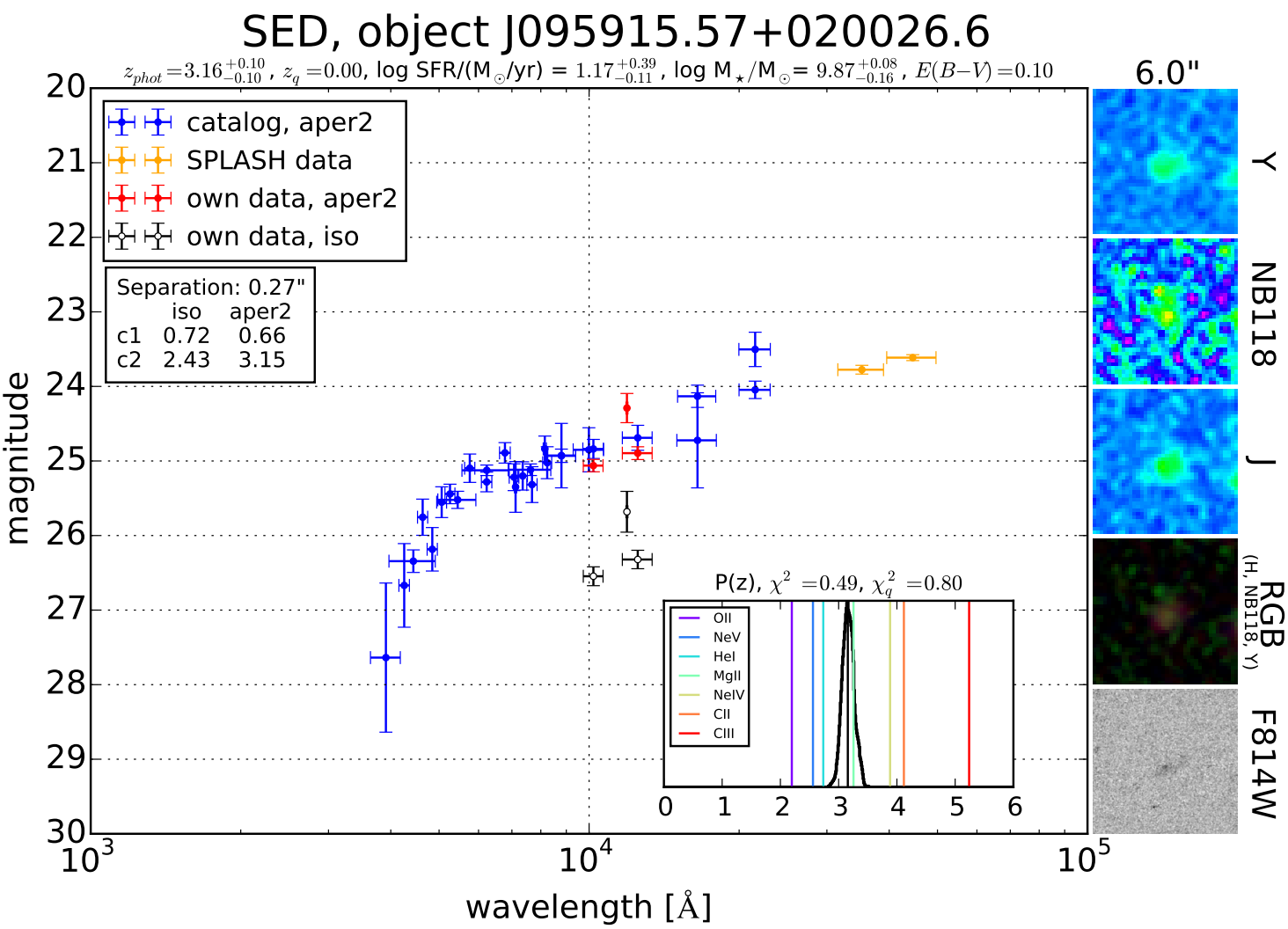
SED, object J095915.57+020026.6
$z_{phot}=3.16^{+0.10}_{-0.10}$, $z_q=0.00$, log SFR/(M$_\odot$/yr) = $1.17^{+0.39}_{-0.11}$, log M$_\star$/M$_\odot$= $9.87^{+0.08}_{-0.16}$, $E(B-V)=0.10$
catalog, aper2
SPLASH data
own data, aper2
own data, iso
Separation: 0.27"
iso aper2
c1 0.72 0.66
c2 2.43 3.15
P(z), $\chi^2=0.49$, $\chi^2_q=0.80$
OII
NeV
HeI
MgII
NeIV
CII
CIII
magnitude
wavelength [Å]
6.0"
Y
NB118
J
RGB
(H, NB118, Y)
F814W

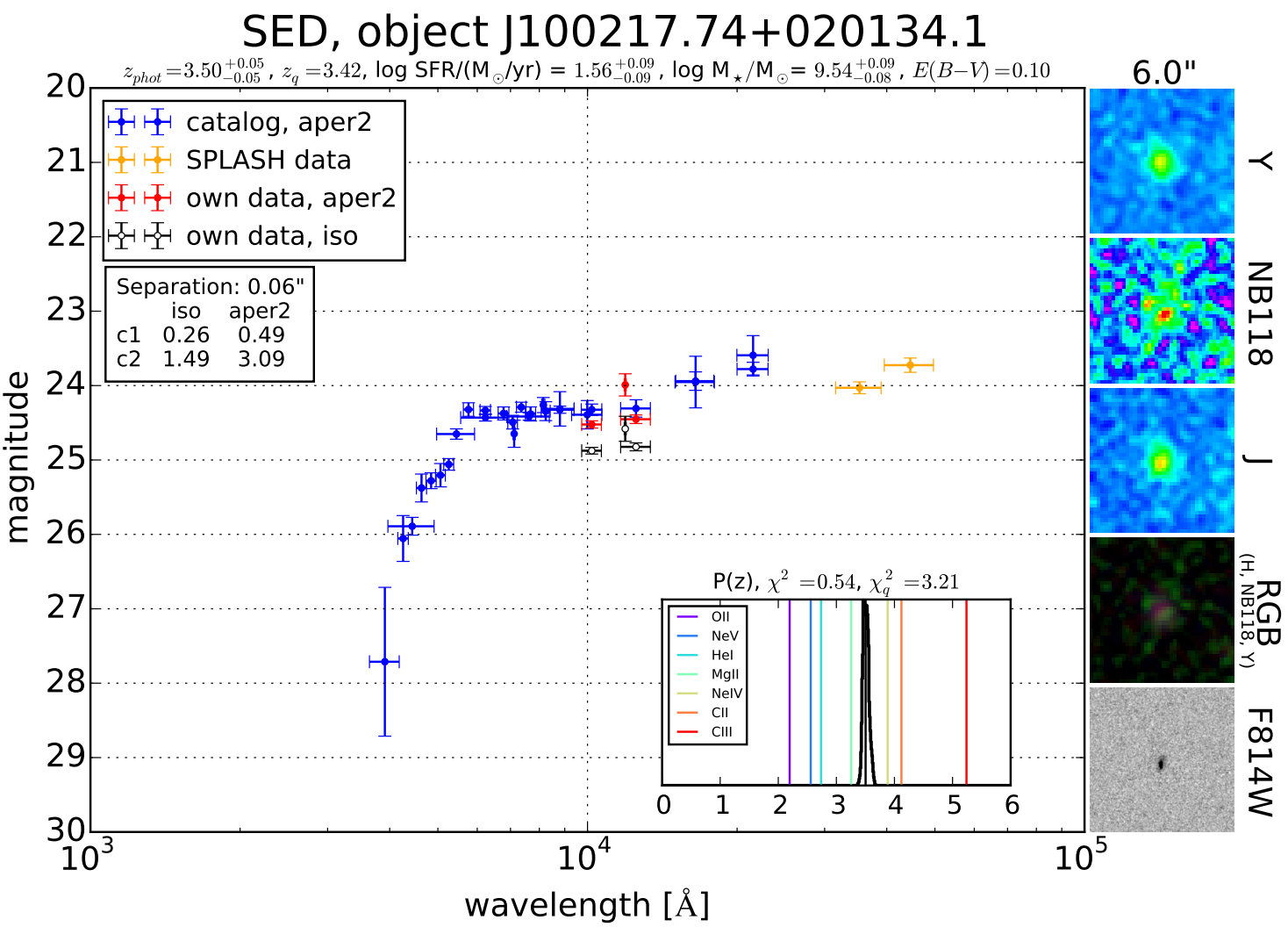
SED, object J100217.74+020134.1
$z_{phot}=3.50^{+0.05}_{-0.05}$, $z_q=3.42$, log SFR/(M$_\odot$/yr) = $1.56^{+0.09}_{-0.09}$, log M$_\star$/M$_\odot$= $9.54^{+0.09}_{-0.08}$, $E(B-V)=0.10$
catalog, aper2
SPLASH data
own data, aper2
own data, iso
Separation: 0.06"
iso aper2
c1 0.26 0.49
c2 1.49 3.09
P(z), $\chi^2=0.54$, $\chi^2_q=3.21$
OII
NeV
HeI
MgII
NeIV
CII
CIII
magnitude
wavelength [Å]
6.0"
Y
NB118
J
RGB
(H, NB118, Y)
F814W

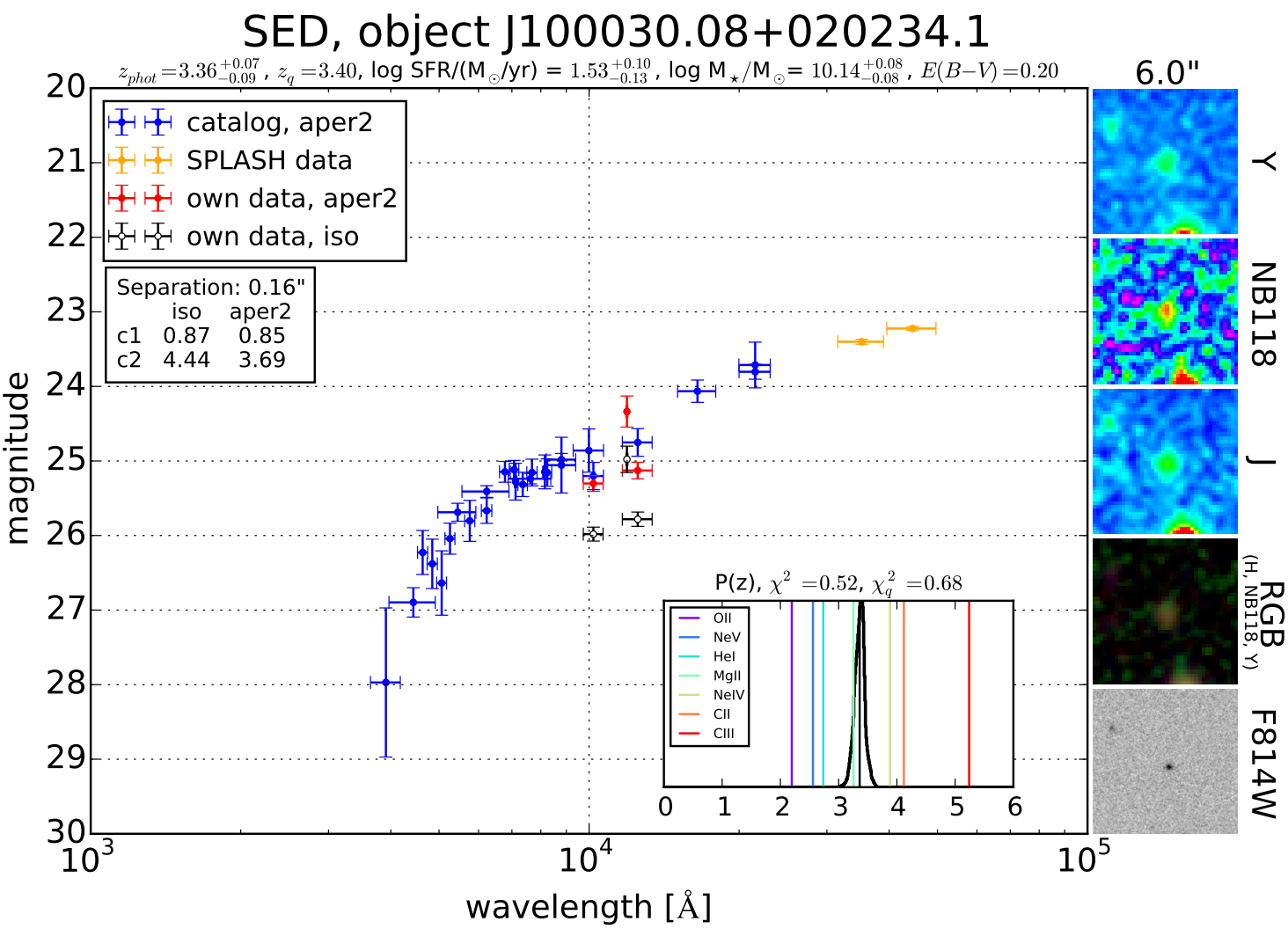
SED, object J100030.08+020234.1
$z_{phot}=3.36^{+0.07}_{-0.09}$, $z_q=3.40$, log SFR/(M$_\odot$/yr) = $1.53^{+0.10}_{-0.13}$, log M$_\star$/M$_\odot$= $10.14^{+0.08}_{-0.08}$, $E(B-V)=0.20$
catalog, aper2
SPLASH data
own data, aper2
own data, iso
Separation: 0.16"
iso aper2
c1 0.87 0.85
c2 4.44 3.69
P(z), $\chi^2=0.52$, $\chi^2_q=0.68$
OII
NeV
HeI
MgII
NeIV
CII
CIII
magnitude
wavelength [Å]
6.0"
Y
NB118
J
RGB
(H, NB118, Y)
F814W

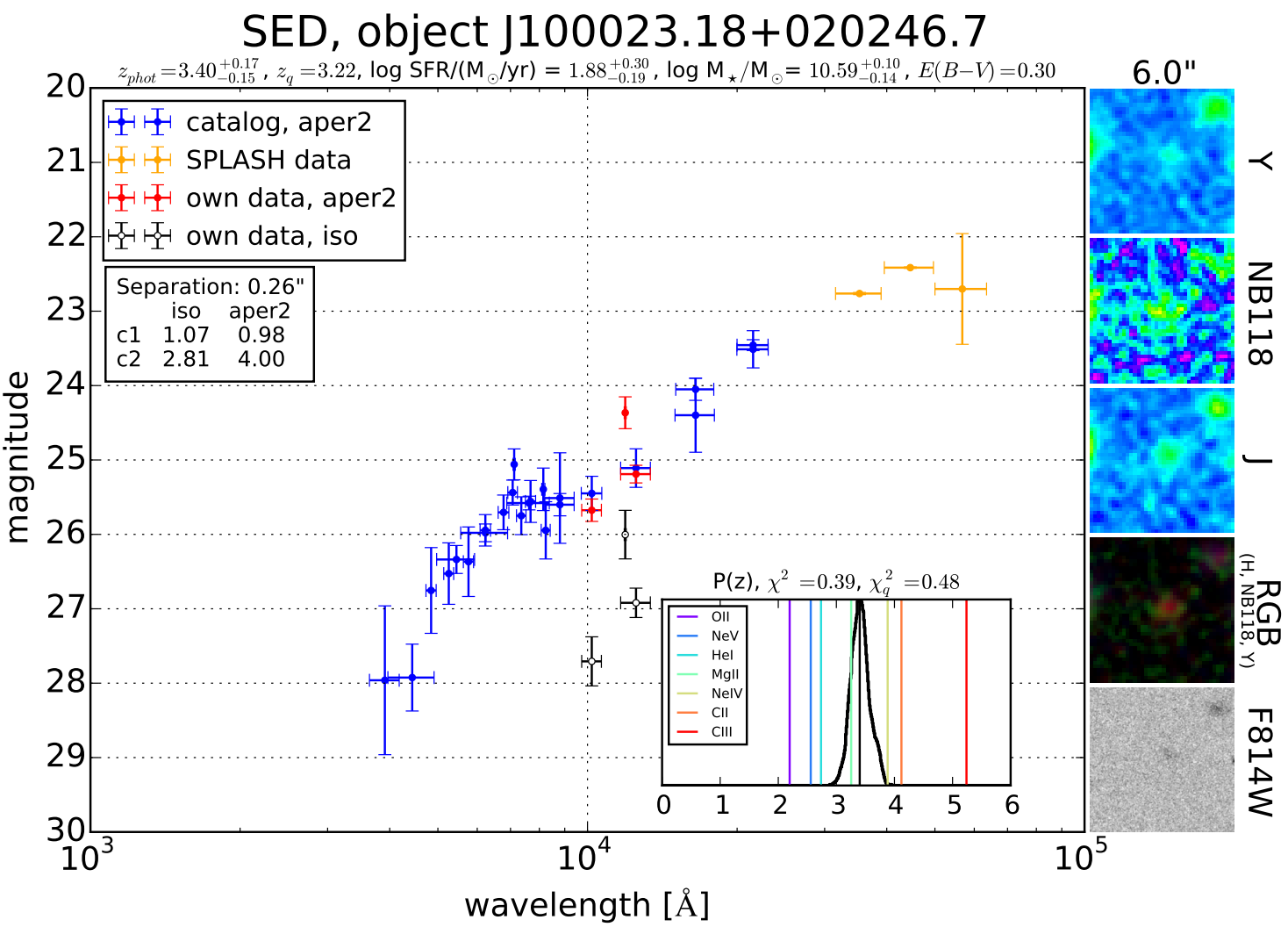
SED, object J100023.18+020246.7
$z_{phot}=3.40^{+0.17}_{-0.15}$, $z_q=3.22$, log SFR/(M$_\odot$/yr) = $1.88^{+0.30}_{-0.19}$, log M$_\star$/M$_\odot$= $10.59^{+0.10}_{-0.14}$, $E(B-V)=0.30$
catalog, aper2
SPLASH data
own data, aper2
own data, iso
Separation: 0.26"
iso aper2
c1 1.07 0.98
c2 2.81 4.00
P(z), $\chi^2=0.39$, $\chi^2_q=0.48$
OII
NeV
HeI
MgII
NeIV
CII
CIII
magnitude
wavelength [Å]
6.0"
Y
NB118
J
RGB
(H, NB118, Y)
F814W

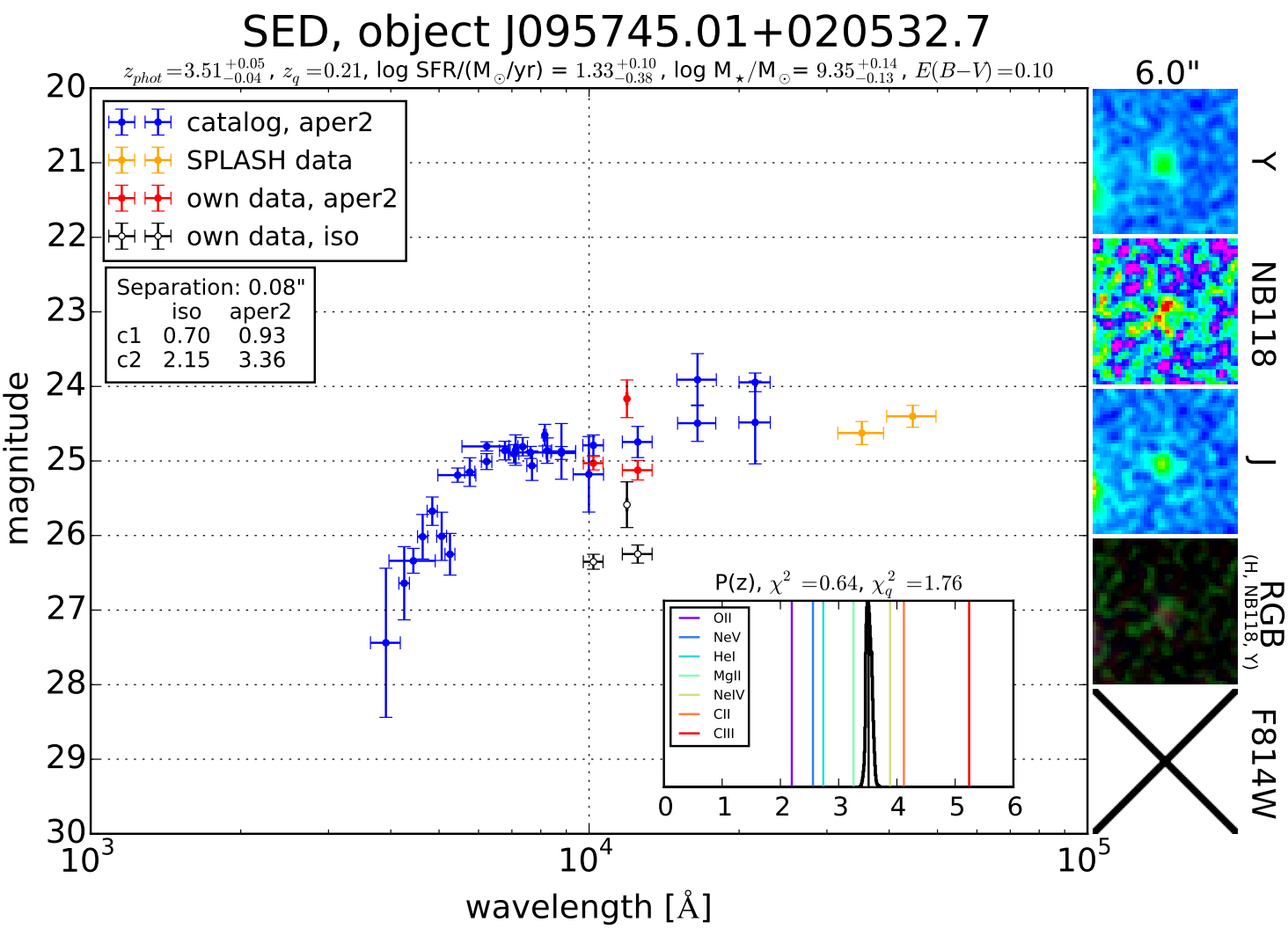
SED, object J095745.01+020532.7
$z_{phot}=3.51^{+0.05}_{-0.04}$, $z_q=0.21$, log SFR/(M$_\odot$/yr) = $1.33^{+0.10}_{-0.38}$, log M$_\star$/M$_\odot$= $9.35^{+0.14}_{-0.13}$, $E(B-V)=0.10$
catalog, aper2
SPLASH data
own data, aper2
own data, iso
Separation: 0.08"
iso aper2
c1 0.70 0.93
c2 2.15 3.36
P(z), $\chi^2=0.64$, $\chi^2_q=1.76$
OII
NeV
HeI
MgII
NeIV
CII
CIII
magnitude
wavelength [Å]
6.0"
Y
NB118
J
RGB
(H, NB118, Y)
F814W

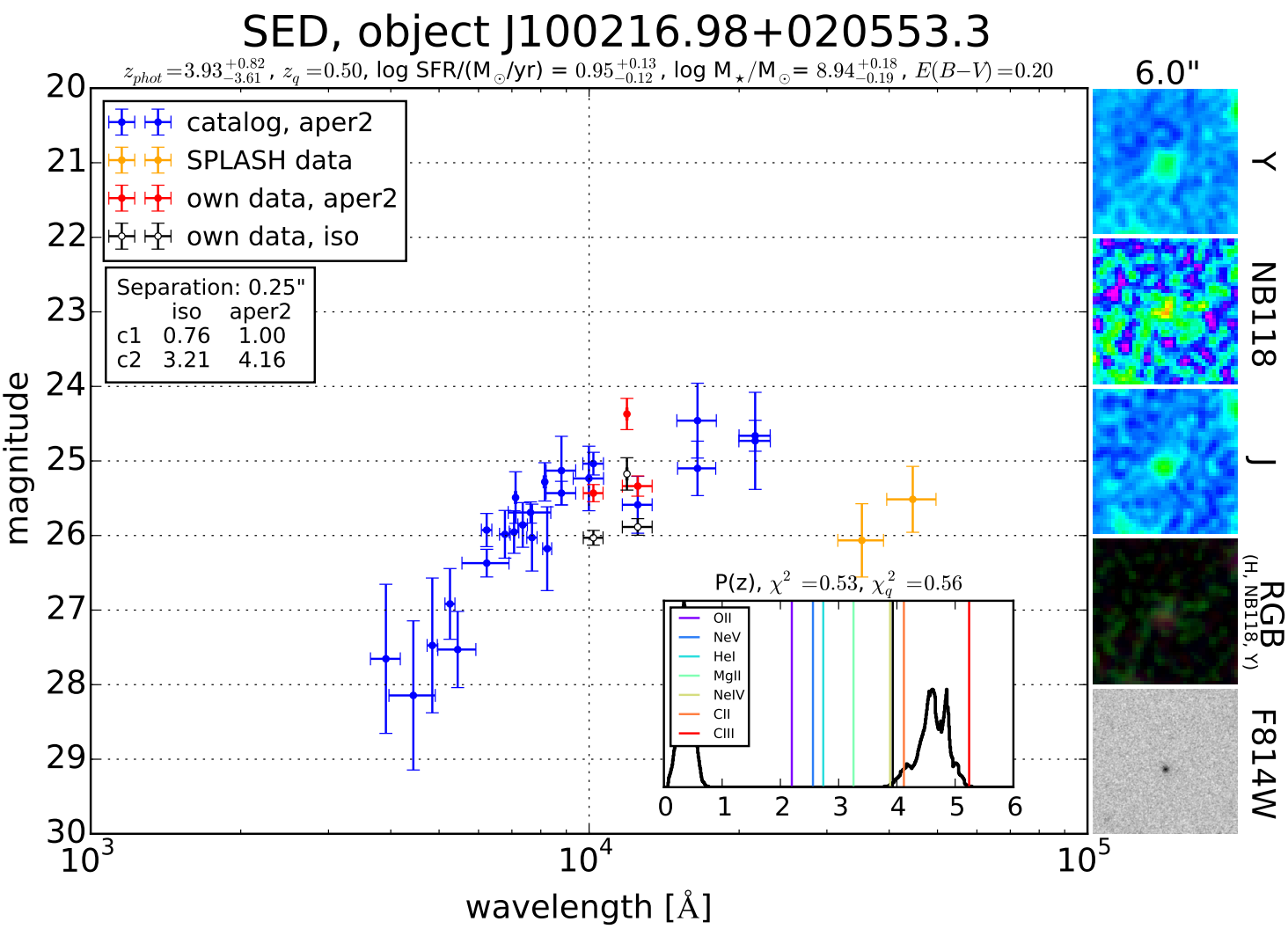
SED, object J100216.98+020553.3
$z_{phot}=3.93^{+0.82}_{-3.61}$, $z_q=0.50$, log SFR/(M$_\odot$/yr) = $0.95^{+0.13}_{-0.12}$, log M$_\star$/M$_\odot$= $8.94^{+0.18}_{-0.19}$, $E(B-V)=0.20$
catalog, aper2
SPLASH data
own data, aper2
own data, iso
Separation: 0.25"
iso aper2
c1 0.76 1.00
c2 3.21 4.16
P(z), $\chi^2=0.53$; $\chi^2_q=0.56$
OII
NeV
HeI
MgII
NeIV
CII
CIII
magnitude
wavelength [Å]
6.0"
Y
NB118
J
RGB
(H, NB118, Y)
F814W

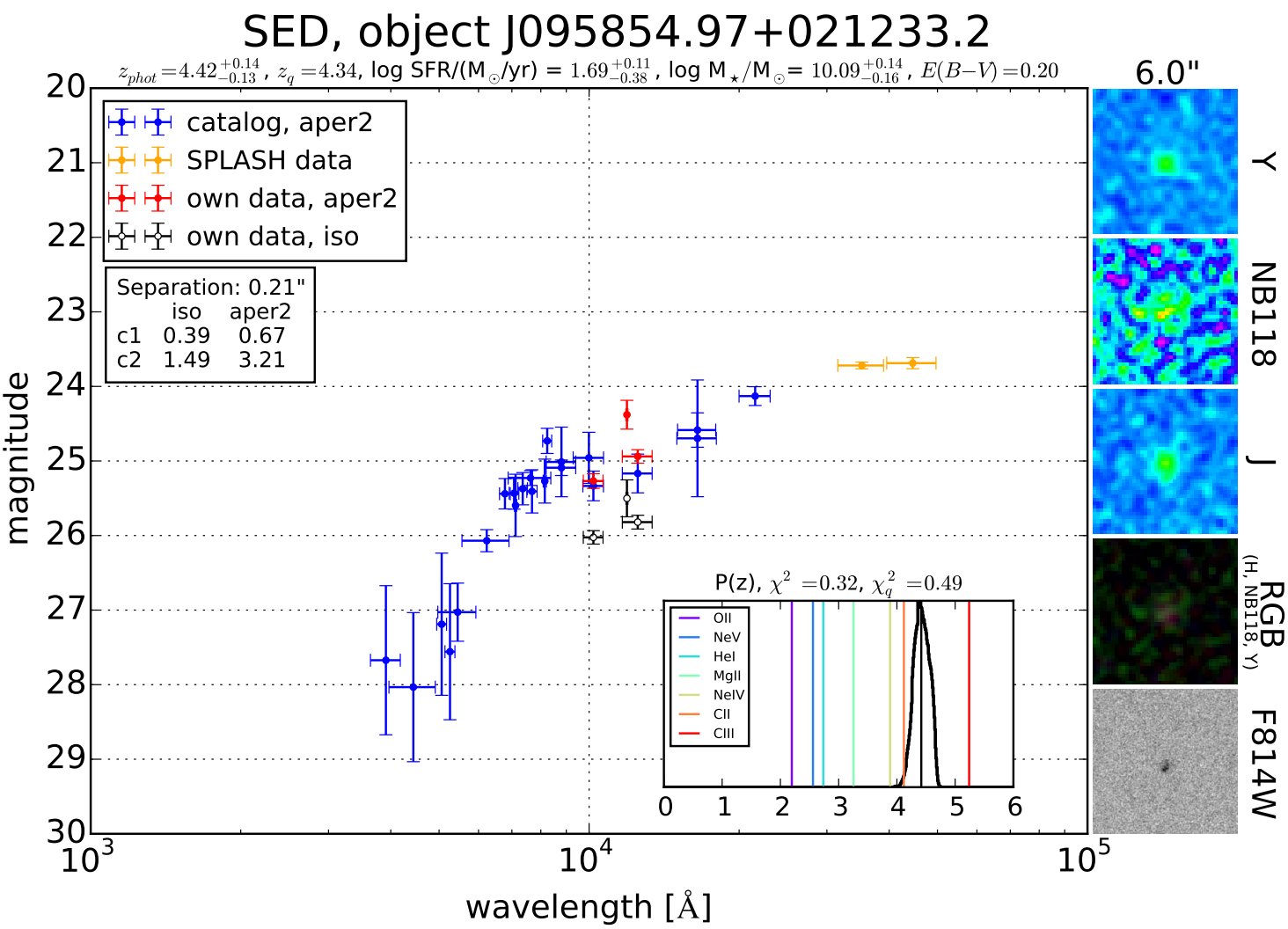
SED, object J095854.97+021233.2
$z_{phot}=4.42^{+0.14}_{-0.13}$, $z_q=4.34$, log SFR/(M$_\odot$/yr) = $1.69^{+0.11}_{-0.38}$, log M$_\star$/M$_\odot$= $10.09^{+0.14}_{-0.16}$, $E(B-V)=0.20$
catalog, aper2
SPLASH data
own data, aper2
own data, iso
Separation: 0.21"
iso aper2
c1 0.39 0.67
c2 1.49 3.21
P(z), $\chi^2=0.32$, $\chi^2_q=0.49$
OII
NeV
HeI
MgII
NeIV
CII
CIII
magnitude
wavelength [Å]
6.0"
Y
NB118
J
RGB
(H, NB118, Y)
F814W

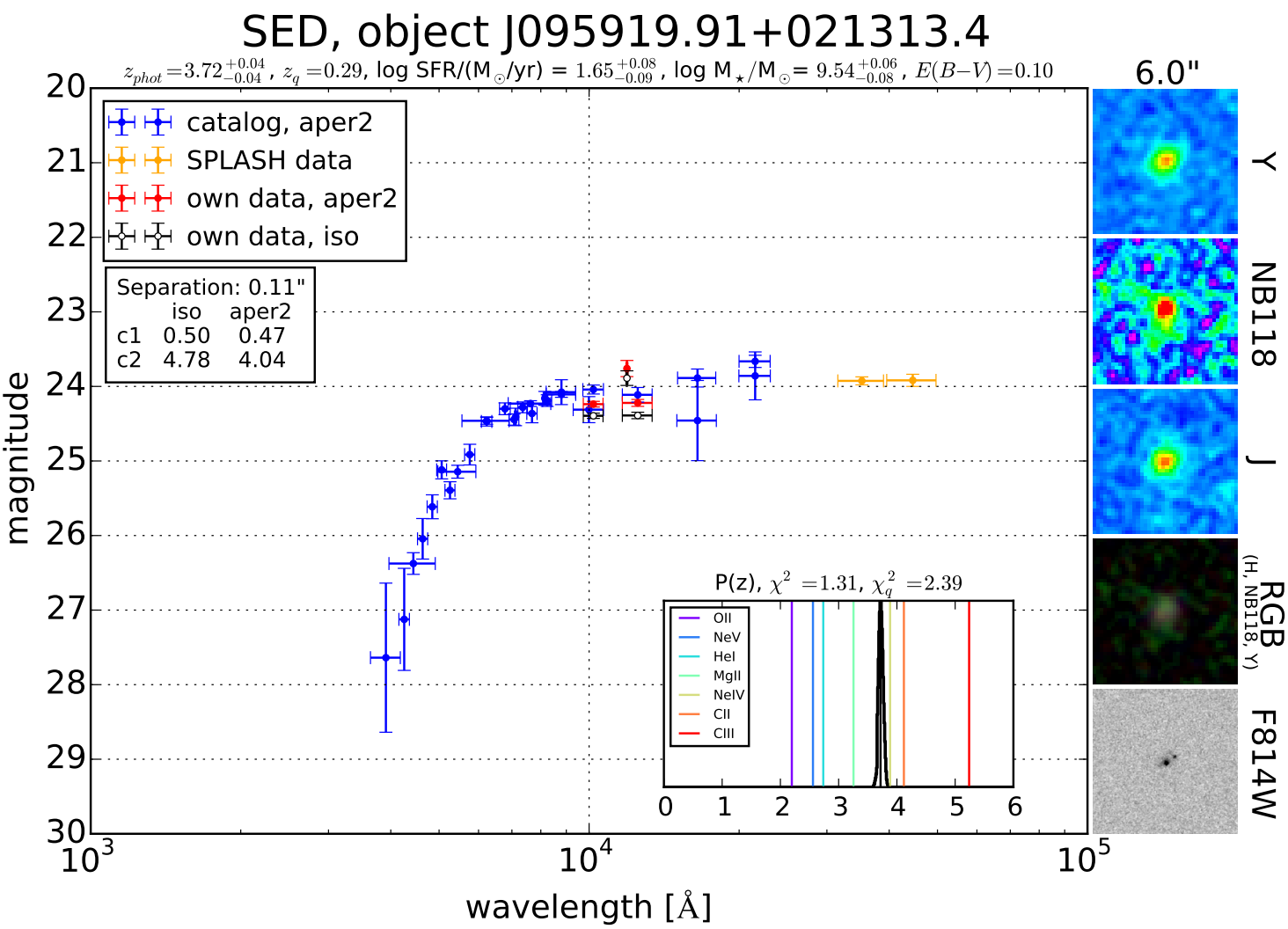
SED, object J095919.91+021313.4
$z_{phot}=3.72^{+0.04}_{-0.04}$, $z_q=0.29$, log SFR/(M$_\odot$/yr) = $1.65^{+0.08}_{-0.09}$, log M$_\star$/M$_\odot$= $9.54^{+0.06}_{-0.08}$, $E(B-V)=0.10$
catalog, aper2
SPLASH data
own data, aper2
own data, iso
Separation: 0.11"
iso aper2
c1 0.50 0.47
c2 4.78 4.04
P(z), $\chi^2=1.31$, $\chi^2_q=2.39$
OII
NeV
HeI
MgII
NeIV
CII
CIII
magnitude
wavelength [Å]
6.0"
Y
NB118
J
RGB
(H, NB118, Y)
F814W

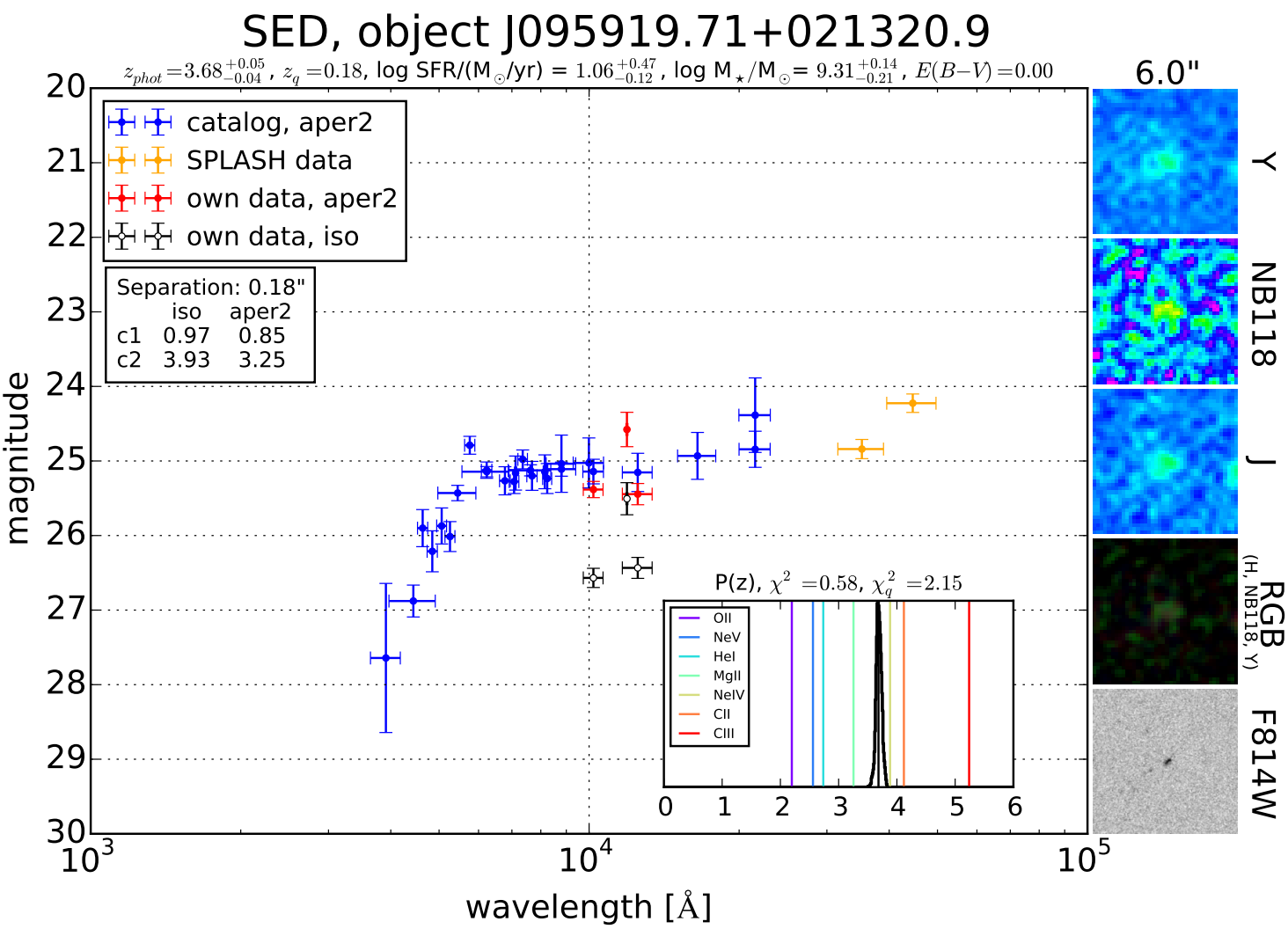
SED, object J095919.71+021320.9
$z_{phot}=3.68^{+0.05}_{-0.04}$, $z_q=0.18$, log SFR/(M$_\odot$/yr) = $1.06^{+0.47}_{-0.12}$, log M$_\star$/M$_\odot$= $9.31^{+0.14}_{-0.21}$, $E(B-V)=0.00$
catalog, aper2
SPLASH data
own data, aper2
own data, iso
Separation: 0.18"
iso aper2
c1 0.97 0.85
c2 3.93 3.25
P(z), $\chi^2=0.58$, $\chi^2_q=2.15$
OII
NeV
HeI
MgII
NeIV
CII
CIII
magnitude
wavelength [Å]
6.0"
Y
NB118
J
RGB
(H, NB118, Y)
F814W

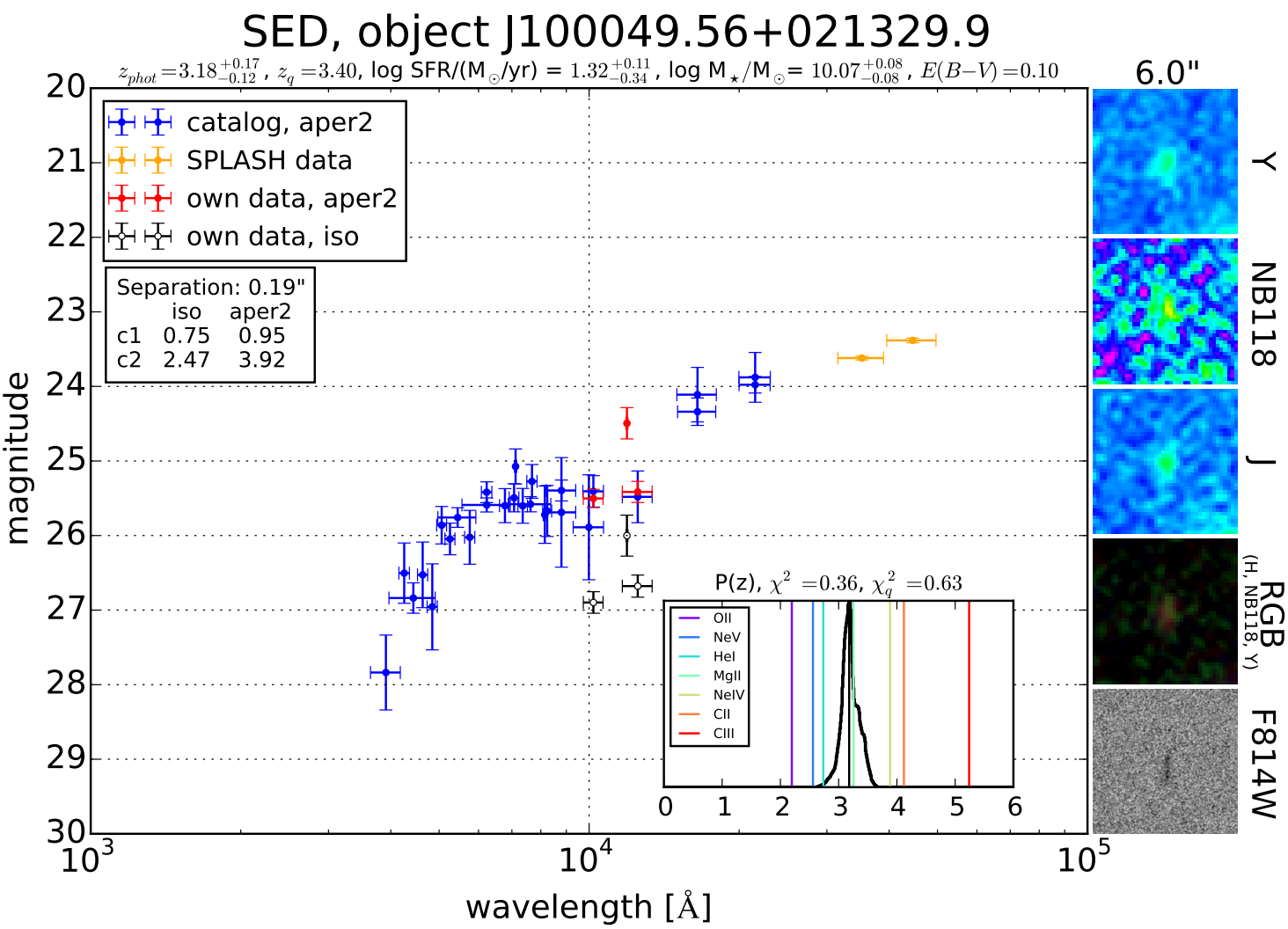
SED, object J100049.56+021329.9
$z_{phot}=3.18^{+0.17}_{-0.12}$, $z_q=3.40$, log SFR/(M$_\odot$/yr) = $1.32^{+0.11}_{-0.34}$, log M$_\star$/M$_\odot$= $10.07^{+0.08}_{-0.08}$, $E(B-V)=0.10$
6.0"
catalog, aper2
SPLASH data
own data, aper2
own data, iso
Separation: 0.19"
iso aper2
c1 0.75 0.95
c2 2.47 3.92
P(z), $\chi^2=0.36$, $\chi^2_q=0.63$
OII
NeV
HeI
MgII
NeIV
CII
CIII
magnitude
wavelength [Å]
Y
NB118
J
RGB
(H, NB118, Y)
F814W

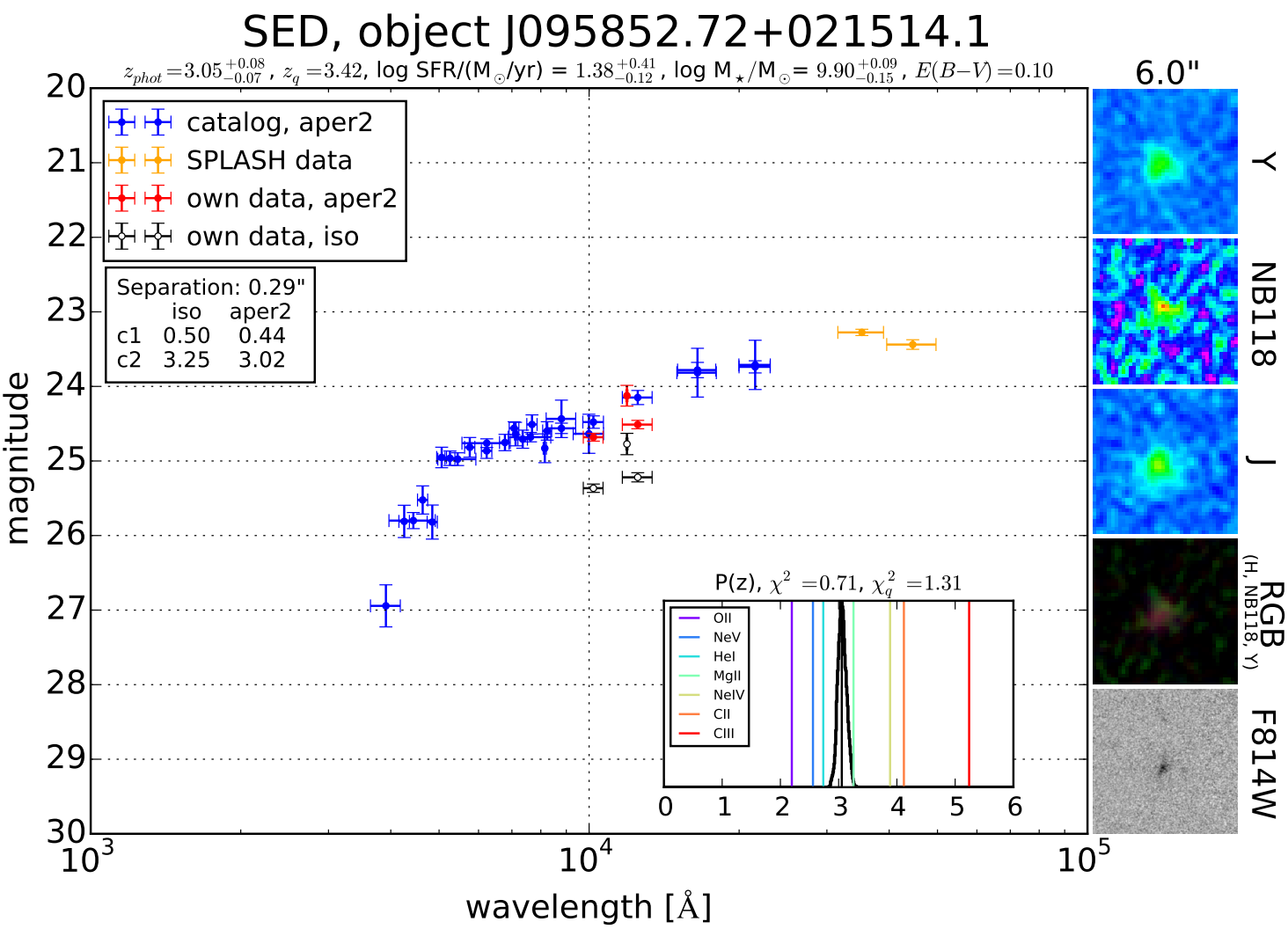
SED, object J095852.72+021514.1
$z_{phot}=3.05^{+0.08}_{-0.07}$, $z_q=3.42$, log SFR/(M$_\odot$/yr) = $1.38^{+0.41}_{-0.12}$, log M$_\star$/M$_\odot$= $9.90^{+0.09}_{-0.15}$, $E(B-V)=0.10$
catalog, aper2
SPLASH data
own data, aper2
own data, iso
Separation: 0.29"
iso aper2
c1 0.50 0.44
c2 3.25 3.02
P(z), $\chi^2=0.71$, $\chi^2_q=1.31$
OII
NeV
HeI
MgII
NeIV
CII
CIII
magnitude
wavelength [Å]
6.0"
Y
NB118
J
RGB
(H, NB118, Y)
F814W

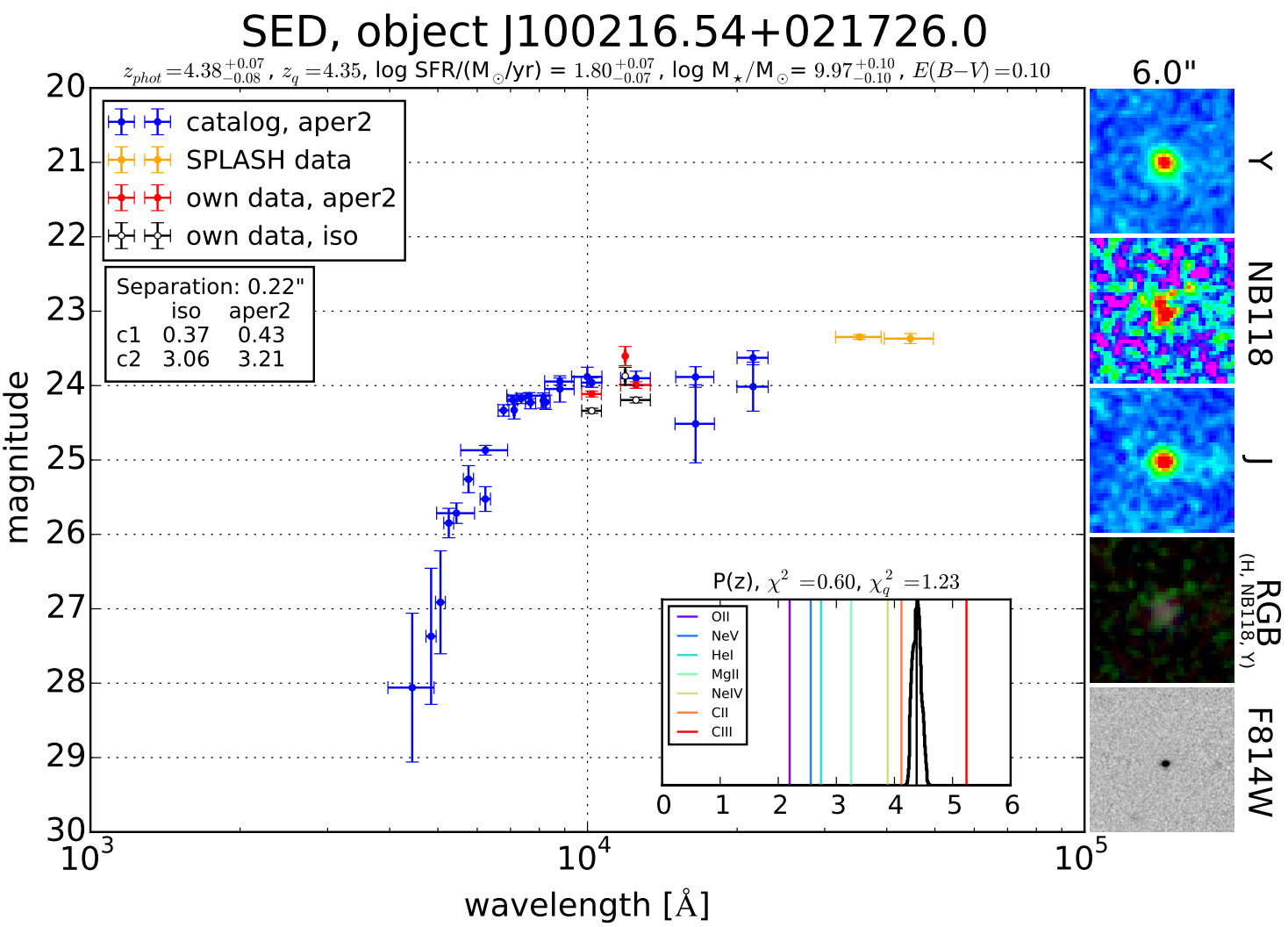
SED, object J100216.54+021726.0
$z_{phot}=4.38^{+0.07}_{-0.08}$, $z_q=4.35$, log SFR/(M$_\odot$/yr) = $1.80^{+0.07}_{-0.07}$, log M$_\star$/M$_\odot$= $9.97^{+0.10}_{-0.10}$, $E(B-V)=0.10$
catalog, aper2
SPLASH data
own data, aper2
own data, iso
Separation: 0.22"
iso aper2
c1 0.37 0.43
c2 3.06 3.21
P(z), $\chi^2=0.60$, $\chi^2_q=1.23$
OII
NeV
HeI
MgII
NeIV
CII
CIII
magnitude
wavelength [Å]
6.0"
Y
NB118
J
RGB
(H, NB118, Y)
F814W

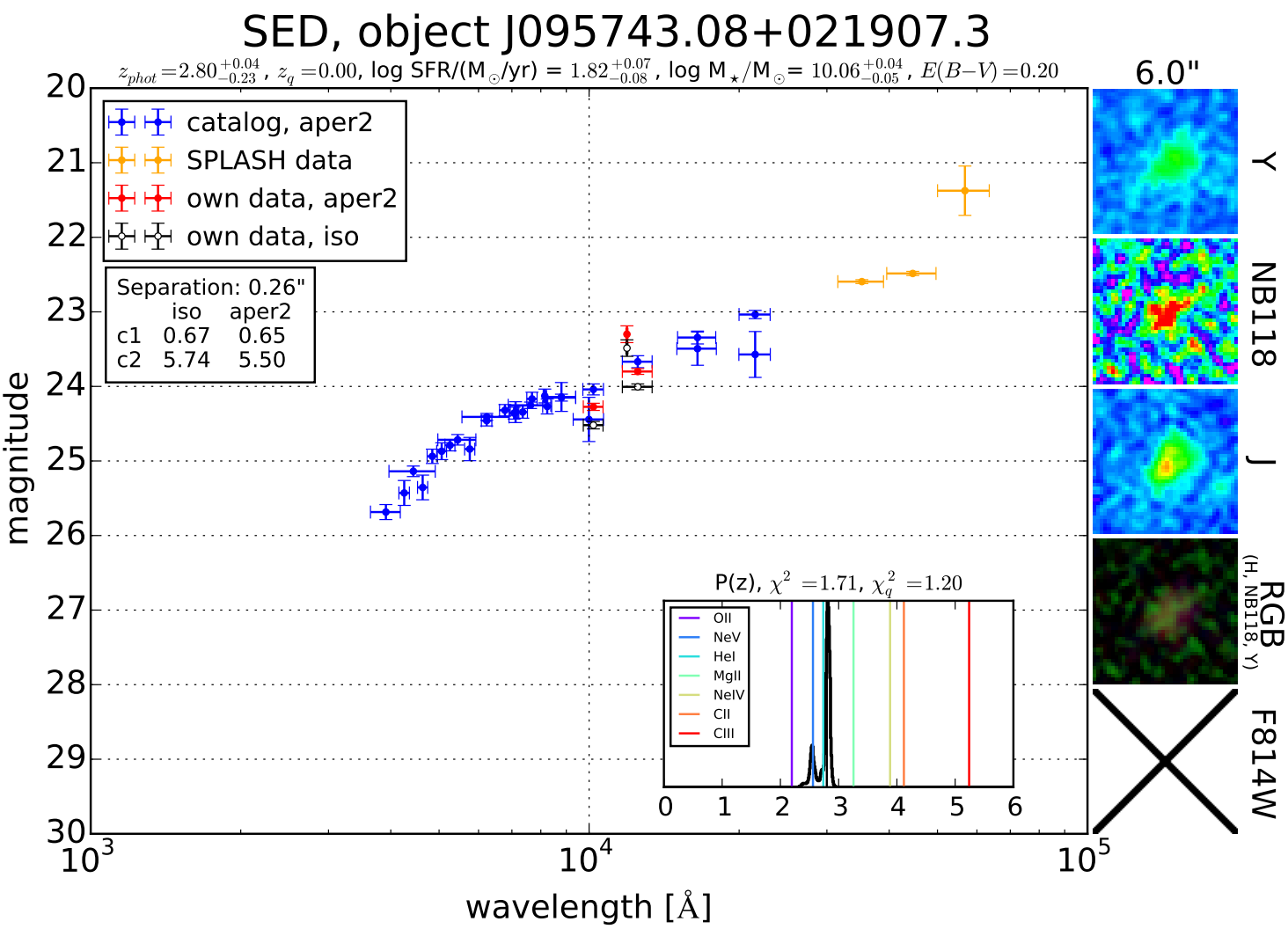
SED, object J095743.08+021907.3
$z_{phot}=2.80^{+0.04}_{-0.23}$, $z_q=0.00$, log SFR/(M$_\odot$/yr) = $1.82^{+0.07}_{-0.08}$, log M$_\star$/M$_\odot$= $10.06^{+0.04}_{-0.05}$, $E(B-V)=0.20$
catalog, aper2
SPLASH data
own data, aper2
own data, iso
Separation: 0.26"
iso aper2
c1 0.67 0.65
c2 5.74 5.50
P(z), $\chi^2=1.71$, $\chi^2_q=1.20$
OII
NeV
HeI
MgII
NeIV
CII
CIII
magnitude
wavelength [Å]
6.0"
Y
NB118
J
RGB
(H, NB118, Y)
F814W

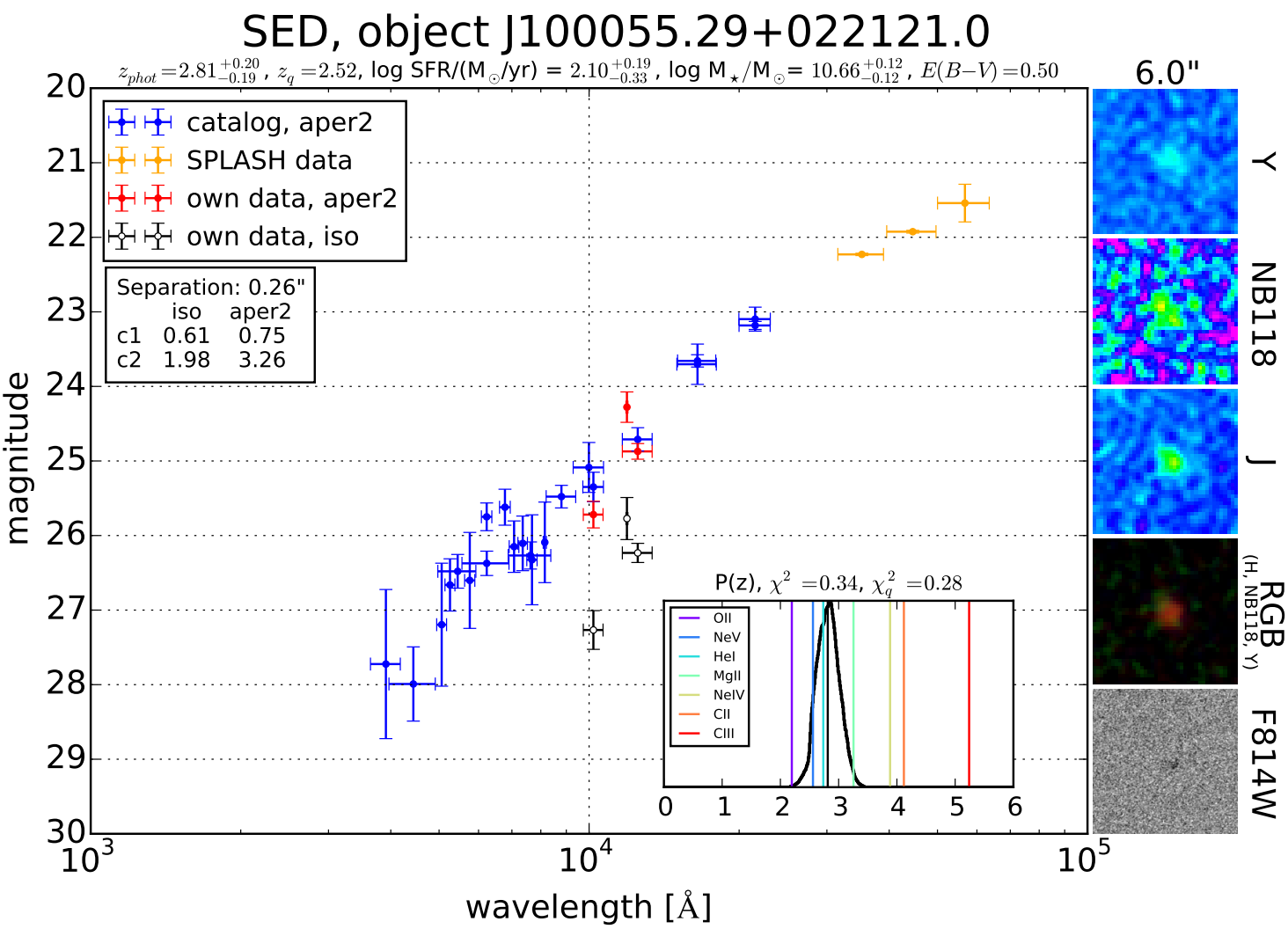
SED, object J100055.29+022121.0
$z_{phot}=2.81^{+0.20}_{-0.19}$, $z_q=2.52$, log SFR/(M$_\odot$/yr) = $2.10^{+0.19}_{-0.33}$, log M$_\star$/M$_\odot$= $10.66^{+0.12}_{-0.12}$, $E(B-V)=0.50$
catalog, aper2
SPLASH data
own data, aper2
own data, iso
Separation: 0.26"
iso aper2
c1 0.61 0.75
c2 1.98 3.26
P(z), $\chi^2=0.34$, $\chi^2_q=0.28$
OII
NeV
HeI
MgII
NeIV
CII
CIII
magnitude
wavelength [Å]
6.0"
Y
NB118
J
RGB
(H, NB118, Y)
F814W

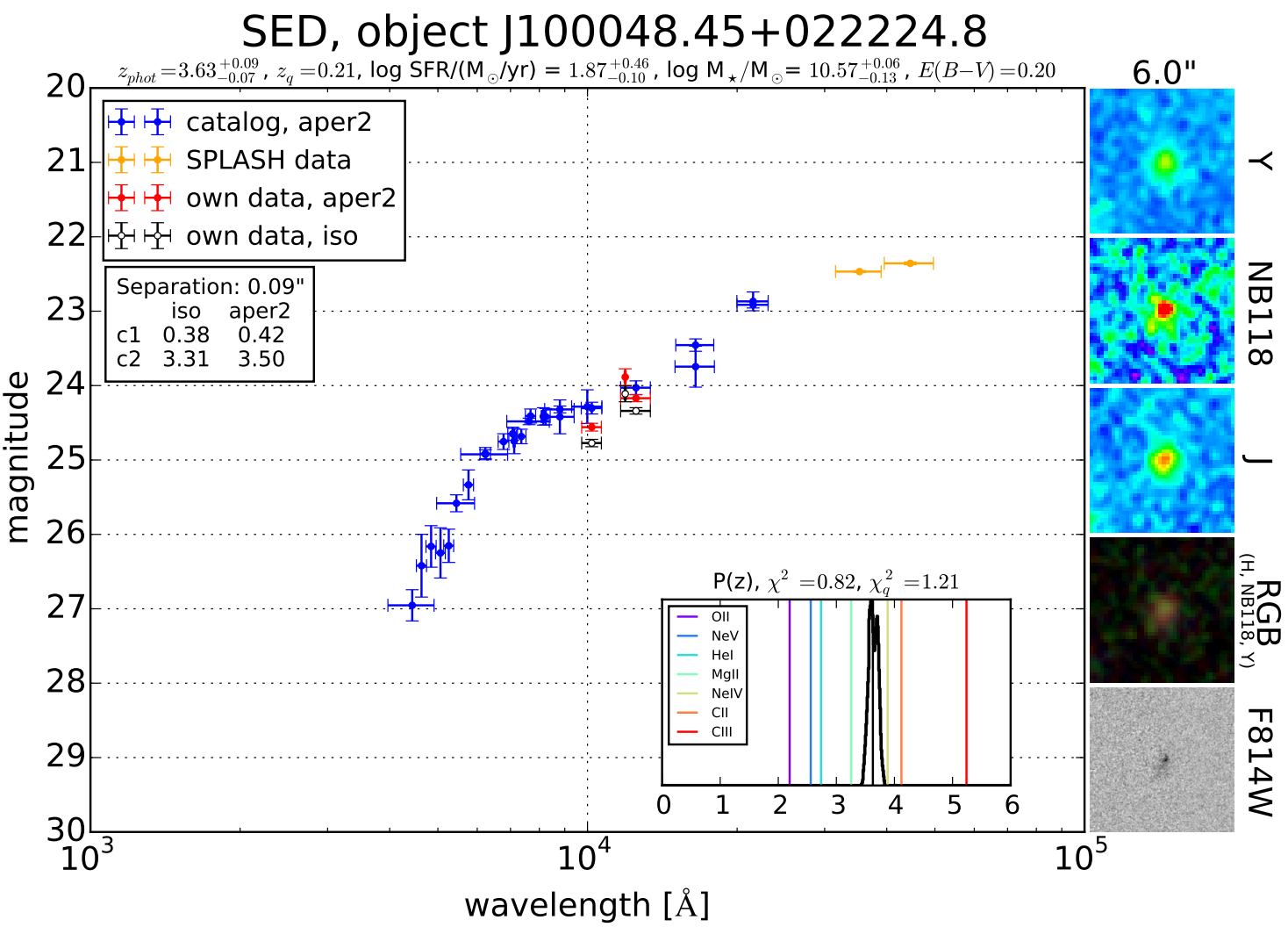
SED, object J100048.45+022224.8
$z_{phot}=3.63^{+0.09}_{-0.07}$, $z_q=0.21$, log SFR/(M$_\odot$/yr) = $1.87^{+0.46}_{-0.10}$, log M$_\star$/M$_\odot$= $10.57^{+0.06}_{-0.13}$, $E(B-V)=0.20$
catalog, aper2
SPLASH data
own data, aper2
own data, iso
Separation: 0.09"
iso aper2
c1 0.38 0.42
c2 3.31 3.50
P(z), $\chi^2=0.82$, $\chi^2_q=1.21$
OII
NeV
HeI
MgII
NeIV
CII
CIII
magnitude
wavelength [Å]
6.0"
Y
NB118
J
RGB
(H, NB118, Y)
F814W

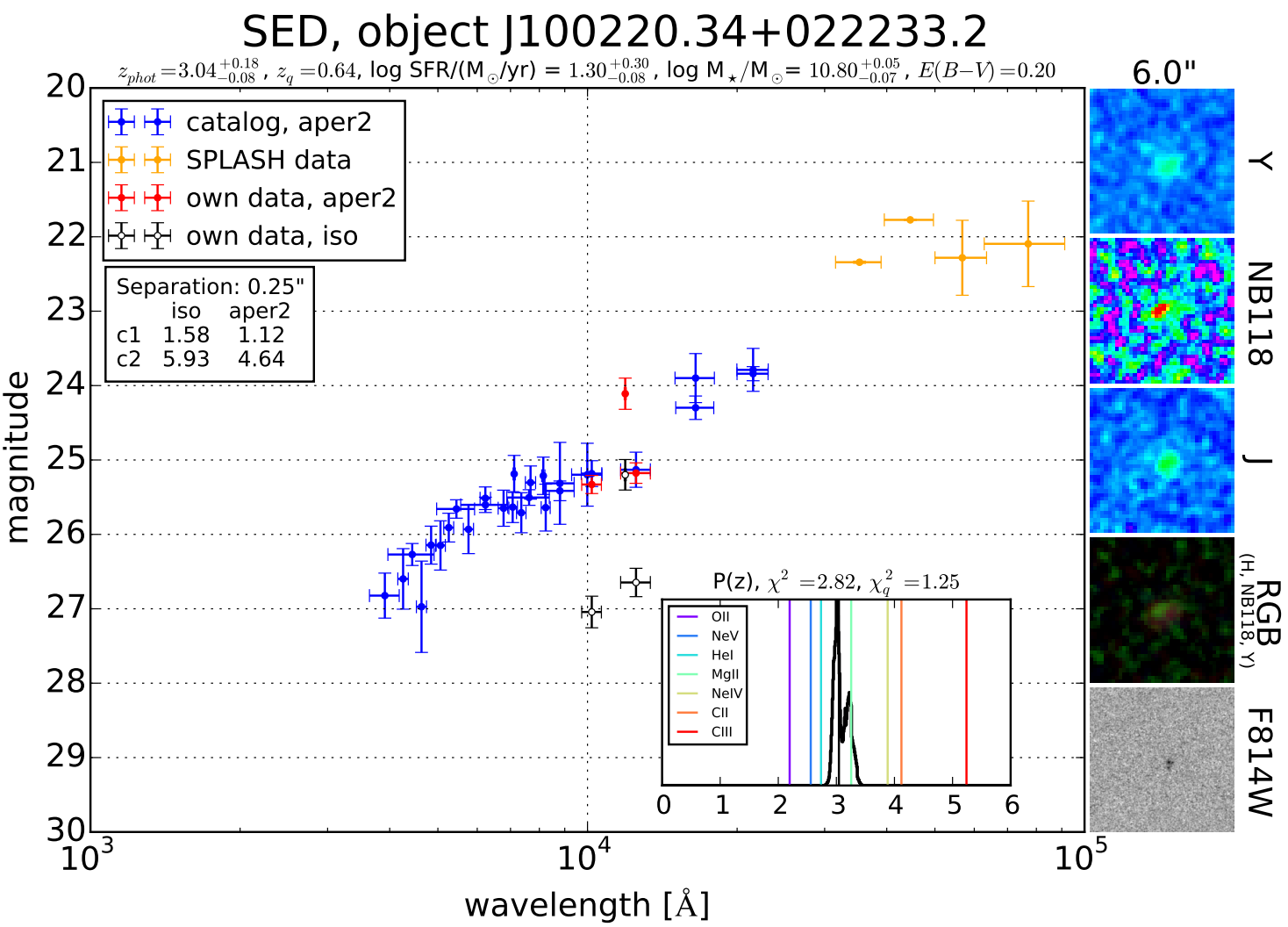
SED, object J100220.34+022233.2
$z_{phot}=3.04^{+0.18}_{-0.08}$, $z_q=0.64$, log SFR/(M$_\odot$/yr) = $1.30^{+0.30}_{-0.08}$, log M$_\star$/M$_\odot$= $10.80^{+0.05}_{-0.07}$, $E(B-V)=0.20$
catalog, aper2
SPLASH data
own data, aper2
own data, iso
Separation: 0.25"
iso aper2
c1 1.58 1.12
c2 5.93 4.64
P(z), $\chi^2=2.82$, $\chi^2_q=1.25$
OII
NeV
HeI
MgII
NeIV
CII
CIII
magnitude
wavelength [Å]
6.0"
Y
NB118
J
RGB
(H, NB118, Y)
F814W

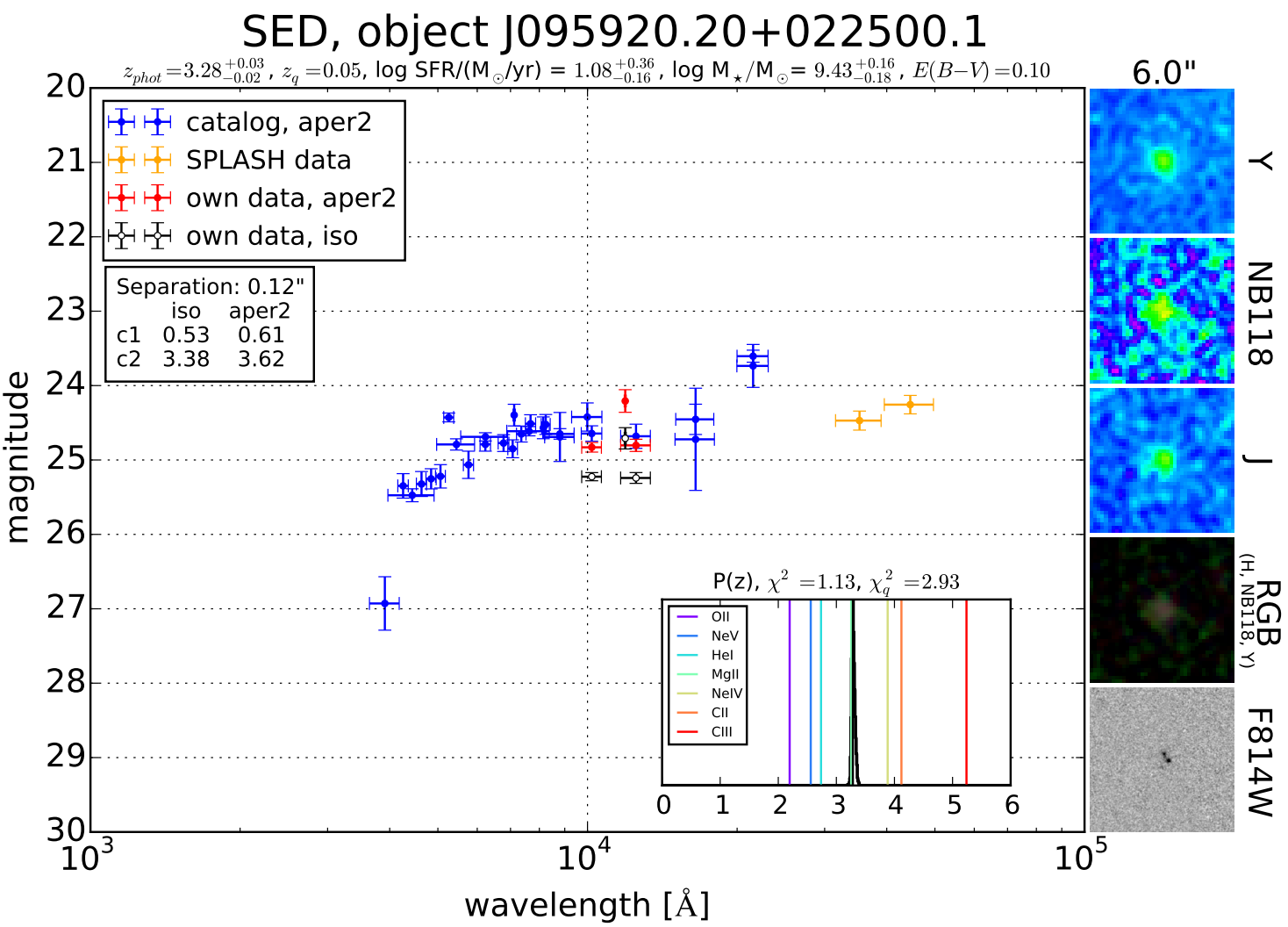
SED, object J095920.20+022500.1
$z_{phot}=3.28^{+0.03}_{-0.02}$, $z_q=0.05$, log SFR/(M$_\odot$/yr) = $1.08^{+0.36}_{-0.16}$, log M$_\star$/M$_\odot$= $9.43^{+0.16}_{-0.18}$, $E(B-V)=0.10$
catalog, aper2
SPLASH data
own data, aper2
own data, iso
Separation: 0.12"
iso aper2
c1 0.53 0.61
c2 3.38 3.62
P(z), $\chi^2=1.13$, $\chi^2_q=2.93$
OII
NeV
HeI
MgII
NeIV
CII
CIII
magnitude
wavelength [Å]
6.0"
Y
NB118
J
RGB
(H, NB118, Y)
F814W

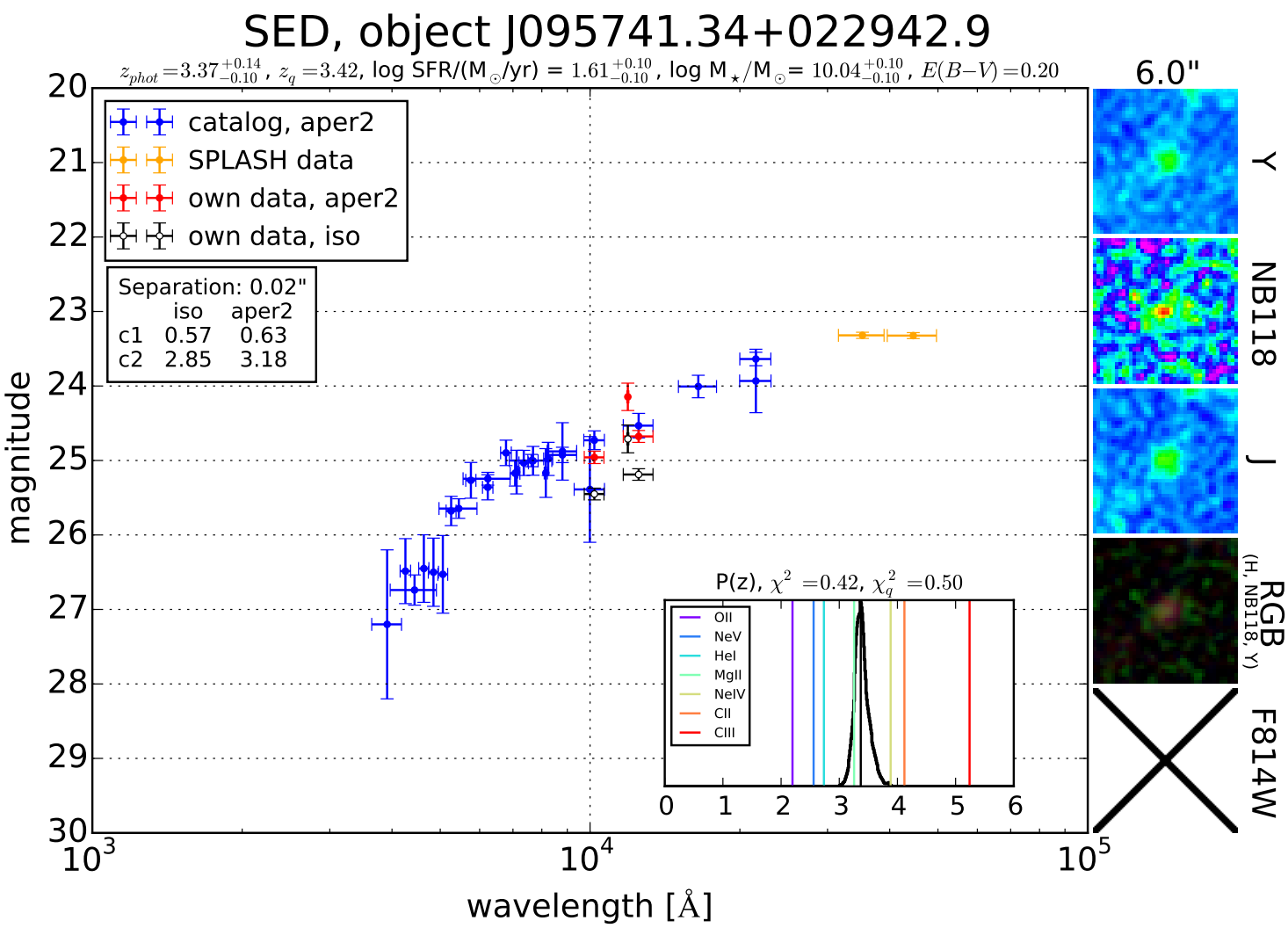
SED, object J095741.34+022942.9
$z_{phot}=3.37^{+0.14}_{-0.10}$, $z_q=3.42$, log SFR/(M$_\odot$/yr) = $1.61^{+0.10}_{-0.10}$, log M$_\star$/M$_\odot$= $10.04^{+0.10}_{-0.10}$, $E(B-V)=0.20$
catalog, aper2
SPLASH data
own data, aper2
own data, iso
Separation: 0.02"
iso aper2
c1 0.57 0.63
c2 2.85 3.18
P(z), $\chi^2=0.42$, $\chi^2_q=0.50$
OII
NeV
HeI
MgII
NeIV
CII
CIII
magnitude
wavelength [Å]
6.0"
Y
NB118
J
RGB
(H, NB118, Y)
F814W

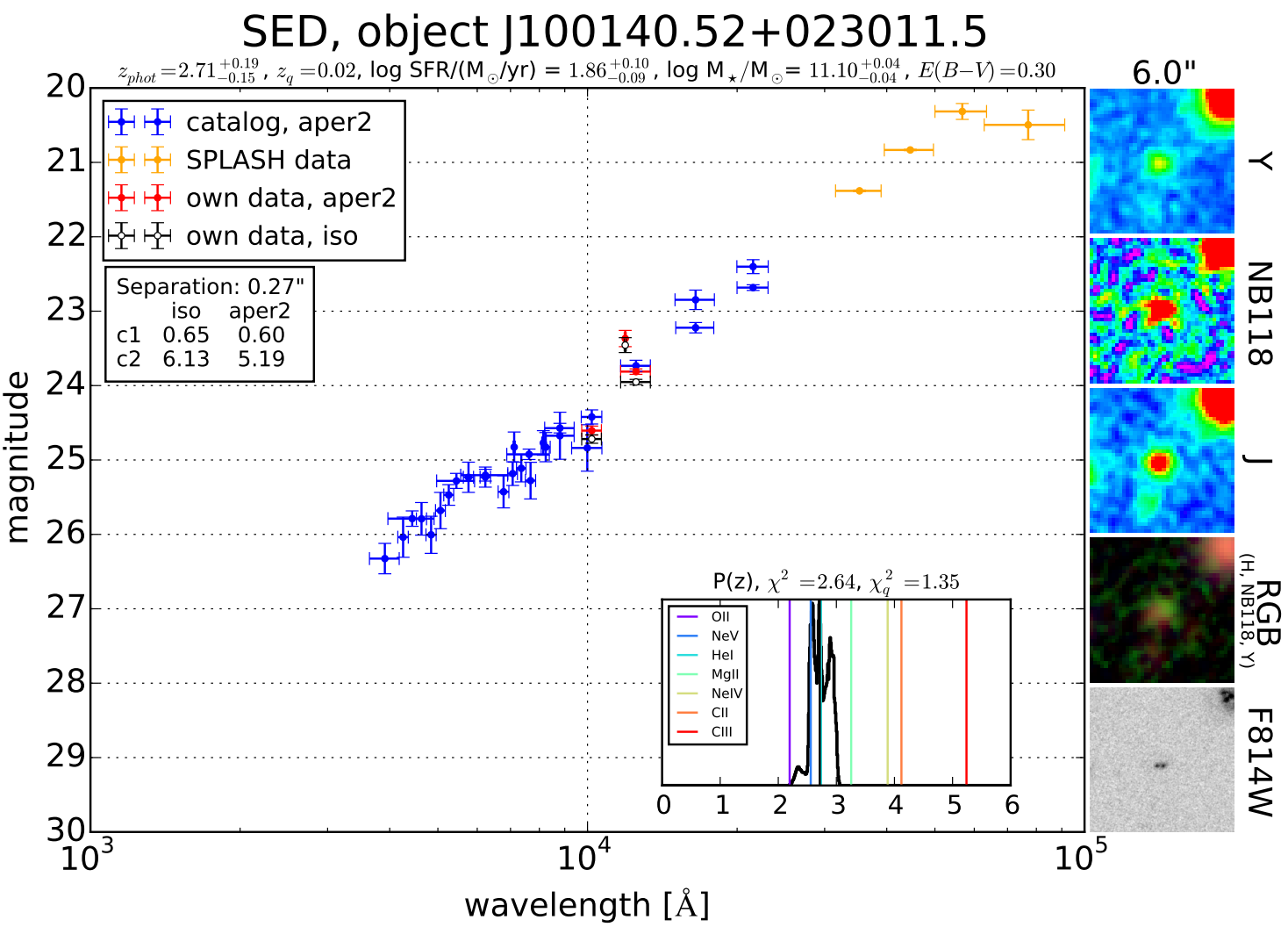
SED, object J100140.52+023011.5
$z_{phot}=2.71^{+0.19}_{-0.15}$, $z_q=0.02$, log SFR/(M$_\odot$/yr) = $1.86^{+0.10}_{-0.09}$, log M$_\star$/M$_\odot$= $11.10^{+0.04}_{-0.04}$, $E(B-V)=0.30$
catalog, aper2
SPLASH data
own data, aper2
own data, iso
Separation: 0.27"
iso aper2
c1 0.65 0.60
c2 6.13 5.19
P(z), $\chi^2=2.64$, $\chi^2_q=1.35$
OII
NeV
HeI
MgII
NeIV
CII
CIII
magnitude
wavelength [Å]
6.0"
Y
NB118
J
RGB
(H, NB118, Y)
F814W

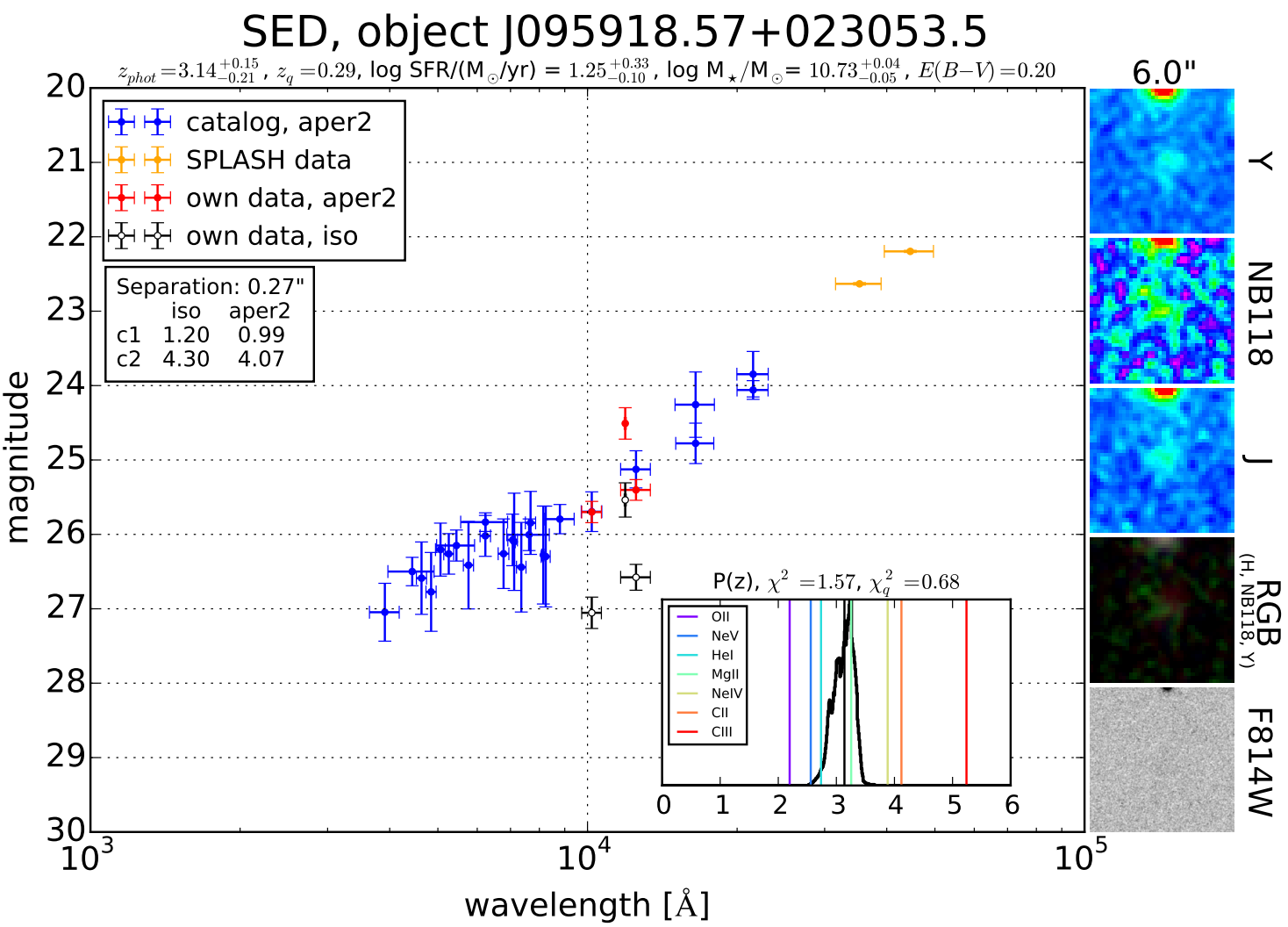
SED, object J095918.57+023053.5
$z_{phot}=3.14^{+0.15}_{-0.21}$, $z_q=0.29$, log SFR/(M$_\odot$/yr) = $1.25^{+0.33}_{-0.10}$, log M$_\star$/M$_\odot$= $10.73^{+0.04}_{-0.05}$, $E(B-V)=0.20$
catalog, aper2
SPLASH data
own data, aper2
own data, iso
Separation: 0.27"
iso aper2
c1 1.20 0.99
c2 4.30 4.07
P(z), $\chi^2=1.57$, $\chi^2_q=0.68$
OII
NeV
HeI
MgII
NeIV
CII
CIII
magnitude
wavelength [Å]
6.0"
Y
NB118
J
RGB
(H, NB118, Y)
F814W

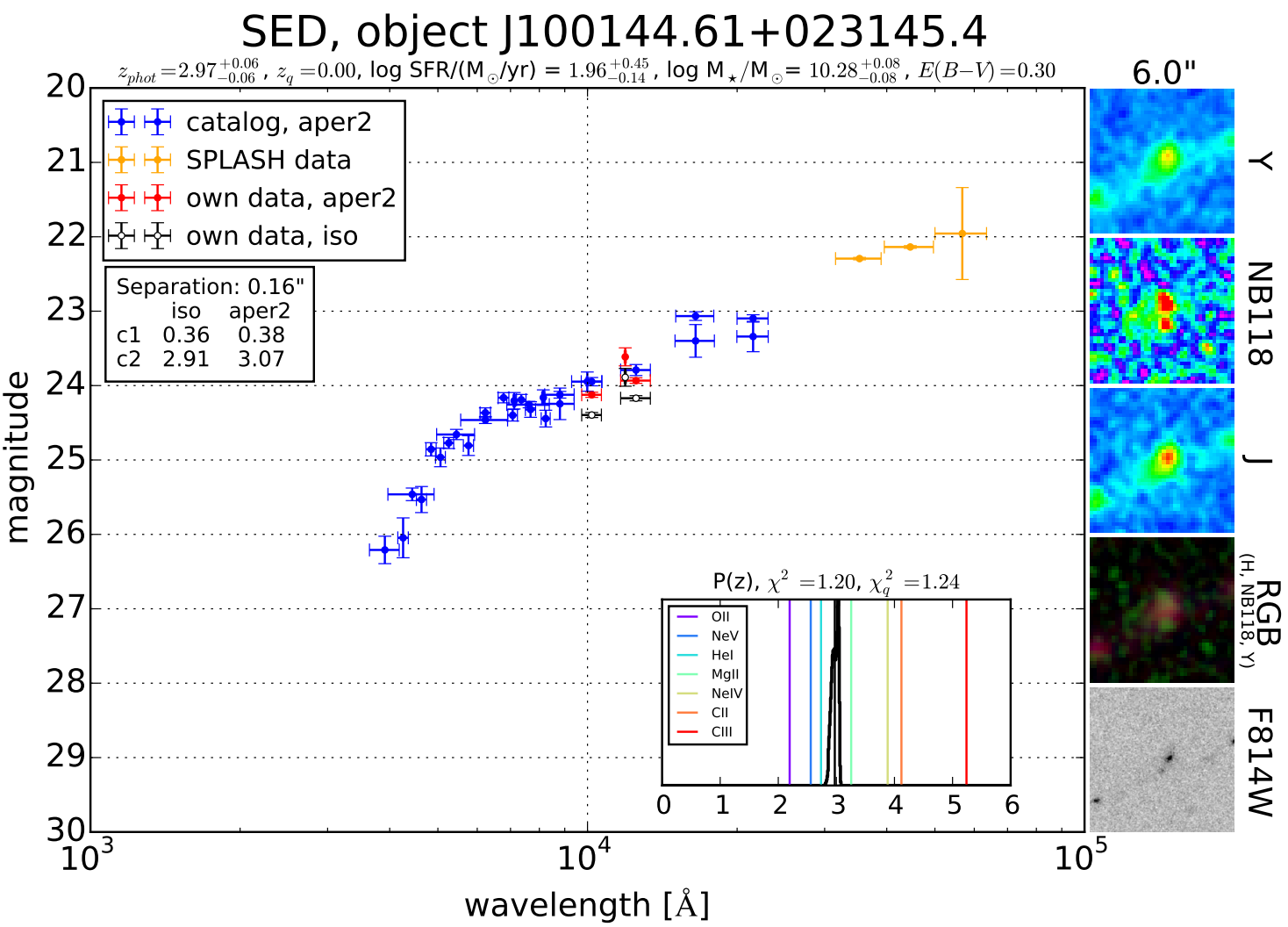
SED, object J100144.61+023145.4
$z_{phot}=2.97^{+0.06}_{-0.06}$, $z_q=0.00$, log SFR/(M$_\odot$/yr) = $1.96^{+0.45}_{-0.14}$, log M$_\star$/M$_\odot$= $10.28^{+0.08}_{-0.08}$, $E(B-V)=0.30$
catalog, aper2
SPLASH data
own data, aper2
own data, iso
Separation: 0.16"
iso aper2
c1 0.36 0.38
c2 2.91 3.07
P(z), $\chi^2=1.20$, $\chi^2_q=1.24$
OII
NeV
HeI
MgII
NeIV
CII
CIII
magnitude
wavelength [Å]
6.0"
Y
NB118
J
RGB
(H, NB118, Y)
F814W

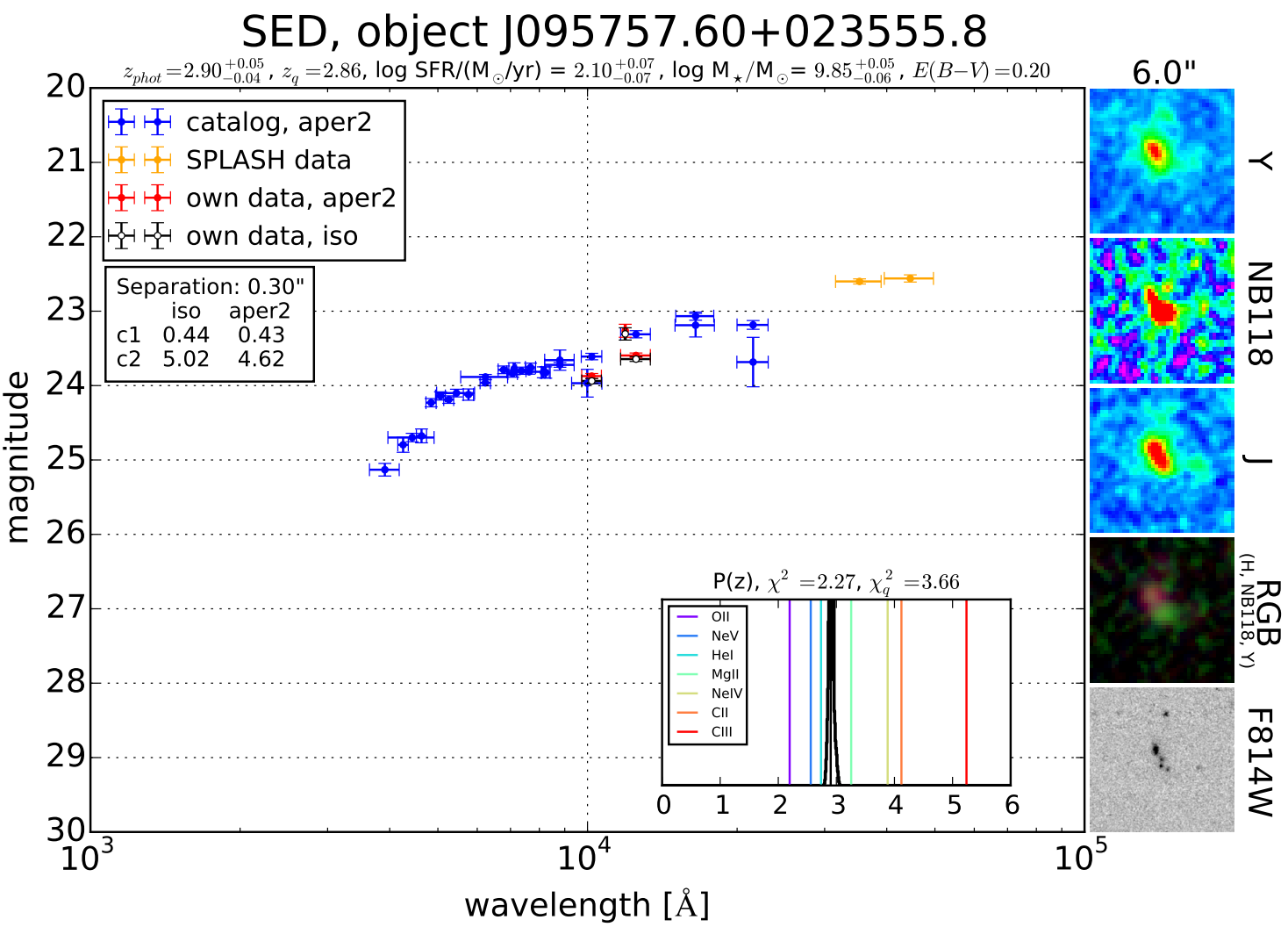
SED, object J095757.60+023555.8
$z_{phot}=2.90^{+0.05}_{-0.04}$, $z_q=2.86$, log SFR/(M$_\odot$/yr) = $2.10^{+0.07}_{-0.07}$, log M$_\star$/M$_\odot$= $9.85^{+0.05}_{-0.06}$, $E(B-V)=0.20$
catalog, aper2
SPLASH data
own data, aper2
own data, iso
Separation: 0.30"
iso aper2
c1 0.44 0.43
c2 5.02 4.62
P(z), $\chi^2=2.27$, $\chi^2_q=3.66$
OII
NeV
HeI
MgII
NeIV
CII
CIII
magnitude
wavelength [Å]
6.0"
Y
NB118
J
RGB
(H, NB118, Y)
F814W

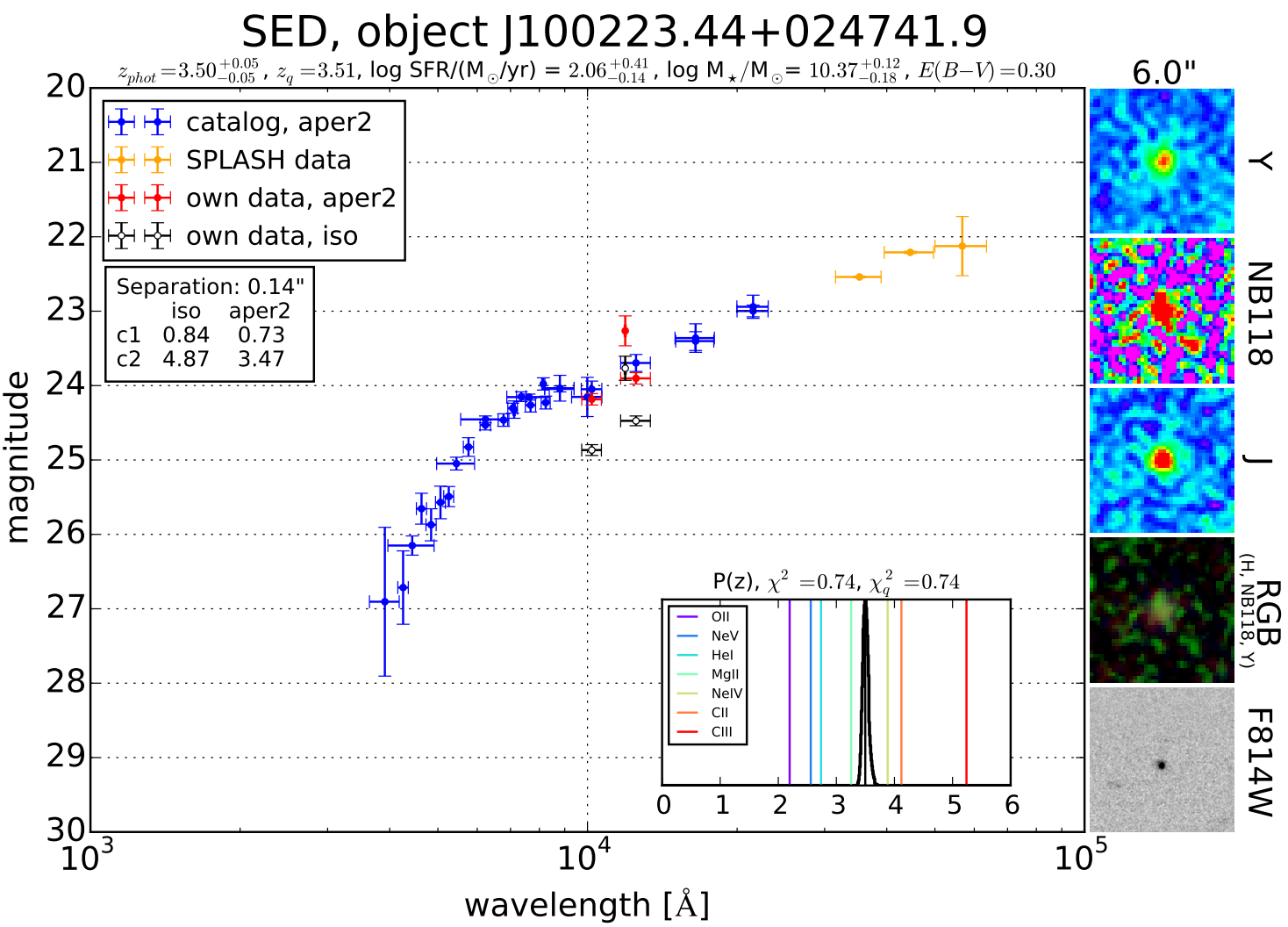
SED, object J100223.44+024741.9
$z_{phot}=3.50^{+0.05}_{-0.05}$, $z_q=3.51$, log SFR/(M$_\odot$/yr) = $2.06^{+0.41}_{-0.14}$, log M$_\star$/M$_\odot$= $10.37^{+0.12}_{-0.18}$, $E(B-V)=0.30$
catalog, aper2
SPLASH data
own data, aper2
own data, iso
Separation: 0.14"
iso aper2
c1 0.84 0.73
c2 4.87 3.47
P(z), $\chi^2=0.74$, $\chi^2_q=0.74$
OII
NeV
HeI
MgII
NeIV
CII
CIII
magnitude
wavelength [Å]
6.0"
Y
NB118
J
RGB
(H, NB118, Y)
F814W

Bibliography

Almeida, C. R., C. N. Tadhunter, K. J. Inskip, R. Morganti, J. Holt, and D. Dicken (2011). The optical morphologies of the 2 jy sample of radio galaxies: evidence for galaxy interactions. *Monthly Notices of the Royal Astronomical Society 410*(3), 1550–1576.

Arnouts, S., L. Moscardini, E. Vanzella, S. Colombi, S. Cristiani, A. Fontana, E. Giallongo, S. Matarrese, and P. Saracco (2002, January). Measuring the redshift evolution of clustering: the Hubble Deep Field South. *MNRAS 329*, 355–366.

Bastian, N., K. R. Covey, and M. R. Meyer (2010, September). A Universal Stellar Initial Mass Function? A Critical Look at Variations. *ARAA 48*, 339–389.

Bertin, E. and S. Arnouts (1996, June). SExtractor: Software for source extraction. *AAPS 117*, 393–404.

Bessiere, P. S., C. N. Tadhunter, C. Ramos Almeida, and M. Villar Martín (2012, October). The importance of galaxy interactions in triggering type II quasar activity. *MNRAS 426*, 276–295.

Bower, R. G., A. J. Benson, R. Malbon, J. C. Helly, C. S. Frenk, C. M. Baugh, S. Cole, and C. G. Lacey (2006, August). Breaking the hierarchy of galaxy formation. *MNRAS 370*, 645–655.

Bruzual, G. and S. Charlot (2003, October). Stellar population synthesis at the resolution of 2003. *MNRAS 344*, 1000–1028.

Chabrier, G. (2003, July). Galactic Stellar and Substellar Initial Mass Function. *PASP 115*, 763–795.

Daddi, E., H. Dannerbauer, D. Stern, M. Dickinson, G. Morrison, D. Elbaz, M. Giavalisco, C. Mancini, A. Pope, and H. Spinrad (2009, April). Two Bright Submillimeter Galaxies in a z = 4.05 Protocluster in Goods-North, and Accurate Radio-Infrared Photometric Redshifts. *ApJ 694*, 1517–1538.

Daddi, E., M. Dickinson, G. Morrison, R. Chary, A. Cimatti, D. Elbaz, D. Frayer, A. Renzini, A. Pope, D. M. Alexander, F. E. Bauer, M. Giavalisco, M. Huynh, J. Kurk, and M. Mignoli (2007, November). Multiwavelength Study of Massive Galaxies at z˜2. I. Star Formation and Galaxy Growth. *ApJ 670*, 156–172.

De Breuck, C., H. Röttgering, G. Miley, W. van Breugel, and P. Best (2000, October). A statistical study of emission lines from high redshift radio galaxies. *A&A 362*, 519–543.

Elitzur, M. and L. C. Ho (2009). On the disappearance of the broad-line region in low-luminosity active galactic nuclei. *The Astrophysical Journal Letters 701*(2), L91.

Fang, G., J.-S. Huang, S. P. Willner, X. Kong, T. Wang, Y. Chen, and X. Lin (2014, February). Selection and Mid-infrared Spectroscopy of Ultraluminous Star-forming Galaxies at z ˜ 2. *ApJ 781*, 63.

Fioc, M. and B. Rocca-Volmerange (1997, October). PEGASE: a UV to NIR spectral evolution model of galaxies. Application to the calibration of bright galaxy counts. *A&A 326*, 950–962.

Gilbank, D. G., I. K. Baldry, M. L. Balogh, K. Glazebrook, and R. G. Bower (2010, July). The local star formation rate density: assessing calibrations using [OII], H and UV luminosities. *MNRAS 405*, 2594–2614.

Hopkins, A. M. and J. F. Beacom (2006, November). On the Normalization of the Cosmic Star Formation History. *ApJ 651*, 142–154.

Ilbert, O., S. Arnouts, H. J. McCracken, M. Bolzonella, E. Bertin, O. Le Fèvre, Y. Mellier, G. Zamorani, R. Pellò, A. Iovino, L. Tresse, V. Le Brun, D. Bottini, B. Garilli, D. Maccagni, J. P. Picat, R. Scaramella, M. Scodeggio, G. Vettolani, A. Zanichelli, C. Adami, S. Bardelli, A. Cappi, S. Charlot, P. Ciliegi, T. Contini, O. Cucciati, S. Foucaud, P. Franzetti, I. Gavignaud, L. Guzzo, B. Marano, C. Marinoni, A. Mazure, B. Meneux, R. Merighi, S. Paltani, A. Pollo, L. Pozzetti, M. Radovich, E. Zucca, M. Bondi, A. Bongiorno, G. Busarello, S. de La Torre, L. Gregorini, F. Lamareille, G. Mathez, P. Merluzzi, V. Ripepi, D. Rizzo, and D. Vergani (2006, October). Accurate photometric redshifts for the CFHT legacy survey calibrated using the VIMOS VLT deep survey. *A&A 457*, 841–856.

Ilbert, O., H. J. McCracken, O. Le Fèvre, P. Capak, J. Dunlop, A. Karim, M. A. Renzini, K. Caputi, S. Boissier, S. Arnouts, H. Aussel, J. Comparat, Q. Guo, P. Hudelot, J. Kartaltepe, J. P. Kneib, J. K. Krogager, E. Le Floc'h, S. Lilly, Y. Mellier, B. Milvang-Jensen, T. Moutard, M. Onodera, J. Richard, M. Salvato, D. B. Sanders, N. Scoville, J. D. Silverman, Y. Taniguchi, L. Tasca, R. Thomas, S. Toft, L. Tresse, D. Vergani, M. Wolk, and A. Zirm (2013, August). Mass assembly in quiescent and star-forming galaxies since z $\simeq$ 4 from UltraVISTA. *A&A 556*, A55.

Karim, A., E. Schinnerer, A. Martínez-Sansigre, M. T. Sargent, A. van der Wel, H.-W. Rix, O. Ilbert, V. Smolčić, C. Carilli, M. Pannella, A. M. Koekemoer, E. F. Bell, and M. Salvato (2011, April). The Star Formation History of Mass-selected Galaxies in the COSMOS Field. *ApJ 730*, 61.

Kauffmann, G., T. M. Heckman, S. D. M. White, S. Charlot, C. Tremonti, J. Brinchmann, G. Bruzual, E. W. Peng, M. Seibert, M. Bernardi, M. Blanton, J. Brinkmann, F. Castander, I. Csábai, M. Fukugita, Z. Ivezic, J. A. Munn, R. C. Nichol, N. Padmanabhan, A. R. Thakar, D. H. Weinberg, and D. York (2003, May). Stellar masses and star formation histories for 10^5 galaxies from the Sloan Digital Sky Survey. *MNRAS 341*, 33–53.

Kennicutt, Jr., R. C. (1998). Star Formation in Galaxies Along the Hubble Sequence. *ARAA 36*, 189–232.

Knapen, J. H., M. Cisternas, and M. Querejeta (2015, December). Interacting galaxies in the nearby Universe: only moderate increase of star formation. *MNRAS 454*, 1742–1750.

Koekemoer, A. M., H. Aussel, D. Calzetti, P. Capak, M. Giavalisco, J.-P. Kneib, A. Leauthaud, O. Le Fèvre, H. J. McCracken, R. Massey, B. Mobasher, J. Rhodes, N. Scoville, and P. L. Shopbell (2007, September). The COSMOS Survey: Hubble Space Telescope Advanced Camera for Surveys Observations and Data Processing. *ApJs 172*, 196–202.

Kornei, K. A., A. E. Shapley, C. L. Martin, A. L. Coil, J. M. Lotz, and B. J. Weiner (2013, September). Fine-structure Fe II* Emission and Resonant Mg II Emission in z ˜ 1 Star-forming Galaxies. *ApJ 774*, 50.

Kriek, M., P. G. van Dokkum, I. Labbé, M. Franx, G. D. Illingworth, D. Marchesini, and R. F. Quadri (2009, July). An Ultra-Deep Near-Infrared Spectrum of a Compact Quiescent Galaxy at z = 2.2. *ApJ 700*, 221–231.

Kriek, M., P. G. van Dokkum, K. E. Whitaker, I. Labbé, M. Franx, and G. B. Brammer (2011). H-alpha and 4000 Å break measurements for 3500 k-selected galaxies at $0.5 < z < 2.0$. *The Astrophysical Journal 743*(2), 168.

Laigle, C., H. J. McCracken, O. Ilbert, B. C. Hsieh, P. Capak, G. Hasinger, J. D. Silverman, I. Davidzon, C. Pichon, J. Coupon, H. Aussel, D. Le Borgne, K. Caputi, Y.-Y. Chang, F. Civano, J. Dunlop, J. Fynbo, A. Koekemoer, O. Le Fevre, E. Le Floch, A. Leauthaud, S. Lilly, L. Lin, S. Marchesi, B. Milvang-Jensen, M. Salvato, N. Scoville, M. Stockmann, Y. Taniguchi, S. Toft, and J. Zabl (submitted). The cosmos2015 catalogue: Exploring the $1 < z < 6$ universe with half a million galaxies. *ApJ, submitted*.

Lin, L., P. Capak, C. Laigle, O. Ilbert, B.-C. Hsieh, H.-Y. Jian, B. C. Lemaux, J. D. Silverman, J. Coupon, H. J. McCracken, G. Hasinger, O. Le Fevre, and N. Scoville (2015, November). The SPLASH survey: Quiescent galaxies are more strongly clustered but are not necessarily located in high-density environments. *ArXiv e-prints*.

Lupton, R., M. R. Blanton, G. Fekete, D. W. Hogg, W. O'Mullane, A. Szalay, and N. Wherry (2004, February). Preparing Red-Green-Blue Images from CCD Data. *PASP 116*, 133–137.

Martin, C. L., A. E. Shapley, A. L. Coil, K. A. Kornei, N. Murray, and A. Pancoast (2013, June). Scattered Emission from z ˜ 1 Galactic Outflows. *ApJ 770*, 41.

McCracken, H. J., B. Milvang-Jensen, J. Dunlop, M. Franx, J. P. U. Fynbo, O. Le Fèvre, J. Holt, K. I. Caputi, Y. Goranova, F. Buitrago, J. P. Emerson, W. Freudling, P. Hudelot, C. López-Sanjuan, F. Magnard, Y. Mellier, P. Møller, K. K. Nilsson, W. Sutherland, L. Tasca, and J. Zabl (2012, August). UltraVISTA: a new ultra-deep near-infrared survey in COSMOS. *A&A 544*, A156.

Milvang-Jensen, B., W. Freudling, J. Zabl, J. P. U. Fynbo, P. Møller, K. K. Nilsson, H. J. McCracken, J. Hjorth, O. Le Fèvre, L. Tasca, J. S. Dunlop, and D. Sobral (2013, December). On-sky characterisation of the VISTA NB118 narrow-band filters at 1.19 μm. *A&A 560*, A94.

Mo, H., F. C. van den Bosch, and S. White (2010, May). *Galaxy Formation and Evolution*.

Nielsen, N. M., C. W. Churchill, G. G. Kacprzak, and M. T. Murphy (2013, October). MAGIICAT I. The Mg II Absorber-Galaxy Catalog. *ApJ 776*, 114.

Patrício, V., J. Richard, A. Verhamme, L. Wisotzki, J. Brinchmann, M. L. Turner, L. Christensen, P. M. Weilbacher, J. Blaizot, R. Bacon, T. Contini, D. Lagattuta, S. Cantalupo, B. Clément, and G. Soucail (2015, December). A young star-forming galaxy at $z = 3.5$ with an extended Ly\,α halo seen with MUSE. *ArXiv e-prints*.

Rodighiero, G., E. Daddi, I. Baronchelli, A. Cimatti, A. Renzini, H. Aussel, P. Popesso, D. Lutz, P. Andreani, S. Berta, A. Cava, D. Elbaz, A. Feltre, A. Fontana, N. M. Förster Schreiber, A. Franceschini, R. Genzel, A. Grazian, C. Gruppioni, O. Ilbert, E. Le Floch, G. Magdis, M. Magliocchetti, B. Magnelli, R. Maiolino, H. McCracken, R. Nordon, A. Poglitsch, P. Santini, F. Pozzi, L. Riguccini, L. J. Tacconi, S. Wuyts, and G. Zamorani (2011, October). The Lesser Role of Starbursts in Star Formation at $z = 2$. *ApJl 739*, L40.

Roig, B., M. R. Blanton, and N. P. Ross (2013, December). Unusual Broad-Line MgII Emitters Among Luminous Galaxies in BOSS. *ArXiv e-prints*.

Salpeter, E. E. (1955, January). The Luminosity Function and Stellar Evolution. *ApJ 121*, 161.

Scalo, J. M. (1986). The initial mass function of massive stars in galaxies Empirical evidence. In C. W. H. De Loore, A. J. Willis, and P. Laskarides (Eds.), *Luminous Stars and Associations in Galaxies*, Volume 116 of *IAU Symposium*, pp. 451–466.

Scoville, N., H. Aussel, M. Brusa, P. Capak, C. M. Carollo, M. Elvis, M. Giavalisco, L. Guzzo, G. Hasinger, C. Impey, J.-P. Kneib, O. LeFevre, S. J. Lilly, B. Mobasher, A. Renzini, R. M. Rich, D. B. Sanders, E. Schinnerer, D. Schminovich, P. Shopbell, Y. Taniguchi, and N. D. Tyson (2007, September). The Cosmic Evolution Survey (COSMOS): Overview. *ApJs 172*, 1–8.

Silk, J. and M. J. Rees (1998, March). Quasars and galaxy formation. *A&A 331*, L1–L4.

Smolčić, V., A. Karim, O. Miettinen, M. Novak, B. Magnelli, D. A. Riechers, E. Schinnerer, P. Capak, M. Bondi, P. Ciliegi, M. Aravena, F. Bertoldi, S. Bourke, J. Banfield, C. L. Carilli, F. Civano, O. Ilbert, H. T. Intema, O. Le Fèvre, A. Finoguenov, G. Hallinan, H.-R. Klöckner, A. Koekemoer, C. Laigle, D. Masters, H. J. McCracken, K. Mooley, E. Murphy, F. Navarette, M. Salvato, M. Sargent, K. Sheth, S. Toft, and G. Zamorani (2015, April). Physical properties of z $>$ 4 submillimeter galaxies in the COSMOS field. *A&A 576*, A127.

Stark, D. P., J. Richard, S. Charlot, B. Clément, R. Ellis, B. Siana, B. Robertson, M. Schenker, J. Gutkin, and A. Wofford (2015, June). Spectroscopic detections of C III] λ1909 Å at z $\sim$ 6-7: a new probe of early star-forming galaxies and cosmic reionization. *MNRAS 450*, 1846–1855.

Talia, M., A. Cimatti, L. Pozzetti, G. Rodighiero, C. Gruppioni, F. Pozzi, E. Daddi, C. Maraston, M. Mignoli, and J. Kurk (2015, October). The star formation rate cookbook at 1 $<$ z $<$ 3: Extinction-corrected relations for UV and [OII]λ3727 luminosities. *A&A 582*, A80.

Taniguchi, Y., M. Kajisawa, M. A. R. Kobayashi, Y. Shioya, T. Nagao, P. L. Capak, H. Aussel, A. Ichikawa, T. Murayama, N. Z. Scoville, O. Ilbert, M. Salvato, D. B. B. Sanders, B. Mobasher, S. Miyazaki, Y. Komiyama, O. Le Fèvre, L. Tasca, S. Lilly, M. Carollo, A. Renzini, M. Rich, E. Schinnerer, N. Kaifu, H. Karoji, N. Arimoto, S. Okamura, K. Ohta, K. Shimasaku, and T. Hayashino (2015, November). The Subaru COSMOS 20: Subaru optical imaging of the HST COSMOS field with 20 filters*. *PASJ*.

Tilton, E. M. and J. M. Shull (2013, September). Ultraviolet Emission-line Correlations in HST/COS Spectra of Active Galactic Nuclei: Single-epoch Black Hole Masses. *ApJ 774*, 67.

Toft, S., P. van Dokkum, M. Franx, I. Labbe, N. M. Förster Schreiber, S. Wuyts, T. Webb, G. Rudnick, A. Zirm, M. Kriek, P. van der Werf, J. P. Blakeslee, G. Illingworth, H.-W. Rix, C. Papovich, and A. Moorwood (2007, December). Hubble Space Telescope and Spitzer Imaging of Red and Blue Galaxies at z ˜ 2.5: A Correlation between Size and Star Formation Activity from Compact Quiescent Galaxies to Extended Star-forming Galaxies. *ApJ 671*, 285–302.

Vignali, C., M. Mignoli, R. Gilli, A. Comastri, K. Iwasawa, G. Zamorani, V. Mainieri, and A. Bongiorno (2014, November). The space density of Compton-thick AGN at z 0.8 in the zCOSMOS-Bright Survey. *A&A 571*, A34.

Weiner, B. J., A. L. Coil, J. X. Prochaska, J. A. Newman, M. C. Cooper, K. Bundy, C. J. Conselice, A. A. Dutton, S. M. Faber, D. C. Koo, J. M. Lotz, G. H. Rieke, and K. H. R. Rubin (2009, February). Ubiquitous Outflows in DEEP2 Spectra of Star-Forming Galaxies at z = 1.4. *ApJ 692*, 187–211.